Ph. D. Thesis, Eindhoven University of Technology, July 2020

ISBN: 978-94-92323-37-8

The work described in this thesis was performed at:
AMOLF, Science Park 104, 1098 XG Amsterdam, The Netherlands

This work is part of the Dutch Research Council (NWO)

A digital version of this thesis is available at:
`https://ir.amolf.nl/` and `https://research.tue.nl/`.

Glancing at tiny vibrations

Backaction evading measurements of mechanical motion close to the quantum regime

PROEFSCHRIFT

ter verkrijging van de graad van doctor aan de Technische Universiteit Eindhoven, op gezag van de rector magnificus prof.dr.ir. F.P.T. Baaijens, voor een commissie aangewezen door het College voor Promoties, in het openbaar te verdedigen op woensdag 1 juli 2020 om 11:00 uur

door

Giada Rita La Gala

geboren te Acquaviva delle Fonti, Italië

Dit proefschrift is goedgekeurd door de promotoren en de samenstelling van de promotiecommissie is als volgt:

Voorzitter:	prof. dr. ir. G. M. W. Kroesen	
1^{e} promotor:	prof. dr. E. Verhagen	
2^{e} promotor:	prof. dr. A. F. Koenderink	(Universiteit van Amsterdam)
leden:	dr. M. Vanner	(Imperial College London)
	prof. dr. A. Polman	(Universiteit van Amsterdam)
	prof. dr. A. Fiore	
	dr. P. Zijlstra	

Het onderzoek of ontwerp dat in dit proefschrift wordt beschreven is uitgevoerd in overeenstemming met de TU/e Gedragscode Wetenschapsbeoefening.

The ability to perceive or think differently
is more important than the knowledge gained.

David Bohm

CONTENTS

1 Introduction **1**
1.1 Quantum measurement and backaction 1
1.1.1 Evading measurement backaction 2
1.2 Basics of cavity optomechanics 3
1.2.1 Optomechanical Hamiltonian 4
1.2.2 Optical spring 5
1.3 Sliced photonic crystal nanobeams 6
1.3.1 Working principle 7
1.3.2 Fabrication. 8
1.4 Outline of this thesis 9

2 Optomechanical measurement **13**
2.1 Introduction 14
2.2 Homodyne detection 14
2.2.1 Input-output theory of a general cavity system 16
2.2.2 Introducing mechanical fluctuations: measuring cavity detuning in time 18
2.3 Parameter estimation from continuous measurements 20
2.3.1 Transduction function and power spectral density. 20
2.3.2 Quadrature-averaged homodyne detection 22
2.3.3 Application to sliced photonic crystal nanobeam resonators. . 23
2.4 Nonlinear transduction 26
2.4.1 Generalization of the transduction model for higher harmonics 27
2.5 Pulsed measurements. 30

3 Nanomechanical design for single-mode optomechanical measurement **33**
3.1 Introduction 34

3.2 Noise in optomechanical measurements induced by spurious modes . . . 35
3.2.1 Noise in continuous measurements induced by a spurious mode . . . 36
3.2.2 Noise in pulsed measurements induced by a spurious mode. . 38
3.2.3 Comparison . . . 39
3.3 Robust mode symmetries in optomechanical systems . . . 40
3.4 Mechanical design strategy . . . 41
3.5 Results . . . 43
3.6 Light-mediated mechanical coupling . . . 51
3.7 Conclusions. . . . 54

4 Backaction evading measurements of mechanical motion 57
4.1 Backaction evading measurements . . . 58
4.1.1 Pulsed backaction evasion . . . 58
4.1.2 Conditional states and measurement-induced squeezing . . . 59
4.1.3 Measurement strength . . . 61
4.2 Experimental realization . . . 62
4.2.1 Experimental methods. . . . 63
4.2.2 Data analysis: postselection . . . 65
4.2.3 State tomography . . . 69
4.3 Imperfection induced second mode noise . . . 72
4.4 Pulsed measurement with one mechanical mode. . . . 74
4.5 Conclusions. . . . 78
4.6 Appendix: Conditional state variances . . . 79

5 Improving optical coupling to sliced nanobeam devices in a free space setup 81
5.1 Motivation . . . 82
5.2 Design . . . 83
5.2.1 Coupling a sliced nanobeam to a waveguide . . . 84
5.2.2 Waveguide mirror . . . 87
5.2.3 Tapered waveguide . . . 88
5.3 Nanofabrication . . . 90
5.4 Optical characterization . . . 93
5.4.1 Coupling efficiency in input-output relations . . . 93
5.5 Characterization with a fiber coupled setup. . . . 94
5.6 Discussion and conclusions. . . . 99
5.7 Appendix: Modification of optical setup for free-space coupling via inverted taper waveguides . . . 101

Summary 103

About the author 105

Acknowledgements 107

Bibliography 111

1

INTRODUCTION

One of the main unsolved problems in physics is the description of the transition between classical and quantum realm. Quantum laws of physics are used to describe microscopic systems, while macroscopic systems generally follow the laws of classical physics. It is however not clear whether quantum phenomena are in principle possible but not visible in macroscopic systems or if quantum mechanics would break down beyond a certain complexity scale [1]. Cavity optomechanics deals with mechanical devices that can be considered macroscopic, with harmonically oscillating masses composed of billions or trillions of atoms even if they have sizes of the order of micrometers. For this reason it is a well-suited platform to study quantum states and decoherence of *large* mechanical resonators. The properties of optomechanical systems make the occurrence of quantum effects, such as vacuum fluctuations, accessible experimentally [2, 3]. Some of the milestones achieved in the field include the optical cooling near a mechanical resonator quantum groundstate [4–7], entanglement [8–10], coherent state transfer [11–13], quantum squeezing of a mechanical resonator motion [14, 15], creation of non-classical squeezed light [16, 17], observation of radiation pressure shot noise [18, 19] and non-classical correlations between photons and phonons [20–23].

1.1. QUANTUM MEASUREMENT AND BACKACTION

Among the main challenges in the field of quantum optomechanics is the development of measurement schemes with greater sensitivity, in order to address the detection of quantum phenomena and characterize quantum states of motion. For continuous displacement measurements, i.e. measurements that are long compared to the characteristic mechanical oscillation period, a fundamental limit to the sensitivity of a measurement is set by the Heisenberg uncertainty principle that is called the *standard quantum limit* (SQL) [24, 25]. It is the result of the fact that continuous measurements simultaneously probe two non-commuting variables such as position and momentum. Enforced by the quantum fluctuations

in the number of photons of the coherent light used in cavity optomechanical measurement, the standard quantum limit tells that a measurement of mechanical motion through a light field adds at least a certain amount of uncertainty. This minimum amount is well defined and is equal to what is called *zero point fluctuation* amplitude, i.e. the amplitude of the displacement fluctuations that the mechanical oscillator exhibits when it is cooled to its quantum ground state

$$x_{\mathrm{zpf}} = \sqrt{\frac{\hbar}{2m\omega_m}}, \tag{1.1}$$

where $\hbar$ is the reduced Planck constant, m is the mass of the moving object and ω_m is its natural oscillation frequency. Two sources of noise can contribute to the quantum uncertainty added by a measurement: on the one hand, quantum noise (e.g. photon shot noise) on the detected measurement signal leads to a finite measurement imprecision. On the other hand, the measurement also necessarily perturbs the system that is measured, in a process termed *measurement backaction*. For example, the photons that perform the measurement of a mechanical resonator's position transfer momentum to the resonator through the radiation pressure force. Thus, the quantum fluctuations of the optical laser field create a stochastic force that drives the resonator into random motion. In a standard setting, the minimum added uncertainty (standard quantum limit) is reached at a given measurement strength, where imprecision and backaction noises give equal contributions to the total measurement noise. For lower probing powers, shot noise imprecision dominates, while for higher powers, radiation pressure backaction induces random motion exceeding the ground state fluctuations [25].

1.1.1. EVADING MEASUREMENT BACKACTION

This limitation to measurement precision, set by the SQL, is important if the goal is to resolve characteristic quantum features of the motion of a mechanical oscillator. For example, a truly non-classical quantum state would be one characterized by a negative Wigner density [26], which is a quasiprobability distribution that describes a quantum state in phase space. In order to even be able to reconstruct the Wigner density it is necessary to have a precision better than x_{zpf} [27]. As such, measurement techniques with that level of sensitivity would be a holy grail in the field of quantum optomechanics, allowing to reconstruct a system quantum state and assessing its quantum signatures. Moreover, they could allow ways to improve sensors beyond traditional limits, to detect small forces, displacements, or accelerations for example.

Measurements that can surpass this limit have been proposed and go under the name of *back-action evading* measurements [24, 25, 28–32]. The key idea of such measurements is that they perform only a partial characterization of the system, performing a measurement of one quantity with very high precision while ensuring that all quantum measurement backaction is affecting another, unmeasured quantity. For example, if one measures only the position at a certain time $t = 0$ of a mechanical object while gaining no knowledge of its momentum, the (stochastic) radiation pressure force associated with the measurement would only

add uncertainty to the momentum at that same time. While that means that the full trajectory of the object versus time is not known, the first position measurement itself can be performed with in principle arbitrary precision. Backaction-evading measurements have been performed on various systems including light fields, the spin of atomic ensembles, and mechanical resonators [33–36]. In cavity optomechanics, backaction-evading measurements have been demonstrated using very narrowband cavities probed with continuous laser fields whose amplitude is modulated harmonically in time at twice the mechanical resonance frequency [37–42].

In this thesis we show examples of different kinds of measurements that can evade backaction, in the context of *pulsed optomechanics* [43, 44]. These are fast measurements of motion made with light pulses. In contrast to continuous modulated probe field strategies, they do not require extremely narrowband optical cavities, and could achieve sub-SQL characterization of quantum states in times much shorter than typical mechanical decoherence times. The key quality of these kind of measurements is their restriction on the measurement time to a fraction of the mechanical period, to avoid the collection of a signal that carries the influence of measurement backaction. By choosing the relative delay of pulse sequences with respect to the mechanical evolution it is possible to use the measurements to prepare the mechanical resonator into a squeezed motional state. Moreover, the ability to resolve the full dynamics of the mechanical oscillation without perturbing its motion allows to perform *state tomography* [27, 44]. Combined with nonlinear measurement or non-Gaussian states of light, pulsed interactions can also induce other nonclassical states [45, 46]. Moreover, proposals suggested exploiting pulsed measurements for swap operations between mechanics and light [47] and creation of macroscopic superpositions [46].

1.2. BASICS OF CAVITY OPTOMECHANICS

Optomechanics is a field of physics at the intersection of condensed matter physics (photonics, optics, mechanics) and quantum optics (quantum mechanics with photons). It studies the interaction of optical fields with mechanical oscillations. At the core of optomechanics is the concept that a stream of photons can transfer momentum onto a massive object by exerting a force upon them called *radiation pressure*. When the effect is large enough the object experiences a measurable displacement. This was already hypothesized by Kepler who noticed in 1619 that tails of comets can be deflected by the optical field radiated by the sun [48]. In fact, the light from stars is sufficiently strong to create visible displacement into the rarefied interstellar clouds. It should be realized that the double nature of the interaction means that there exists also a *mechanoptic* side. The object motion, whether induced by the light field or through other means, impacts the field itself which experiences a recoil of the radiation pressure force, or in other words experiences a form of *backaction*.

In a cavity optomechanical system, such as that depicted in Fig.1.1, the optical field and the mechanical oscillator mode coexist in an optical cavity. The magnitude of the optomechanical interaction is enhanced by the energy buildup

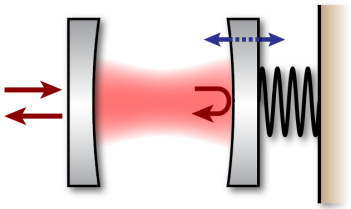

Figure 1.1: Schematic of the simplest cavity optomechanical system: a Fabry-Perot cavity with a movable mirror (attached to a spring to indicate harmonic motion in the direction indicated by the blue arrow). A resonant driving light field can enter and exit the cavity via the left mirror.

of the optical resonance, which is affected by the mechanical motion and vice versa. In the presence of a mechanical and an optical resonance a number of dynamical effects can take place. Depending on the relative timings of optical and mechanical modulations and on the magnitude of the parameters characterizing an optomechanical system (mechanical resonance frequency ω_m, mechanical linewidth Γ, optical linewidth κ and drive laser detuning $\Delta = \omega - \omega_c$, with ω the laser frequency and ω_c the cavity resonance frequency), effects become available under the general denominator of *dynamical backaction* (such as the optical spring effect, see section 1.2.2, cooling and amplification of mechanical motion, optomechanically induced transparency [49], and nonlinear dynamics) [3].

1.2.1. OPTOMECHANICAL HAMILTONIAN

The system composed of a coupled mechanical and optical oscillator can be described by a Hamiltonian

$$\hat{H} = \hbar\omega_c(x)\hat{a}^\dagger\hat{a} + \hbar\omega_m\hat{b}^\dagger\hat{b} \tag{1.2}$$

where ω_c and ω_m are the optical and mechanical resonance frequencies, $\hat{a}^\dagger$ and $\hat{b}^\dagger$ are the optical and mechanical creation operators, with the respective annihilation operators $\hat{a}$ and $\hat{b}$. The first term of the Hamiltonian can be split in a term describing the uncoupled optical degree of freedom and terms describing the optomechanical parametric coupling through

$$\omega_c(x) \simeq \omega_c + x\frac{\partial\omega_c}{\partial x} + ..., \tag{1.3}$$

where x is the mechanical displacement. In most realizations of cavity optomechanics it is sufficient to keep only the linear term of eq.1.3. Defining the quantity

$$G = -\partial\omega_c/\partial x \tag{1.4}$$

that represent the optical frequency shift per displacement [3], the interaction term in the Hamiltonian can then be written as

$$\hat{H}_{\text{int}} = -\hbar G\hat{x}\hat{a}^\dagger\hat{a}, \tag{1.5}$$

from which we recognize the expression for the radiation pressure force

$$\hat{F} = -\frac{d\hat{H}_{\rm int}}{d\hat{x}} = \hbar G \hat{a}^\dagger \hat{a}. \tag{1.6}$$

Since $\hat{n} = \hat{a}^\dagger \hat{a}$ is the number operator, we see that $\hbar G$ is the force per photon. It follows that we can write

$$G\hat{x} = G x_{\rm ZPF}(\hat{b} + \hat{b}^\dagger) \equiv g_0(\hat{b} + \hat{b}^\dagger), \tag{1.7}$$

where g_0 is the *vacuum optomechanical coupling rate* (sometimes referred to as 'single photon-phonon coupling rate') that indicates the strength of the optomechanical interaction. It corresponds to the cavity frequency shift induced by a mechanical zero-point displacement [3]. Usually this parameter is way smaller than the optical frequency; $g_0 \ll \omega_c$. For this reason it is said that the mechanical degree of freedom is parametrically coupled to the optical one. The effect of the interaction is to modestly vary the optical frequency around its bare frequency value through mechanical displacement. In the next section we present the specific system we study in the rest of this thesis, which is characterized by particularly large values of the optomechanical coupling strength g_0. Having defined g_0 we can rewrite the interaction Hamiltonian in the basic form

$$\hat{H}_{\rm int} = -\hbar g_0 \hat{a}^\dagger \hat{a}(\hat{b} + \hat{b}^\dagger). \tag{1.8}$$

We finally note that in the case of a large coherent optical drive with intracavity amplitude $\bar{\alpha}$, the field operator can be written as $\hat{a} = \bar{\alpha} + \delta\hat{a}$, where $\delta\hat{a}$ denotes small fluctuations. For small enough mechanical displacement and optomechanical coupling, this leads to a linearized form of the interaction Hamiltonian

$$\hat{H}_{\rm int} = -\hbar g_0 \bar{\alpha}(\delta\hat{a} + \delta\hat{a}^\dagger)(\hat{b} + \hat{b}^\dagger), \tag{1.9}$$

where we have neglected higher order terms in the optical fluctuations and we assumed $\bar{\alpha}$ to be real without loss of generality. While we show that this approximation can break down in our systems (section 2.4), it still shows that in a basic form, the laser-driven optomechanical cavity allows a linear coupling between the mechanical displacement $x_{\rm zpf}(\hat{b} + \hat{b}^\dagger)$ and the cavity electric field fluctuations $\mathscr{E}_{\rm vac}(\hat{a} + \hat{a}^\dagger)$ (with $\mathscr{E}_{\rm vac}$ the vacuum field). In the context of measurement, it shows how mechanical fluctuations can be read out through the field that leaks out of the cavity.

1.2.2. OPTICAL SPRING

One basic phenomenon due to radiation pressure in cavity optomechanical systems is the *optical spring effect*. When the laser detuning is scanned across the optical resonance, one can observe a shift of the mechanical frequency on either side of the cavity resonance. There, a small mechanical displacement leads to a change of the photon number and thus a change in the optical force. Depending on the detuning, the direction of this force is either opposite (or equal) to the mechanical restoring

force. As such, it can lead to an optical stiffening or softening of the mechanical spring constant. In the so-called unresolved sideband regime (where the optical cavity linewidth $\kappa \gg \omega_m$), the expression that describes the frequency shift is [50]

$$\delta\omega_m = g_0^2 \frac{2\Delta}{(\Delta^2 + \kappa^2/4)^2} \frac{\kappa_{\text{in}} P_{\text{in}}}{\hbar\omega}, \tag{1.10}$$

where $\Delta = \omega - \omega_c$ is the laser detuning, P_{in} is the optical power incident on the cavity and κ_{in} is the rate that describes how well that light can couple into the optical cavity. Figure 1.2 shows an example of the effect for small laser power, together with a fit according to equation 1.10.

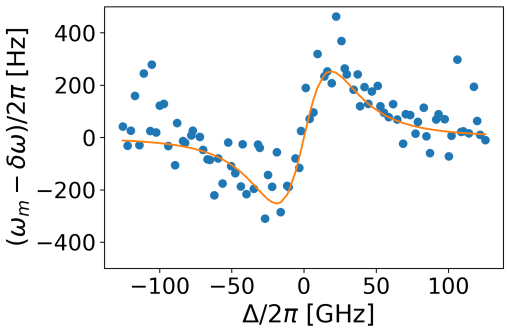

Figure 1.2: Optical spring shift observed with P_{in} = 136nW on a sliced nanobeam as described in the following section. Equation 1.10 is fitted (orange line) through the experimental data points (blue dots). The cavity linewidth of $\kappa \approx 40$ GHz determines the bandwidth over which the effect is observed.

1.3. SLICED PHOTONIC CRYSTAL NANOBEAMS

In this thesis we experimentally study the optomechanics of nanophotonic cavities that we call 'sliced photonic crystal nanobeams'. The large photon-phonon coupling rates observed for these cavities are of the order of $g_0/2\pi \simeq 10-25$ MHz which, together with optical linewidths of $\kappa/2\pi \simeq 10-100$ GHz and mechanical linewidths of $\Gamma \simeq 100$ Hz at cryogenic temperatures implies that the devices show a single photon-phonon cooperativity $C_0 \equiv 4g_0^2/\kappa\Gamma \gg 1$. This parameter compares the strength of the optomechanical coupling to the system's dissipation (both optical and mechanical) and in particular represents the inverse of the number of photons needed to perform a measurement at the standard quantum limit with the assumption of perfect collection efficiency, i.e. all photons contributing to the measurement [3]. The large values of the single photon-phonon cooperativity make the sliced nanobeam cavity parameters comparable to cold atom systems [18] rather than typical optomechanical nanodevices.

The structures are an example of optomechanics in the 'bad cavity' regime, i.e. the regime in which the optical decay rate κ is larger than the mechanical resonance frequency ω_m. In chapter 4 we will show that this is a useful feature, since it allows to use an optical field to take snapshot measurements of the mechanical motion. In the

following section we briefly illustrate the optical and mechanical design principles covered extensively by Leijssen et al. [51] and Freisem et al. [52]. Afterwards we give a summary of the protocol employed for the nano-fabrication of the devices.

1.3.1. WORKING PRINCIPLE

The sliced nanobeam cavity is a one-dimensional photonic crystal that from a mechanical perspective is the equivalent of two suspended doubly clamped beams of a length of $\sim 15\mu$m lying in very close proximity with a separation of ~ 60 nm. The large optomechanical interaction strength derives from the tight confinement of optical modes and the spatial overlap of optical and mechanical modes. For the nanobeams this can be achieved by engineering a defect cavity mode in the photonic crystal and forcing the field to be confined in a small gap [53], i.e. in the interstice introduced by the 'slice' of the photonic crystal along the longitudinal axis. In Fig.1.3 we show the spatial profile of the in-plane electric field component

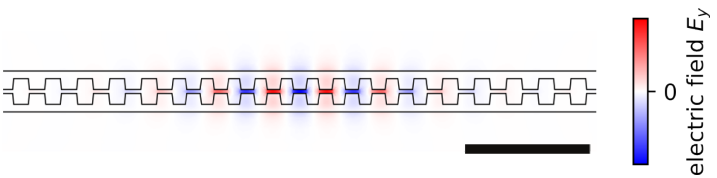

Figure 1.3: Top view of the simulated spatial profile of the electric field component y (color bar) for the first cavity mode, simulated with COMSOL. The scalebar corresponds to 2μm.

E_y of the sliced nanobeam cavity mode. The defect mode is created by locally varying the periodicity of the photonic crystal, which exhibits a photonic crystal bandgap for the relevant optical frequencies in the regions outside the defect. In order to design the optimal geometry, in particular choosing the desired mode eigenfrequency (around ~ 200 THz) while maximizing the cavity mode quality factor we study the structure band diagram by simulating the device eigenmodes with COMSOL [51]. In particular we design a tapered defect mode in which the band diagram is progressively modified, to minimize radiation from light to the free-space continuum.

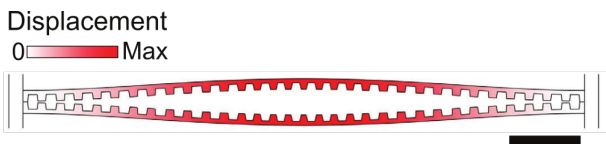

Figure 1.4: Top view of the fundamental first order in-plane flexural mode of vibration of the sliced nanobeam cavity. The color bar shows the normalized displacement profile simulated with COMSOL. The scalebar corresponds to 2μm.

In Fig.1.3 we can recognize that the cavity mode is localized in the middle of the nanobeam, where the electric field E_y is strongest. In the same location we have maximum displacement of the first order in-plane flexural mechanical

mode supported by the structure (at ~ 3 MHz), Fig.1.4. The motion of the nanobeam oscillating in this mode modulates the slot width and thus the effective refractive index of the nanobeams, giving rise to the optomechanical coupling. The mechanical mode shown in Fig.1.4 is ideal, in the sense that it maximally modulates the cavity mode and is spectrally well isolated from other mechanical modes. Practical realizations of the devices do not generally show the ideal eigenmodes. In chapter 3 we investigate how to circumvent this limitation.

In the experiments we employ free-space coupling of the excitation light beam at perpendicular incidence. The structures, that otherwise are designed not to radiate in that direction, contain a *double period modulation*: by introducing a periodic refractive index modulation with a period twice as large of that of the photonic crystal structure it is possible to create a diffraction grating that is integrated in the structure itself and that radiates at normal incidence [51]. The efficiency at which we can collect light from the structures is however limited to 1%. In chapter 5 we present an integrated architecture that allow us to achieve higher light coupling efficiencies.

1.3.2. FABRICATION

In order to fabricate the devices we employ a top-down fabrication process based on nanolithography. The process flow is shown in Fig.1.5. The devices are formed out of

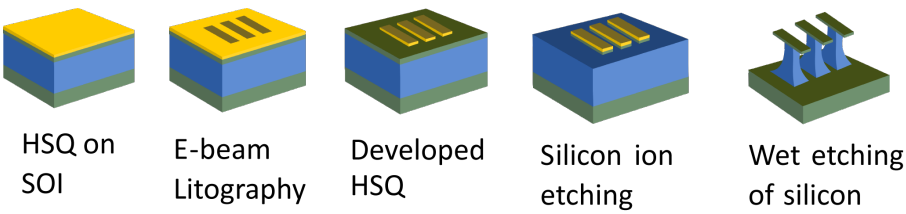

Figure 1.5: Fabrication process: a) A layer of HSQ resist (yellow) is spincoated on top of a 220 nm SOI chip (green: silicon, blue: silicon dioxide). b) The resist layer is patterned by means of EBL. c) The patterned resist is developed by means of TMAH. d) The top resist mask is transferred to the 220 nm silicon layer by means of reactive ion etching. Finally e), the glass box is removed by isotropic wet HF etching.

the top silicon layer of a *silicon-on-insulator* (SOI) wafer characterized by a 220 nm silicon layer on top of 3 μm silicon oxide 'BOX' layer. We create a two-dimensional mask by patterning a resist layer that we spincoat on top of the wafer. The thickness of the resist is chosen to balance two counteracting factors. On the one side the thickness determines the resolution we are able to obtain in the patterning; the thinner the resist the better the resolution. On the other hand the resist mask is used to transfer the pattern written in the resist onto the silicon in the anisotropic plasma etching step [54]. This step is based on the different etching rate of two materials (resist and silicon) exposed to the same ion plasma. The relative etching rate determines the selectivity of the etching process hence the minimum required resist thickness that would sustain the penetration of 220 nm silicon without the complete resist depletion. We use a negative resist hydrogen silsesquioxane (HSQ), which implies that the developed mask will show the portions of the layer that

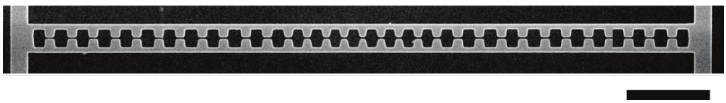

Figure 1.6: Electron micrograph of a silicon sliced nanobeam. The scalebar corresponds to 2μm. Figure courtesy of Rick Leijssen [59].

have being written. The writing process is done by *electron beam lithography* (EBL), which effectively transforms the HSQ to a glass-like composition of material that resembles SiO_2 after development [55]. It is crucial in this step to have a high resolution that can be achieved with small beam aperture at low electron beam currents on a relatively thin resist (we use a thickness of ~ 50 nm). Imperfections in the resist mask will be translated to the underlying silicon layer and will affect the performance of the photonic crystal by introducing defects or scattering particles. For this reason it is important to achieve the highest possible resolution in the EBL step. The exposed HSQ is developed using a solution of 25% tetramethylammonium hydroxide (TMAH) at 50°C.

The next step is to transfer the mask pattern to the silicon device layer through reactive ion etching with an inductively coupled plasma. As already mentioned, one critical factor in this step is the correct selectivity of the etching recipe. Moreover the chemical composition of the plasma gas determines the shape of the silicon sidewalls via the formation of passivation layers. We use a inductively-coupled hydrogen bromide (HBr) plasma for high-selectivity etching of silicon with respect to SiO_2 and HSQ [56–58]. The reactive ion etching step is composed of two steps: a first step uses a 20 sccm HBr plasma and serves to remove the native oxide layer with a thickness of approximately 2 – 3nm. The second and main step uses a combination of 48.5sccm HBr and 1.5sccm O_2 plasma gasses inductively coupled, at low acceleration power to allow bringing the plasma close to the sample and react with the silicon. In this step the developed HSQ mask is used to pattern the silicon.

The final step uses an isotropic etching of glass through hydrofluoridic acid (at a concentration of 20%) in order to perform the membrane release: the remaining SiO_2 after the etching will serve as support pads for the suspended bridges. For the final step we dry any remaining washing water from the samples at the critical point in order to avoid non-uniform evaporation that leads to sticking problems of the nanobeam slices with each other. In Fig.5.8 we show a scanning electron microscope picture of a finished device.

1.4. OUTLINE OF THIS THESIS

In this thesis, we study optomechanical measurements of sliced photonic crystal nanobeams, with the aim to bring such measurements to a regime where single backaction-evading pulses can characterize mechanical quantum states with sub-SQL precision. We discuss methods of sample and measurement design, and demonstrate pulsed measurements approaching the quantum regime.

In chapter 2, we introduce the measurement methods employed in the

experiments and in particular balanced homodyne interferometry, which is a well-known detection technique that allows sensitive characterization of light fields. We discuss both continuous and pulsed measurements. We show that in continuous measurements it can be useful to introduce a modulation of the reference beam arm length, that corresponds to averaging all optical phases. The measurement signal becomes easy to interpret and allows to characterize the absolute magnitude of a cavity frequency modulation. This is especially relevant in our case, where, due to high optomechanical coupling to optical decay rate ratio, the mechanical signal can be transduced nonlinearly.

In chapter 3, we examine the mechanical response of nanobeam systems in the presence of realistic disorder. The resonators always show multiple modes that can limit the level of effective sensitivity and control that can be achieved in optomechanical measurements. We present and experimentally implement a strategy to mitigate the effect of unwanted mechanical modes. We examine in detail the importance of the noise contributions due to the presence of spurious modes and argue how spectral design of the system can optimize those noise contributions even in the presence of perturbations due to random fabrication imperfections. We then implement this design strategy in the case of a sliced photonic crystal nanobeam cavity. We report the mechanical performance of experimental realizations, and evaluate the figures of merit for varying designs, in the contexts of either continuous or pulsed measurement. We finally discuss how the strategy can be interpreted in a model of two coupled modes and show the occurrence of light mediated coupling.

In chapter 4, we demonstrate pulsed optomechanical measurements on sliced nanobeams. We show that the sensitivity of these measurements can be close to the quantum regime, achieving a single-pulse measurement imprecision of 9 times the zero-point fluctuation size (x_{zpf}) constrained by optical detection efficiency. We prepare both thermally squeezed and purified (cooled) conditional mechanical states, and perform full state tomography on these. We study how additional mechanical modes affect the conditional state, limiting its width to $58x_{\mathrm{zpf}}$. We demonstrate how mechanical decoherence and re-thermalization can be tracked by recording the state evolution at longer time scales. Furthermore we perform pulsed measurements on structures designed to show a single fundamental first order mechanical mode, showing how the width of the conditional state can be brought down to $\sim 28x_{\mathrm{zpf}}$, limited by optical shot noise and the presence of a third order mode.

Finally, in chapter 5 we investigate the possibility to increase measurement efficiency through alternative light extraction methods. We design an on-chip architecture that can be used in a free-space setup. We evanescently couple a slab waveguide to the sliced nanobeam cavity. The waveguide is designed to have a tapered ending with a radiation profile that can be mode matched to that of a focused laser beam incoming from the objective lens. We fabricate the devices on the edge of the silicon chip so that the ending facet of the tapered waveguide can lie at a distance equal to the objective focal length. We report spectroscopic measurements aimed at characterizing this on-chip optical coupling method for

efficient measurement.

2

OPTOMECHANICAL MEASUREMENT

This chapter describes detection methods for high-sensitivity optomechanical displacement measurement. We focus in particular on balanced homodyne detection. We introduce the method of quadrature-averaged homodyne detection, and show how system parameters can be retrieved in optomechanical systems that exhibit nonlinear transduction. Finally, we introduce the concept of pulsed displacement measurements. [1]

[1] Parts of these measurements were published in Nat. Commun. 8, 16024 (2017).

2.1. INTRODUCTION

Measurements of mechanical motion through the interaction of optical cavity modes and mechanical vibrations are at the core of this thesis. In section 1.2, we saw that this parametric interaction is described by the cavity frequency shift imparted through mechanical displacement. In this chapter we introduce the methods that we use in the reported experiments to detect such frequency shifts. A central role is taken by homodyne interferometry [60], which we employ in the majority of measurements.

Depending on the duration of the optical measurement compared to the mechanical oscillation period, we can distinguish continuous and pulsed regimes of position measurements. In continuous measurements, the measurement time is much longer than the mechanical oscillation period. We use these for the characterization of system parameters. We introduce the method of *phase-averaged* homodyne interferometry which is particularly suited for that goal. Especially in the context of quantum measurements, in which one wants to resolve displacements that are of the order of the zero point amplitude of motion, achieving the highest possible sensitivity is an important goal [3, 24, 25, 61, 62]. To maximize the sensitivity of optomechanical measurements, it is beneficial to employ systems in which mechanically-induced modulation of the optical field is large. However, as we will see the characterization of the optomechanical parameters can become nontrivial for strong enough coupling, in particular due to *nonlinear transduction* of mechanical motion. We report a method for the characterization of the optical and mechanical parameters of our devices in this extreme regime.

When the measurement time is short compared to the mechanical period, we talk about pulsed measurements. Those measurements are interesting because of their back-action evading nature, and their ability to perform both state characterization and manipulation through interactions that are short enough to outpace decoherence [43, 44, 63]. Moreover, their sensitivity can fundamentally overcome the standard quantum limit on continuous measurements.

2.2. HOMODYNE DETECTION

Both a mechanical and an optical mode can be conveniently described using phase space diagrams. A state of the mode is then given by the probability density in that phase space, defining the chance of certain outcomes of measurements on the system. The phase space is spanned by a set of quadrature variables, in terms of which either the electromagnetic field or the mechanical motion can be expressed. For an optical mode in the classical (mean field) limit, the quadratures represent the real and imaginary part of the complex electric field. For a mechanical oscillator mode, they correspond to the canonical position and momentum at a specific time in the oscillation cycle. We can write the mechanical displacement operator as

$$\hat{x}(t) = \hat{X}(t)\cos(\omega_{\mathrm{m}} t) + \hat{Y}(t)\sin(\omega_{\mathrm{m}} t), \tag{2.1}$$

where ω_{m} is the mechanical frequency. The two quadratures $\hat{X}(t)$ and $\hat{Y}(t)$ vary slowly in time compared to the mechanical oscillation period $2\pi/\omega_{\mathrm{m}}$, i.e., they are

defined in a frame rotating at the mechanical frequency. They are related to the annihilation and creation operators $\hat{a}$ and $\hat{a}^\dagger$ through

$$\hat{X} = x_{\mathrm{zpf}}(\hat{a} + \hat{a}^\dagger), \tag{2.2}$$

$$\hat{Y} = -ix_{\mathrm{zpf}}(\hat{a} - \hat{a}^\dagger), \tag{2.3}$$

where x_{zpf} is the mechanical zero-point amplitude and the annihilation and creation operators are also defined in a rotating frame.[2] For an optical mode, similar expression relate the quadratures to the electric field by replacing the zero-point displacement x_{zpf} by the vacuum electric field.

At time $t = 0$, the quadratures relate to the oscillator's position x and momentum p as $\hat{X}(0) = \hat{x}(0)$ and $\hat{Y}(0) = \hat{p}(0)/(m\omega_{\mathrm{m}})$, where m is the mass. As such, the quadratures satisfy the commutation relation $[\hat{X}, \hat{Y}] = i\hbar/(m\omega_{\mathrm{m}}) = 2ix_{\mathrm{zpf}}^2$. This commutation relation gives rise to an uncertainty relationship as well as quantum fluctuations.

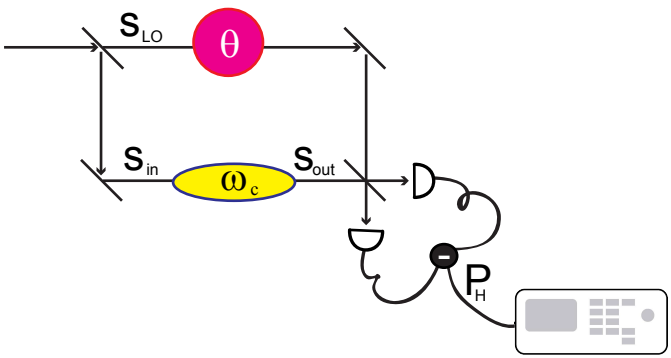

Figure 2.1: Graphical representation of a homodyne setup. The incoming laser beam is split by a beam splitter into two beams: local oscillator (s_{LO}) and signal (s_{in}). In the local oscillator arm, a phase delay θ between the reference and signal beam can be introduced. Along the path of the signal beam the cavity system under study is placed denoted by 'ω_{c}'. The interaction of the signal beam with the cavity results in the beam s_{out}. The beams are recombined at a 50:50 beam splitter, generating two beams that each carry information from both the LO and signal path. These lead to two detected interference signals on photodiodes. The signals are subtracted and constitute the output signal of the homodyne interferometer P_{H}.

For a single-mode optical field, the quadratures can be measured individually by employing homodyne detection [60, 62]. In figure 2.1 we show a schematic of a homodyne interferometer used to measure the field emanating from an optical cavity, depicted by the yellow ellipse. A laser beam is split into two arms of a Mach-Zehnder interferometer, with the field in the 'signal' arm described by ($s_{\mathrm{in}} = |s_{\mathrm{in}}|\, e^{i\phi_{\mathrm{in}}}$) and that in the stronger 'local oscillator' arm by ($s_{\mathrm{LO}} = |s_{\mathrm{LO}}|\, e^{i\phi_{\mathrm{LO}}}$). By convention, we normalize all fields s_i such that $|s_i|^2$ is the photon flux in beam i. After interacting with the cavity, whose frequency we seek to probe, the signal

[2] They are obtained from the lab-frame operators through substitution $\hat{a} \to \hat{a}e^{-i\omega_m t}$.

field s_{out} impinges on the final beam splitter, where it is combined with the local oscillator field. By changing the local oscillator arm length, a controllable phase delay ϕ_{homo} is added to the local oscillator reference beam. At the 50:50 beam spitter the recombination of the two beams leads to $s_+ = 1/\sqrt{2}(i s_{\text{out}} + s_{\text{LO}})$ and $s_- = 1/\sqrt{2}(i s_{\text{LO}} + s_{\text{out}})$ which are detected by photodiodes as powers P_+ and P_-.

The detected photocurrents are subtracted, to produce a measured signal that can be expressed as the difference of the effective optical powers $P_{\text{H}} = P_+ - P_-$. In a quantum formalism, with the optical fields described by annihilation operators $\hat{s}_i$, the associated operator of this observable is

$$\frac{\hat{P}_H}{\hbar\omega_0} = \hat{s}_+^\dagger \hat{s}_+ - \hat{s}_-^\dagger \hat{s}_- = i(e^{-i\phi_{\text{homo}}} \hat{s}_{\text{LO}}^\dagger \hat{s}_{\text{out}} - e^{i\phi_{\text{homo}}} \hat{s}_{\text{LO}} \hat{s}_{\text{out}}^\dagger), \tag{2.4}$$

where ω_0 is the optical frequency. With a large coherent local oscillator field, we can write this in terms of the signal field quadratures as

$$\frac{\hat{P}_H}{\hbar\omega_0} = 2|s_{\text{LO}}|(\hat{X}_{\text{out}} \sin\theta - \hat{Y}_{\text{out}} \cos\theta), \tag{2.5}$$

where $\theta = \phi_{\text{LO}} - \phi_{\text{in}} + \phi_{\text{homo}}$ is the phase difference between the arms of the interferometer and the quadratures are now normalized by the vacuum field amplitude. We recognize that by varying θ between 0 and 2π in equation 2.5, we can choose for a specific quadrature of the signal field to be measured: where $\theta = 0$ and $\theta = \pi/2$ are the extreme cases of detecting the *phase quadrature* $\hat{Y}_{\text{out}}$ or the *amplitude quadrature* $\hat{X}_{\text{out}}$, respectively. Most commonly, a homodyne interferometer is operated such that the optical phase quadrature is measured.

We note that the measured photocurrent will generally encode both a signal that is to be measured, such as a displacement-induced modulation of the signal field, and the quantum (shot) noise in the detected quadrature. Indeed, homodyne detection allows measuring even very small signals with quantum noise-limited sensitivity, as the large local oscillator field $|s_{\text{LO}}|$ can effectively amplify the detected field above the electronic noise floor of the detector. This is important in our measurements since we want to drive the optical cavity with a limited amount of power. For larger power we observe unwanted nonlinear dynamics related to optomechanical backaction and thermo-optic nonlinearity. By performing homodyne detection we can perform quantum-limited detection of signal s_{out} while driving the system within a linear regime of operation. Moreover, since the balanced detector subtracts the interference signals $|s_+|^2$ and $|s_-|^2$, the output signal does not present classical laser amplitude or phase noise that is present in the interferometer input. On the other hand shot noise cannot be erased since is not classically correlated among the two arms. As such, homodyne measurements offer many benefits towards the detection of optical quadratures that is shot noise limited [64].

2.2.1. INPUT-OUTPUT THEORY OF A GENERAL CAVITY SYSTEM

The output beam s_{out} (see figure 2.1) carries information about the cavity system that is probed by the homodyne detection measurement. If we describe the linear

response of the cavity by a *transfer function* r such that the cavity input-output relation is $s_{\text{out}} = r\, s_{\text{in}}$, the homodyne signal reads

$$\frac{P_H}{\hbar\omega_0} = 2\,|s_{\text{in}}||s_{\text{LO}}|\,(\text{Re}\,(r)\sin\theta - \text{Im}\,(r)\cos\theta)\,. \tag{2.6}$$

For a single-mode, high-Finesse cavity, the transfer function can be described by a general resonant response [65]

$$r = ce^{i\varphi} - \frac{\eta\kappa}{\kappa/2 + i(\omega - \omega_c)}. \tag{2.7}$$

The first term in this general expression describes a non-resonant channel, with amplitude c and phase φ, e.g. a direct reflection of light that does not enter the cavity. The second term describes the cavity resonance, which is characterized by the resonance frequency ω_c, cavity decay rate κ and radiative coupling efficiency $\eta \equiv \kappa_{\text{ex}}/\kappa$ where κ_{ex} is the decay rate through the radiative coupling channel, i.e., radiated into the beam s_{out}. We note that in the most general case, the transfer function could still be multiplied by an overall phase factor, and we have used here a phase convention that the resonant contribution (second term in eq. 2.7) is real for large detuning. However, any global phase factor can always be absorbed in a proper readjustment of the phase θ when evaluating the resulting homodyne signal.

From eq. 2.6 we see that specific homodyne angles ideally probe the real or imaginary part of the cavity response, given by

$$\text{Re}\,(r) \quad = c\cos\varphi - \tfrac{\eta\kappa^2/2}{\Delta^2+\kappa^2/4}, \tag{2.8}$$

$$\text{Im}\,(r) \quad = c\sin\varphi + \tfrac{\eta\kappa\Delta}{\Delta^2+\kappa^2/4},. \tag{2.9}$$

where $\Delta \equiv \omega - \omega_c$ is the detuning of the incident laser frequency from the cavity resonance frequency.

In general, depending on the system characteristics, i.e. the number of coupling channels as well as the relative loss rates in these and the direct reflection phase, the resonant lineshapes as a function of Δ can vary strongly. This can be described in the context of Fano interference effects [66], as it arises due to the interference of a resonant and a direct (broadband) channel between input and output. In particular, the amplitude and phase of the non-resonant part of the signal s_{out} are sensitive to the experimental conditions and the characteristics of the cavity such that the detuning dependence of a specific quadrature is strongly affected.

In Fig.2.2c-f, we show, for three particular cases of Fabry-Perot cavities (Fig.2.2a), the resultant phase and amplitude of the transfer function together with the amplitude and phase quadrature as a function of detuning. From the phasor diagram (Fig.2.2b) all the plots can be retrieved easily, by noticing that, from equation 2.7, the zero for Δ corresponds to the minimum of $\text{Re}\,(r)$ in the phase convention we took in eq. 2.7. The resonance parameters c, φ, κ, η are bounded and related to each other by conservation of energy, which restricts the sum of the intensities at the output of all decay channels to be the same as the intensity at the input. Depending on the system characteristics we envision three specific

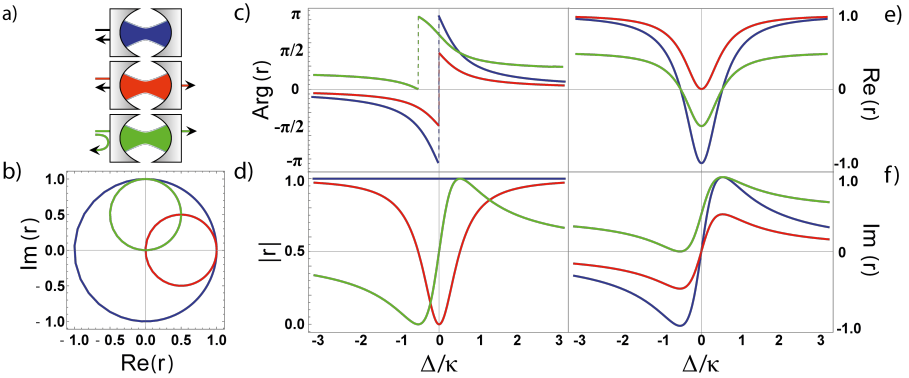

Figure 2.2: a) Three optical systems, i.e. Fabry-Pérot cavities with different coupling channels. In blue the case of a single sided cavity with only one resonant channel, in red the case of a double sided cavity with two resonant coupling channels and in blue the case of a double sided cavity plus a non-resonant channel. b) The parametric plot shows the transfer function in the complex plane for the three cavities with the same color convention, whereas c-d) are the amplitude and phase of the complex transfer function versus laser detuning and e-f) its real and imaginary parts.

cases of optical systems with different coupling channels, which can be related to Fabry-Perot models with specific mirror reflectivities: a *single sided* cavity ($c = 1$, $\varphi = 0$, $\kappa = 1$, $\eta = 1$), a *double sided* cavity ($c = 1$, $\varphi = 0$, $\kappa = 1$, $\eta = 0.5$) and a double sided cavity with *back reflection* from the first mirror ($c = 1/\sqrt{2}$, $\varphi = \pi/4$, $\kappa = 1$, $\eta = 1/2$). It is clear that in general, one obtains a Fano lineshape for the reflected amplitude $|r|$, which can vary from a dispersive to absorptive (Lorentzian) shape depending on the value of ϕ. The Lorentzian lineshape is characteristic of relative phases between resonant and non-resonant channels that are 0 or π. The standard double sided Fabry-Perot cavity is an example, which has full transmission on resonance and large reflectance for large detuning. But in the more complex systems that we study in this thesis, also the dispersive lineshapes can be encountered when we probe a nanophotonic cavity in reflection employing a free space optical beam.

2.2.2. INTRODUCING MECHANICAL FLUCTUATIONS: MEASURING CAVITY DETUNING IN TIME

The effect of small modulation of a cavity resonance frequency $\delta\omega_c$, as the one caused by mechanical vibrations (see section 1.2), is translated into the measured signal in the form of fluctuations of the homodyne output. In the presence of a modulation of the cavity frequency, the laser detuning Δ that appears in the definition of the optical field quadratures (equation 2.9) becomes time-dependent via the cavity resonance frequency:

$$\Delta(t) = \bar{\Delta} + \delta\Delta(t) = \omega - \bar{\omega}_c - \delta\omega_c(t), \tag{2.10}$$

where $\delta\Delta$ and $\delta\omega_c$ denote the detuning and cavity resonance frequency fluctuations, and the horizontal bars denote mean values (equal to the value for the mechanical

resonator at rest). In order to address mechanical fluctuations we want to measure the fluctuations of the homodyne signal $P_H(t) = \bar{P}_H + \delta P_H(t)$. The general expression for the output signal $P_{\mathrm{H}}(t)$ that follows from equations 2.6 and 2.7 is

$$\frac{P_{\mathrm{H}}(t)}{\hbar\omega_0} = |s_{\mathrm{in}}||s_{\mathrm{LO}}|\left[-2c\sin(\theta+\varphi) + \frac{\kappa_{\mathrm{ex}}}{\Delta^2(t)+\kappa^2/4}(-2\Delta(t)\cos\theta + \kappa\sin\theta)\right], \quad (2.11)$$

from which it follows that

$$\frac{\delta P_{\mathrm{H}}(t)}{\hbar\omega_0} = 2\delta\omega_c(t)|s_{\mathrm{in}}||s_{\mathrm{LO}}|\frac{\kappa_{\mathrm{ex}}}{\left(\bar{\Delta}^2+\kappa^2/4\right)^2}\left[\kappa\bar{\Delta}\sin\theta - \left(\bar{\Delta}^2 - \frac{\kappa^2}{4}\right)\cos\theta\right]. \quad (2.12)$$

Equation 2.12 represents the full expression for the fluctuations of the homodyne signal which transduces the cavity fluctuations. This is the ultimate observable we want to have access to if we are aiming for mechanical measurements. The measured signal is maximally sensitive to a displacement x that shifts the cavity frequency by $\delta\omega_c = Gx$ when we choose $\bar{\Delta} = 0$ and $\theta = 0$.

Moreover, monitoring the signal due to a known fluctuation while the laser frequency is swept across the resonance allows extraction of the system parameters ω_c, κ, and κ_{ex}. At first sight, it seems from eq. 2.12 that measured modulations $P_H(t)$ do not depend on the non-resonant reflection, described by c and ϕ in the first term on the right hand side of equation 2.7. However, in practical experimental scenarios the non-resonant response can still strongly affect the measured signal. This is particularly true if the laser frequency is swept. It is related to the way that θ is set experimentally, which does not allow to keep it at a single well-determined value as eq. 2.12 suggests. Fluctuations in the length of the interferometer arms often necessitate an active control over the local oscillator arm length, for example by moving a mirror in the local oscillator arm on through piezoelectric actuation which feeds back on a measured signal. This control is accomplished by fixing the average output signal $\bar{P}_H$ to a constant value. But since $\bar{P}_H$ *does* depend on the values of c and ϕ, the resulting drawback is that also δP_H become dependent on those parameters through the phase θ. Indeed, the practical value of θ is found by solving

$$\bar{P}_H = -2|s_{\mathrm{in}}||s_{\mathrm{LO}}|\left(\mathrm{Re}\,(r)(\bar{\Delta})\sin\theta + \mathrm{Im}\,(r)(\bar{\Delta})\cos\theta\right) \quad (2.13)$$

for a particular chosen value of $\bar{P}_H$. For example, if we keep $\bar{P}_H = 0$ as is most conventionally done, we have

$$\theta(\bar{\Delta}) = \arctan\left(-\frac{\mathrm{Im}\,(r)(\bar{\Delta})}{\mathrm{Re}\,(r)(\bar{\Delta})}\right) + 2\pi n, \quad (2.14)$$

where n is an integer. If instead we maximize the difference between the balanced detectors such that $\partial\bar{P}_H/\partial\theta = \mathrm{Re}\,(r)(\bar{\Delta})\cos\theta - \mathrm{Im}\,(r)(\bar{\Delta})\sin\theta = 0$ we obtain

$$\theta(\bar{\Delta}) = \arctan\left(\frac{\mathrm{Re}\,(r)(\bar{\Delta})}{\mathrm{Im}\,(r)(\bar{\Delta})}\right) + 2\pi n. \quad (2.15)$$

Either of these expressions varies with $\bar{\Delta}$ and as a result these settings do not necessarily probe the phase or amplitude quadrature for all laser frequencies.

Moreover, if c and ϕ are not precisely known, even at detuning $\bar{\Delta} = 0$ the probed quadrature is not determined. Especially for the free-space interaction with complex nanophotonic systems such as photonic crystals, to make quantitative predictions about the non-resonant reflection one should acquire knowledge about the optical setup configuration such as optical beam size and relative polarization between optical cavity mode and signal beam polarization [67]. The values of c and ϕ can vary from sample to sample and depend strongly on optical alignment. In fact, in the systems we study it is often impossible to measure c and ϕ as the reflectance $|r|$ as shown in Fig. 2.2 cannot be directly observed because of large fluctuations and/or (optomechanical) nonlinearities. In the next section we present a method that overcomes these experimental difficulties and allows faithful extraction of system parameters in the presence of an unknown background signal, simplifying the requirements on the experimental protocol.

2.3. PARAMETER ESTIMATION FROM CONTINUOUS MEASUREMENTS

2.3.1. TRANSDUCTION FUNCTION AND POWER SPECTRAL DENSITY

In a practical implementation, the output signal of the homodyne interferometer $P_H(t)$ is handled by an electronic spectrum analyzer which measures the spectrum of fluctuations $\delta P_H(t)$ and quantifies these in terms of power spectral density. Thanks to the Wiener-Khinchin theorem we can retrieve an operational relationship that connects the measured power spectral density of fluctuations to the theoretical Fourier transform of the auto-correlation function of the measured quantity [25]. For example, the power spectral density $S_{\omega\omega}$ of fluctuations of frequency ω is

$$S_{\omega\omega}(\Omega) = \int \langle \omega(t)\omega(0)\rangle \, e^{i\Omega t} dt, \tag{2.16}$$

where Ω is the Fourier frequency. For future reference, we introduce here also the concept of a symmetrized power spectral density defined as

$$\bar{S}_{\omega\omega}(\Omega) = \frac{1}{2}\left(S_{\omega\omega}(\Omega) + S_{\omega\omega}(-\Omega)\right). \tag{2.17}$$

We note that if two variables are linearly (and instantaneously) related via $x = ay$, their spectral densities are related through $S_{xx} = a^2 S_{yy}$. If we assume that the amplitude of the modulation $\delta\omega_c(t)$ is much smaller than the cavity linewidth κ, the variation of P_H can be approximated by the Taylor expansion truncated to first order: $\delta P_H(t) = \frac{\partial \bar{P}_H}{\partial \bar{\omega}_c}\delta\omega_c(t)$, as we did in eq. 2.12. In this case it is possible to write an analytical expression for the transduction from a given fluctuation spectrum of ω_c (or x) to P_H: the spectral density of the frequency fluctuations $S_{\omega\omega}$ is related to the measured signal from the spectrum analyzer $S_{P_H P_H}$, by means of the relationship [68]

$$S_{P_H P_H}(\Omega) = \beta P_{\text{in}} P_{\text{LO}} S_{\omega\omega}(\Omega), \tag{2.18}$$

where we have introduced the *transduction function* β. The expression for the transduction function depends on the employed detection method. In figure 2.3 we

show β as a function of the laser detuning $\bar{\Delta}$ for homodyne detection. In this case the transduction function $\beta(\bar{\Delta},\eta,\kappa,\theta(c,\varphi))$ is a function of five parameters:

$$\beta = \left(\frac{2\eta\kappa}{\left(\bar{\Delta}^2+\kappa^2/4\right)^2}\right)^2 \left[\kappa\bar{\Delta}\sin\theta(c,\varphi) - \left(\bar{\Delta}^2 - \frac{\kappa^2}{4}\right)\cos\theta(c,\varphi)\right]^2. \tag{2.19}$$

For the two choices of fixing θ outlined in the previous section, one can make predictions for $\beta(\bar{\Delta})$, with the knowledge of all parameters, by using the expressions for θ derived in equations 2.14 and 2.15, respectively. Figure 2.3 shows the transduction function for the three cavities depicted in figure 1, fixing the homodyne phase to maximize $\bar{P}_H$. In principle, it is thus possible to determine system parameters through fitting by measuring the transduction function β as a function of detuning by evaluating $S_{P_H P_H}(\bar{\Delta})$ for a known cavity modulation spectrum $S_{\omega\omega}$ (for example due to thermomechanical fluctuations of a resonator at known temperature). However due to the large number of parameters to be determined from a fit of a full model of beta, a successful result that allows the determination of the parameters is not guaranteed. In the next section we propose an alternative operation of the homodyne interferometer that allow us to overcome this difficulty and achieve a simple understanding of the experimental data and extraction of the transduction function parameters.

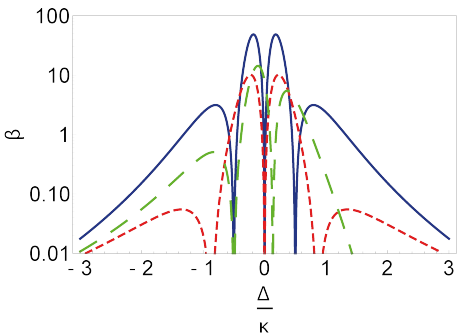

Figure 2.3: Transduction function versus laser detuning. The plot shows the respective transduction for the three cavities shown in figure 2.2. Color convention unchanged: single sided cavity (blue), double sided cavity (red), double sided cavity plus a non-resonant channel (green).

2.3.2. QUADRATURE-AVERAGED HOMODYNE DETECTION

We now show that modulating continuously the phase of the reference beam of the interferometer removes the dependence of the homodyne signal (equation 2.12) on the non-resonant scattering parameters. The measurement probes only the resonant channel of the optical system, described by the second term of equation 2.7. Importantly, the method can be used to detect a signal corresponding to the average over the field quadratures, instead of providing a measurement of a selected quadrature. In this sense it constitutes an alternative use of an homodyne interferometer that normally is used for single quadrature detection, see section 2.5. The advantage of the method is that any single-mode optical system gives a simple Lorentzian signal corresponding to the resonance of the optical mode when laser frequency is tuned. Moreover no feedback scheme is needed, which simplifies the experimental protocol.

If the relative phase between the homodyne interferometer arms is ramped linearly in time as $\theta = 2\pi\nu t$, and if the time of acquisition is sufficiently large (meaning that the signal is collected at least for θ between 0 and 2π), we can average $\langle \delta P_H^2 \rangle$ over time. Using equation 2.19 and

$$\begin{aligned} \int_\tau dt \cos^2(2\pi\nu t) &= \frac{1}{2\pi}\int_0^{2\pi} d\theta \cos^2\theta = \frac{1}{2}, \\ \int_\tau dt \sin(2\pi\nu t)\cos(2\pi\nu t) &= \frac{1}{2\pi}\int_0^{2\pi} d\theta \sin\theta\cos\theta = 0, \end{aligned} \tag{2.20}$$

we arrive at an expression for the transduction of the form

$$\beta_{\mathrm{QA}}(\bar{\Delta},\kappa,\eta) = \frac{2\eta^2\kappa^2}{\left(\kappa^2/4+\bar{\Delta}^2\right)^2}. \tag{2.21}$$

The transduction assumes a simple dependence on the cavity resonance parameters. This allows a simple analysis of the experimental data that requires only the most relevant fitting parameters for each value of the laser frequency, in order to determine the characteristic parameters of the cavity resonance. In figure 2.4 we show that β_{QA} assumes the same detuning dependance for all the cases depicted in figure 2.2. This has to be compared with the result of figure 2.3.

The drawback of the method is a decreased sensitivity that amounts to a maximum of a factor of two, with respect to the ideal case of detection of an optimal single quadrature. To derive this decreased sensitivity we compare the case of a single-sided Fabry-Pérot cavity for which the sensitivity is maximum, at $\bar{\Delta} = 0$. From equation 2.19 we obtain

$$\beta(\bar{\Delta}=0) = 64\frac{\eta^2}{\kappa^4}\cos^2\theta = 2\cos^2\theta\,\beta_{\mathrm{QA}}(\bar{\Delta}=0), \tag{2.22}$$

which shows that for an optimal homodyne detection (with $\theta = 0$) the transduction is twice that of the quadrature averaged method. Equivalently we could notice that the way we operate the homodyne interferometer, where one arm of the interferometer is phase modulated, has an analogy to heterodyne detection but

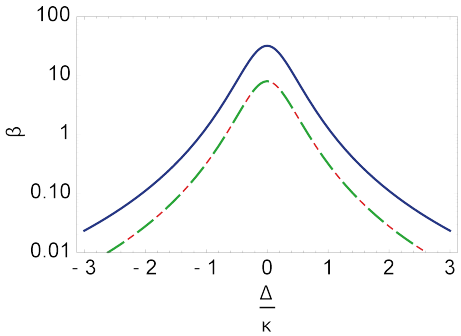

Figure 2.4: Transduction function for quadrature averaged homodyne detection. The plot shows the respective transduction for the three cavities shown in figure 2. Color convention unchanged: single sided cavity (blue), double sided cavity (red), double sided cavity plus non-resonant channel (green).

with a negligible frequency difference between the two beams of the interferometer. In this perspective, one can see that a 3 dB sensitivity decrease corresponds well with the fundamental limitation on the signal to noise ratio of heterodyne detection with respect to homodyne detection [60].

2.3.3. APPLICATION TO SLICED PHOTONIC CRYSTAL NANOBEAM RESONATORS

We apply these techniques to retrieve the characteristic parameters of the sliced photonic crystal nanobeam systems introduced in section 1.3, by employing the setup depicted in figure 2.5. The setup is a homodyne interferometer, section 2.2, with a mirror in the reference beam path whose position is controlled by a piezoelectric element. By modulating the mirror position, and hence the length of the reference beam arm, the homodyne phase θ is swept with a slow triangular waveform, such that it linearly varies over 2π in a time of approximately 100 ms. In this way we can operate the homodyne interferometer in the quadrature averaged mode discussed in section 2.3.2. The cavity is probed in reflection. Its transfer function is of the general type discussed in section 2.2.1, containing a non-resonant signal. We use a New Focus Velocity 6700 (1430 – 1510 nm bandwidth) tunable narrowband diode laser to probe the sample enclosed in a closed cycle cryostat Montana C2. The two interferometes beams are detected by a Newport balanced homodyne detector (900 – 1700 nm wavelength range) with a bandwidth of DC - 80 MHz and analyzed by an electronic spectrum analyzer (ESA) Rohde & Schwarz 10 Hz–3.6 GHz bandwidth. Moreover, we employ a cross-polarizer system composed of quarter wave plate (at 0°) and polarizing beam splitter, which allow us to filter the reflected signal that has the same polarization of the nanobeam cavity mode.

The homodyne signal processed by an electronic spectrum analyzer (ESA) presents mechanical peaks at the characteristic frequency of the mechanical flexural mode of the nanobeam cavity. We show such a measured mechanical peak in figure 2.5. The power spectral density shown by the ESA can be converted to

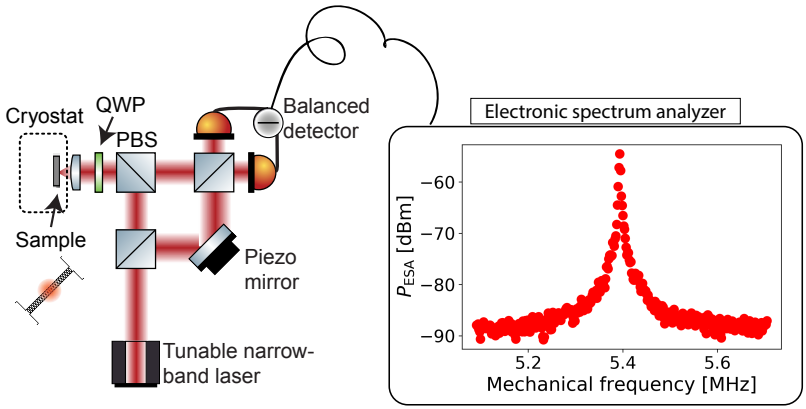

Figure 2.5: Homodyne setup for continuous measurements. The basic scheme is already explained in figure 2.1, here the signal arm contains the nanobeam cavity (inside a cryostat) probed in reflection through a variable cross polarizer that consists of the quarter wave plate QWP and polarizing beam splitter PBS. In the reference beam path a piezoelectric stage controls the position of a movable mirror. The output signal of the balanced detector is sent to an electronic spectrum analyzer. An example of a spectrum of thermal displacement fluctuations recorded by the ESA is reported. The mechanical peak is due to a mechanical mode at about 5.39 MHz.

a displacement spectral density through a linear calibration. The displacement spectral density corresponds to the thermomechanical noise spectrum of a damped harmonic oscillator, on top of a white noise background due to optical shot noise. The area under the peak corresponds to the variance of mechanical displacement that is proportional to the temperature of the thermal bath coupled to the system. The linewidth is the mechanical linewidth Γ [3]. If the temperature is independently known, and the probing power is small enough such that the mechanical resonator is not heated or cooled, this means that the measurement of thermal noise can be used to calibrate the transduction factor.

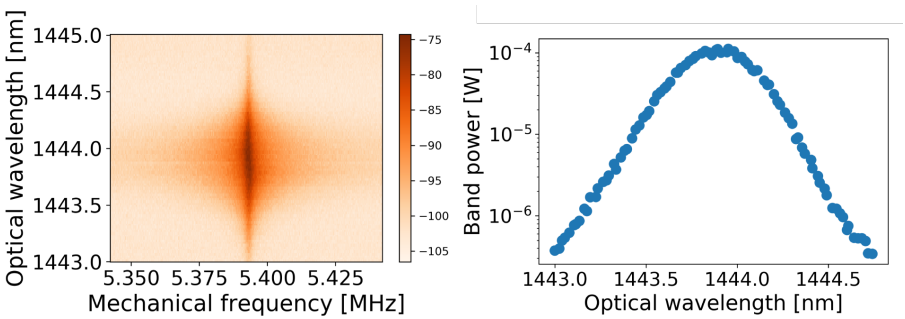

Figure 2.6: Spectrogram relative to the mechanical peak shown in figure 2.5, color bar indicates the power spectral density in units of dBm. By integrating the spectrum for each value of the optical linewidth one obtains the band power as a function of optical linewidth, as shown on the right plot.

We call the integral of the peak in the power spectrum the *band power*. By plotting its value for each value of the laser detuning we can retrieve the full dependence of the transduction function to be compared with the theoretical prediction of figure 2.4. We report an example of such a measurement in figure 2.6. When the cavity frequency fluctuations are small, it is possible to directly extract from the band power linewidth the optical decay rate κ. However, we observe in our devices that due to the large optomechanical coupling, described by g_0/κ, the optical response is strongly affected by the mechanical fluctuations due to the Brownian motion of the nanobeam. This behavior ultimately depends on the thermal occupancy of the mechanical mode. The amplitude of the cavity frequency fluctuations due to the thermal motion of the mechanical resonator is described by a root mean square value given by

$$\delta\omega_{\mathrm{rms}} = \sqrt{\langle\delta\omega^2\rangle} = g_0\sqrt{2n_{\mathrm{th}}} = g_0\sqrt{\frac{2k_{\mathrm{B}}T}{\hbar\omega_m}} \tag{2.23}$$

where n_{th} is the thermal occupancy of the environment at temperature T to which the mode with frequency ω_m is coupled. For our devices at room temperature the relative cavity fluctuations $\delta\omega_{\mathrm{rms}}$ regularly exceed the optical linewidth κ.

Importantly, due to these large thermal fluctuations we observe a *thermal broadening* of the optical linewidth. Figure 2.7 shows this effect on simulated optical band power spectra for various temperatures, that we compare with Lorentzian squared (blue) and Gaussian squared (green) lineshapes fitted to the simulated points. The simulation is done by taking a number of values ($\sim$ 1000), for the resonance frequency of the cavity ω_c, randomly from a Gaussian distribution, centered at the bare cavity resonance frequency and having κ_{eff} as FWHM. Using those values of ω_c in the expression for the transduction, equation 2.21, and taking the average over all of the values at every detuning the band power figures are reconstructed. We compare the simulated points with a Gaussian function and a Lorentzian squared function for different values of the temperature. We see that the broadening affects the band power at higher temperatures, where the lineshape resembles more a Gaussian than a Lorentzian. For a proper description, the predicted Lorentzian squared shape of equation 2.21 in the presence of thermal broadening must be convoluted with a Gaussian probability distribution describing the thermomechanical fluctuations of the cavity frequency. Figure 2.8 shows the extracted full-width at half maximum of a Voigt lineshape, which models the convolution of a Lorentzian and a Gaussian lineshape, versus temperature for a particular sample. We extract the linewidth by fitting the squared Voigt function to the band power as a function of laser frequency. In the limits $\kappa \gg \delta\omega_{\mathrm{rms}}$ or vice versa, this value then corresponds to either the optical decay rate κ or the Gaussian linewidth $2\sqrt{2\log 2}\delta\omega_{\mathrm{rms}}$, respectively. We use an empirical equation for the linewidth of a Voigt lineshape [69]

$$0.5346\kappa + \sqrt{0.2166\kappa^2 + 8\log 2\,\delta\omega_{\mathrm{rms}}^2} \tag{2.24}$$

and the known sample temperature for each data point to extract the values of κ and g_0 from the temperature dependence of the linewidth. This method thus

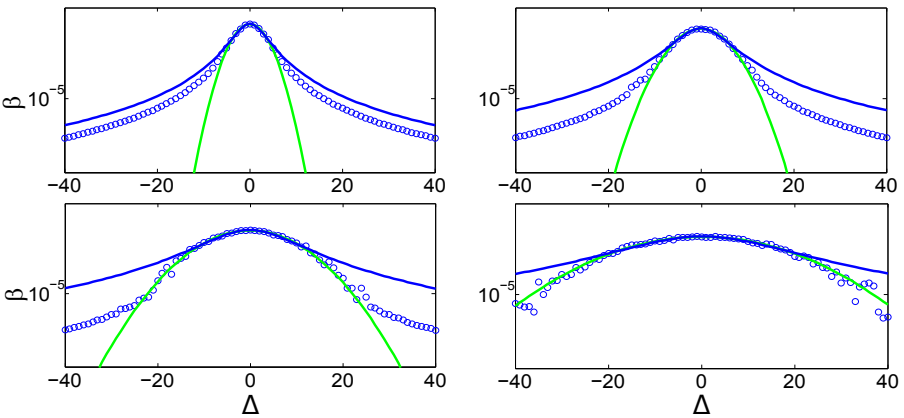

Figure 2.7: We plot the transduction function of equation 2.21 versus detuning Δ. The circles correspond to simulated points, while the blue line corresponds to a Lorentzian squared fit. In green we plot the Gaussian fit. From top to bottom the temperature is equal to $T = 3, 12, 48, 150$K respectively. The other parameters chosen for the simulation are: $g0 = 10.5$MHz, $\omega_m = 5.8894$MHz, $\kappa = 5$GHz. [70]

provides a robust method to retrieve the important parameters g_0 and κ for each sample (figure 2.8).

2.4. NONLINEAR TRANSDUCTION

In the previous section we have explained how large cavity frequency fluctuations due to thermomechanical motion result in the apparent broadening of the optical linewidth with respect to the intrinsic optical cavity linewidth. Importantly, this regime leads to a related effect in our systems that strikingly impacts the mechanical spectra: the occurrence of spectral peaks at frequencies that correspond to the higher harmonics of the mechanical modes frequencies. We denote this effect by *nonlinear transduction*: the mechanical vibrations are transduced by the optomechanical cavity in a nonlinear fashion leading to the creation of sidebands at higher harmonics of the actual mechanical mode frequencies, in a process similar to mixing of the radiofrequency sidebands.

The mechanism can be understood by observing the real and imaginary quadratures of the cavity frequency response r in Fig. 2.2. For small fluctuations of the cavity frequency, these quadratures vary linearly around the value for the mean detuning $\bar{\Delta}$. But if the excursions of the cavity frequency, and thus also the effective detuning Δ for a given laser frequency, approach or exceed κ, the measured signal samples a significant part of the dispersive or absorptive lineshape. As a result, even if the underlying mechanical motion and corresponding cavity frequency is modulated harmonically, the time-varying measured signal can be far from harmonic and is thus composed of multiple harmonics. In figure 2.9 we show an example of a measured fluctuation spectrum in which the occurrence of nonlinear transduction is evident. Notably only two mechanical modes are responsible for all observed peaks in the spectrum. In the figure they are named f_1

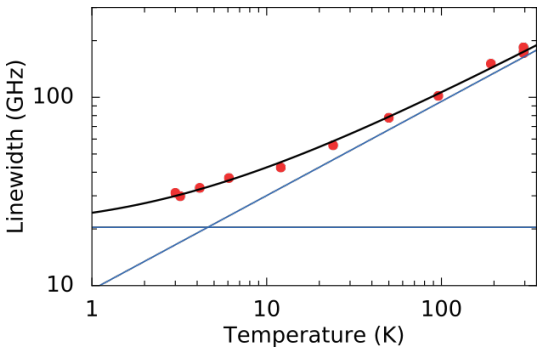

Figure 2.8: Optical linewidth versus temperature. The red dashed line is a fit with a model that assumes a constant Lorentzian intrinsic linewidth κ convolved with a Gaussian with a width that depends on $\sqrt{T}$. The asymptotes (blue) of the fit function allow us to extract κ and the optomechanical coupling rates g_0.

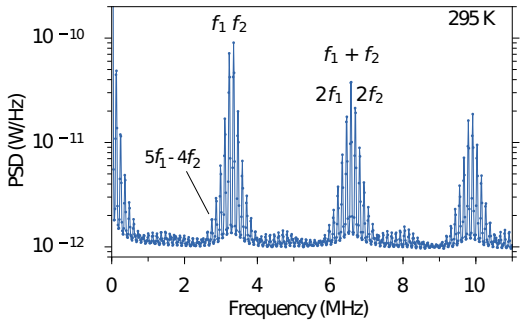

Figure 2.9: Power spectrum of transduced thermal motion obtained at room temperature. The spectrum shows two mechanical peaks at frequencies $f_1, f_2 \approx 3.3$MHz that are nonlinearly transduced.

and f_2 and correspond to independent fundamental in-plane flexural vibrations of the individual nanobeam halves. The other peaks appear at frequencies that correspond to linear combinations of these: $af_1 + bf_2$, where a and b are integers. We show for example in the figure a peak at $5f_1 - 4f_2$ corresponding to a 9th order nonlinear harmonic.

2.4.1. GENERALIZATION OF THE TRANSDUCTION MODEL FOR HIGHER HARMONICS

In section 2.3.2 we showed that, by averaging the homodyne output signal over different field quadratures, we obtain a simple expression for the transduction β that describes how the fluctuations of a cavity frequency emerge in the output signal. Our calculations relied on the assumption that the amplitude of cavity frequency modulations $\delta\omega$ is small compared to the cavity linewidth κ. In this regime we could approximate the output signal P_H by neglecting higher order terms in its Taylor expansion. In other words, the calculated function β_{QA} (equation 2.4) describes *linear transduction*. Entering the regime of large fluctuations does not lead to a

convergent result for our simplified analytical model. However we can calculate the onset on nonlinear transduction in an intermediate regime in which we still assume that the fluctuations are relatively small. We will then show how this regime differs from the large amplitude case which we model numerically, and compare the results with the experimental evidence.

Considering harmonic frequency modulation $\delta\omega(t) = A\cos(\Omega t)$, the Taylor expansion of the homodyne signal $P_H(t)$ is

$$P_H(t) = \sum_{k=0}^{\infty} \frac{1}{k!} \frac{\partial^k P}{\partial \Delta^k} [A\cos(\Omega t)]^k. \tag{2.25}$$

For small modulation $A \ll \kappa$ we can make the approximation:

$$\cos^k(\Omega t) \simeq \frac{1}{2^{k-1}} \cos(k\Omega t), \tag{2.26}$$

since, when A is small, the convergence of the sum is ensured by cutting the sum index to a finite value. The relationship in equation (2.26) allows to write $P(t)$ as a Fourier series

$$P_H(t) = \sum_k \frac{1}{k!} \frac{\partial^k P}{\partial \Delta^k} \frac{A}{2^{k-1}} \cos(k\Omega t) = \sum_k P_k(t). \tag{2.27}$$

By noticing that every term $P_k(t)$ is linear in $\cos(k\Omega t)$, we can write kth-order transduction functions $\beta_{\mathrm{QA,k}}$ that correspond to each term with harmonic frequency $k\Omega$ for quadrature-averaged homodyne detection.

In order to derive an expression for the transduction, we need to evaluate $\langle [\partial^k P/\partial\Delta^k]^2 \rangle_\theta$. We group some constant factors and rewrite δP_H as

$$\frac{\delta P_H}{\hbar\omega_0 |s_{\mathrm{in}}||s_{\mathrm{LO}}|} = 4\eta \frac{(x\cos\theta + \sin\theta)}{1+x^2} = 4\eta(f\cos\theta + g\sin\theta) \tag{2.28}$$

where $x = 2\Delta/\kappa$ and $f = x/(1+x^2)$, $g = 1/(1+x^2)$, so that

$$\begin{aligned} \left\langle \left(\frac{\partial^k P}{\partial \Delta^k}\right)^2 \right\rangle &= \left(\frac{\kappa}{2}\right)^{-2k} \left\langle \left(\frac{\partial^k P}{\partial x^k}\right)^2 \right\rangle \\ &= \left(\frac{\kappa}{2}\right)^{-2k} (4\eta)^2 \left\langle \left(\partial^k (f\cos\theta) + \partial^k (g\sin\theta)\right)^2 \right\rangle \\ &= \left(\frac{\kappa}{2}\right)^{-2k} (4\eta)^2 \frac{1}{2} \left[(\partial^k f)^2 + (\partial^k g)^2 \right]. \end{aligned} \tag{2.29}$$

Since both $(\partial^k f)^2$ and $(\partial^k g)^2$ are real valued we can write

$$(\partial^k f)^2 + (\partial^k g)^2 = (\partial^k f + i\partial^k g)(\partial^k f - i\partial^k g). \tag{2.30}$$

In view of linearity of the derivative we can write

$$\frac{\partial^k}{\partial x^k}(f + ig) = \frac{\partial^k}{\partial x^k}\left(\frac{x+i}{1+x^2}\right) = \frac{\partial^k}{\partial x^k}\frac{1}{x-i} = (-1)^k (x-i)^{-(k+1)} k!, \tag{2.31}$$

which means that we can write an expression for the k-th order derivative of both f and g.

Equation (2.30) becomes

$$(\partial^k f)^2 + (\partial^k g)^2 = \frac{(k!)^2}{(x^2+1)^{k+1}}$$

this ultimately implies that

$$\langle \left[\frac{\partial^k P_H}{\partial \Delta^k} \right]^2 \rangle_\theta = P_{\rm in} P_{\rm LO} \left(\frac{\kappa}{2}\right)^{-2k} (4\eta)^2 \frac{1}{2} \frac{(k!)^2}{(x^2+1)^{k+1}}, \tag{2.32}$$

where $P_{\rm in} = |s_{\rm in}|^2$, $P_{\rm LO} = |s_{\rm LO}|^2$.

We can call $S_{P_k P_k}$ the PSD of the k-th term in equation (2.27), so that

$$S_{P_k P_k} = P_{\rm in} P_{\rm LO} \beta_{{\rm QA},k} \delta(\Omega - \Omega_k), \tag{2.33}$$

and from equation (2.27) and (2.33) it follows that

$$\beta_{{\rm QA},k} = \left(\frac{A}{\kappa}\right)^{2k} \frac{(4\eta)^2}{(x^2+1)^{k+1}}. \tag{2.34}$$

For $\Delta = 0$, we look at the ratio of the second to the first order transduction as a function of the *modulation strength* defined as the ratio between the modulation amplitude and the cavity linewidth A/κ:

$$R = \frac{S_{\rm P_2P_2}}{S_{\rm P_1P_1}} \left(\frac{A}{\kappa}\right)\Big|_{\Delta=0} = \frac{\beta_{\rm QA,2}}{\beta_{\rm QA,1}} \left(\frac{A}{\kappa}\right)\Big|_{\Delta=0} = \left(\frac{2\delta\omega_{\rm rms}}{\kappa}\right)^2, \tag{2.35}$$

where in the last step we consider that, for Brownian motion, the fluctuation amplitude A corresponds to $\delta\omega_{\rm rms}$. Thus, comparison of the band powers of the different harmonics for quadrature-averaged homodyne detection allows, with knowledge of $n_{\rm th}$, an unambiguous estimation of the ratio g_0/κ.

For large modulations $A \geq \kappa$, the approximation in (2.26) is no longer valid. In this case it is only possible to give a numerical estimate for the transduction at higher orders since we cannot anymore exploit the convergence of the truncated Taylor expansion valid for small perturbations. In figure 2.10 we show the comparison with the experimental results. The experimental points are obtained by taking the ratio of the band power integral (see section 2.3.3) of the first and second order spectral peaks, when the laser is on resonance with the cavity. We indicate this quantity as A_{2f}/A_f. Also in this regime, the comparison of the band power ratio to the numerically obtained prediction allows determination of the g_0/κ ratio. The data are collected at different temperature, which varies the value of $\delta\omega_{\rm rms}$ through the mechanical thermal occupancy. We observe that the band power ratio deviates from the small-modulation approximation especially for larger values of $\delta\omega_{\rm rms}$. The correspondence of data an calculation shows that, for a sample at a given temperature, the calculated dependence can be used to extract an estimation of

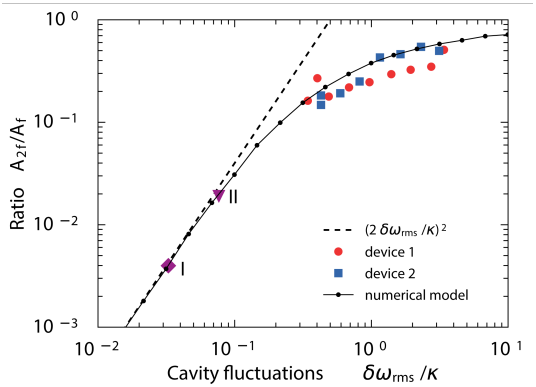

Figure 2.10: Ratio between the 3 second-order peaks around $f1+f2$ and the peaks at the fundamental frequencies $f1$, $f2$ as a function of the relative cavity fluctuations $\delta\omega_{\mathrm{rms}}/\kappa$ for two devices (blue and red data points). Device 1 is the same device presented in figure 2.9; room-temperature measurements from two publications are indicated with data points I (ref.[71]) and II (ref.[50]). The dashed line indicates the prediction from an analytical model with the approximation of equation 2.26, while the black data points connected with solid lines represent a calculation based on a numerically generated time trace to simulate thermal motion.

the ratio $\delta\omega_{\mathrm{rms}}/\kappa$ from a measurement of the ratio A_{2f}/A_f. Using the thermal occupancy n_{th}, which is generally well-known at low laser power, this provides us with an estimate of the ratio g_0/κ. And together with a detuning dependence of the band power and equation 2.24, this can be used to estimate g_0 and κ independently, even if the temperature is not varied. We demonstrate this procedure in chapter 5.

2.5. PULSED MEASUREMENTS

In the previous sections, we introduced balanced homodyne detection as a way to selectively probe the quadratures of an optical field. We discussed how we use continuous homodyne measurements to characterize an optomechanical cavity. Here, we review the basics of the method of pulsed optomechanical measurements, which allow to selectively probe the quadratures of a *mechanical* resonator. These provide a way to perform backaction-evading measurements of a mechanical resonator as discussed in section 1.1.1, in the so-called bad cavity regime, where $\kappa \gg \omega_m$ [44, 72]. Pulsed displacement measurements, with durations that are much smaller than a mechanical period, allow to measure 'instantaneous' position with an imprecision that is related to the shot noise on the number of photons in the pulse. For large enough power, this imprecision can be smaller than the standard quantum limit, i.e. the width of the mechanical ground state x_{zpf}.

The main idea is that pulsed measurement probes only one of the two non-commuting quadrature variables, while measurement backaction affects only the orthogonal, unmeasured quadrature. If we consider the mechanical quadratures $\hat{X}_m$ and $\hat{Y}_m$ in a frame rotating at the mechanical frequency ω_m, the mechanical

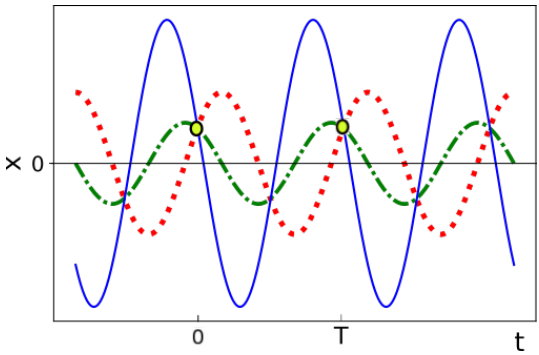

Figure 2.11: Different mechanical trajectories with random amplitudes and phases but the same frequency, which all intersect at the same (non-zero) x position at $t = 0$ and $t = T$. Pulsed measurement can make predictions at specific times while having no certainty of the momentum (i.e. all times in between).

evolution can be written as

$$\hat{x}(t) = \hat{X}_m(t)\cos(\omega_m t) + \hat{Y}_m(t)\sin(\omega_m t), \tag{2.36}$$

where the two quadratures are slowly varying to sample the thermal distribution at a timescale that is the inverse of the mechanical dissipation rate Γ. They diffuse randomly in phase space at the thermal decoherence rate $n_{\rm th}\Gamma$, or in other words they remain equal to within the precision of the mechanical ground state size within one decoherence time $1/n_{\rm th}\Gamma_m$. An optical homodyne measurement of the phase quadrature of a pulse leaving the cavity at $t = 0$ will yield a result that is linearly proportional to the mechanical position quadrature $\hat{X}_m$. Because no knowledge is gained on the momentum quadrature $\hat{Y}_m$, the harmonic trajectory immediately after the measurement cannot be predicted from the single measurement alone, as indicated in Fig. 2.11. However, exactly one mechanical period T later, a second pulsed measurement would give the same result up to the measurement imprecision, if thermal decoherence in time T is negligible, as it probes again the same quadrature. The first measurement thus allows to predict the outcome of the second, with a precision that can in principle be better than the standard quantum limit. The imprecision noise is fundamentally given by the shot noise of the photons in the pulse, which can be a coherent state. A lower bound to this noise can be derived from a simple consideration. The optical phase change due to a quadrature displacement δX is $\delta\phi = 4g_0\delta X/\kappa$ in an ideal, single-sided cavity [3]. The number-phase uncertainty relationship $\delta N\delta\phi \geq 1$ then dictates that a pulse of N photons (with shot noise uncertainty $\delta N = \sqrt{N}$) can yield a minimum quadrature imprecision of $\delta X > \kappa/(4g_0\sqrt{N})$. In other words, a single pulse can reach imprecision below the ground state amplitude if $\sqrt{N} > \kappa/(8g_0)$. Measurement backaction is manifested as the force that the photons in the pulse exert, which affects only the mechanical momentum quadrature $\hat{Y}_m$ if the pulse duration is very short. This backaction consists of both a coherent part, proportional to the mean photon number $\bar{N}$, and a stochastic part that is due to the $\sqrt{N}$ shot noise

fluctuations. This stochastic force thus adds uncertainty to the system, but only to the unmeasured quadrature. It does ensure that the uncertainty of the product of both quadratures always obeys Heisenberg's uncertainty principle, regardless of the strength of the measurement. We will return to this in Chapter 4. We note here already that if the pulse has a finite duration, the stochastic fluctuations of the optical amplitude quadrature can affect the mechanical position quadrature. However, a careful analysis reveals that a potential detrimental effect of this only matters significantly when the pulse duration becomes as large as $\sim T/2$ [32, 44]. The above explanations concerned an idealized optomechanical cavity. In the following two chapters, we will encounter multiple factors that lead to additional noise sources and challenges in pulsed optomechanical measurement. We discuss their description and mitigation in detail there.

CONCLUSIONS

In this chapter we have given an overview of the technical tools we employ in the remaining part of the thesis. We introduced homodyne interferometry and described how it can be used to investigate optomechanical systems. We analyzed cavity systems with different coupling channels. We showed how to model the outcome of measurements of the cavity frequency fluctuations due to mechanical motion in the different systems. Moreover we introduced the homodyne operational mode of quadrature-averaging which can be beneficial in the characterization of optomechanical systems. We showed that our systems, characterized by large optomechanical coupling rates, have a nonlinear response while undergoing Brownian motion. This leads to artifical broadening of the optical linewidth and occurrence of higher order sidebands in the mechanical spectra. We showed that in the regime of nonlinear transduction we can numerically predict the system behaviour. Pulsed measurements, at the core of this thesis were briefly introduced, with their ability to predict mechanical quadratures below the standard quantum limit.

3

NANOMECHANICAL DESIGN FOR SINGLE-MODE OPTOMECHANICAL MEASUREMENT

We present a mechanical design strategy to ensure that optomechanical measurements can retrieve information on a single mechanical degree of freedom. A spectral design approach is used to make mechanical symmetries robust against practical disorder. We evaluate the effectiveness of the method in sliced photonic crystal nanobeams, for two different application scenarios.

3.1. INTRODUCTION

In optomechanical systems, co-localizing light and mechanical oscillations enables ultraprecise sensing and optical control over mechanical motion. A variety of experiments explore mechanical resonators of different masses and sizes, spanning various mechanical designs and measurements conditions. The properties of these systems allow conceptually different applications ranging from gravitational wave sensing to photon-phonon transducers in quantum networks [73, 74]. Besides applications, optomechanics allows the fundamental study of the motion of macroscopic objects. Of particular interest is the transition from quantum to classical descriptions of mechanical motion as it occurs if an object's mass is increased from that of single isolated atoms to macroscopic mechanical objects coupled to an environment at elevated temperature. Particularly relevant for studying this transition is the class of nano- and micro-mechanical systems, which can have relatively small mass and dissipation, while still consisting of billions of trillions of atoms. Employing them, experiments can be designed to unveil fingerprints of quantum mechanical behavior of massive mechanical objects, while showing the onset of decoherence effects yet to be tested [61, 75]. In such experiments, measurements on a mechanical system can be used to characterize the quantum state of motion. Backaction evading measurements, such as pulsed measurements that probe a single quadrature of a mechanical resonator, allow to perform quantum state tomography to reconstruct a resonator's Wigner density [44]. Precise optical displacement measurement can track the evolution of a quantum state and allow to control it via feedback protocols [76–78].

A wide range of mechanical systems have been investigated in cavity optomechanics, that vary in dimension and geometry and hence masses and oscillation frequencies, and are thus suitable for different applications and experiments [3]. Depending on its specific nature, a typical mechanical system will generally show a number of mechanical modes of vibration, and not just a single one. The vibrational modes supported by a certain structure can be more or less complex depending on the structure's geometry and can be fundamentally understood in the context of the theory of elasticity to form a collection of normal modes. If the goal is to characterize and achieve control over a resonator quantum state, one typically wishes to estimate the state of only a single mechanical mode. Other modes affecting the measured signal cause noise on that estimation, and thus limit control. While ideally optomechanical experiments envision the coupling of an optical mode to a single mechanical mode, systems in practice always show multiple modes. The coupling of mechanical modes other than the mode of interest to the optical cavity is often detrimental, limiting the level of effective sensitivity and control that can be achieved. This is the case in feedback cooling experiments where the signal of an optical mode whose phase is sensitive to mechanical motion is used to produce a negative feedback on the oscillator to damp its motion [77, 78]. Likewise, it limits the ability of a pulsed position measurement to estimate a single quadrature of a single mechanical resonator while evading backaction, as any instantaneous measurement probes all modes at once [44, 59].

Optomechanical design can be used to isolate the optical sensitivity to a single

favorable mechanical mode. In particular, the use of structural symmetries can decrease the sensitivity to spurious modes in various cases such as nanobeam cavities [16, 50, 79]. There, unwanted asymmetric mechanical modes do not couple to the 'symmetric' optical cavity mode as their displacement does not affect the effective cavity length. However, then any fabrication imperfection that breaks symmetry limits the effectiveness of this method in practice, as it can induce symmetry breaking in the mechanical modes of interest. Here, we present and experimentally implement a strategy to mitigate the effect of unwanted mechanical modes, 'purifying' the optomechanical spectral response of a structure around a single mechanical degree of freedom. We will examine in detail the importance of noise contributions due to the presence of spurious modes, quantifying these by defining suitable figures of merit. We argue how spectral design of the system can optimize these figures of merit even in the presence of perturbations due to random fabrication imperfections. We then implement this design strategy in the specific example of a sliced photonic crystal nanobeam cavity. We report the mechanical performance of experimental realizations, and evaluate the figures of merit for varying designs, demonstrating the impact of the chosen strategy in realistic scenarios. We finally discuss how the strategy can be interpreted in a model of two coupled modes. We show that as such also radiation-pressure-induced coupling can be used to implement the strategy, and evaluate the effectiveness of such a method.

3.2. NOISE IN OPTOMECHANICAL MEASUREMENTS INDUCED BY SPURIOUS MODES

In ideal optomechanical measurements one wants to study a certain mechanical mode, that is for instance designed to exhibit an interesting quantum state or to be coupled to a quantum system that one wants to sense. In actual experiments, measurements on this mode are disturbed by the presence of modes other than the mode of interest. Here we examine the scenario in which the measurement is affected by the coexistence of an extra mode that is nearly degenerate with the designed mode of interest and couples weakly to the same meter. We treat the presence of spurious modes as extra noise sources that differ for different measurement conditions.

In the presence of two mechanical modes, with resonance frequencies Ω_1 and Ω_2, we characterize the contribution of the excess imprecision noise due to the presence of mode at Ω_1 in a measurement of that at Ω_2 (the mode of interest) in the case of continuous measurements and in the case of instantaneous pulsed measurements. In the presence of two independent mechanical modes, as described in section 1.2 the cavity frequency can be written as

$$\omega_c(x_1, x_2) = \bar{\omega}_c + \frac{\partial \omega_c}{\partial x_1} x_1 + \frac{\partial \omega_c}{\partial x_2} x_2 = \bar{\omega}_c + G_1 x_1 + G_2 x_2, \tag{3.1}$$

where $x_{1,2}$ are the displacements defined for each mode and $G_{1,2}$ are the frequency shift per unit displacement for each mode.

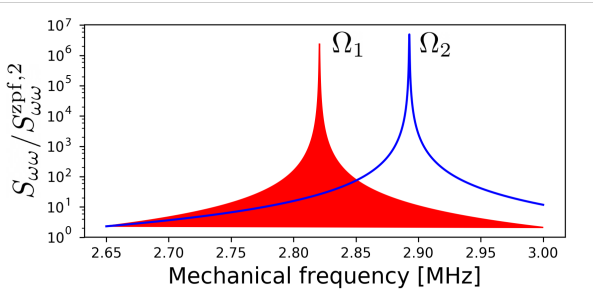

Figure 3.1: Illustration of typical frequency fluctuation spectra due to two mechanical resonances at frequencies Ω_1 and Ω_2. The noise spectral density originating from mode 1 is filled in red. The wing of the Lorentzian of mode 1 is directly linked to the added imprecision noise at the resonance frequency of mode 2. To characterize the imprecision added to a measurement of mode 2 due to the presence of mode 1, we look at the value of the fluctuations of mode 1 at the frequency Ω_2.

3.2.1. NOISE IN CONTINUOUS MEASUREMENTS INDUCED BY A SPURIOUS MODE

In continuous measurements an optomechanical device is probed by a light field with constant intensity over a time span that is much longer than a single mechanical period ($\gg 2\pi/\Omega_m$). The mechanical fluctuations that act as a parametric modulation of the optical resonance frequency (equation 3.1) can be studied in the frequency domain, as fluctuation spectra (Fig.3.1).

The spectral density of optical frequency fluctuations $S_{\omega\omega}(\Omega)$ leads to in terms of the position spectral density $S_{xx}(\Omega)$, that is easily comparable with experimental data. In the case of two uncorrelated mechanical modes

$$S_{\omega\omega}(\Omega) = G_1^2 S_{x_1 x_1}(\Omega) + G_2^2 S_{x_2 x_2}(\Omega), \tag{3.2}$$

where $S_{x_i x_i}(\Omega)$ is the displacement spectral density of each mode ($i = 1,2$).

The response of one resonator to a driving force F_{ext} is described by the susceptibility $\chi(\Omega)$, such that $x(\Omega) = \chi(\Omega)F_{\mathrm{ext}}(\Omega)$ where

$$\chi(\Omega) = \frac{1}{m(\Omega_m^2 - \Omega^2) - im\Gamma\Omega}, \tag{3.3}$$

with m the mass of the mechanical oscillator and Γ the linewidth. This relation can be expressed in terms of power spectral densities as: $S_{xx}(\Omega) = \left|\chi(\Omega)\right|^2 S_{FF}^2$. It quantifies the noise on the position variable due to the response of one resonator to an external fluctuating force described by S_{FF}.

The frequency spectral density can then be written as

$$S_{\omega\omega}(\Omega) = G_1^2 \left|\chi_1(\Omega)\right|^2 S_{F_1F_1}^2 + G_2^2 \left|\chi_2(\Omega)\right|^2 S_{F_2F_2}^2, \tag{3.4}$$

where numbers in subscripts refer again to the two mechanical modes whose contribution can be described independently. We consider here the case of thermally driven mechanical oscillators, in which case the driving force can be

expressed by the thermal Langevin force with fluctuations $S_{F_iF_i} = 2\Gamma_i m k_B T$, where k_B is the Boltzmann constant and T the temperature.

The magnitude of $S_{\omega\omega,1}(\Omega_2)$ quantifies the impact of frequency fluctuations of mode 1 at the frequency of mode 2, Ω_2. As sketched in Fig.1, the fluctuations constitute a noise contribution that affects measurements of mode 2 and is only due to the presence of mode 1. To arrive at an expression for the figure of merit we write

$$S_{x_1x_1}(\Omega_2) = \left|\chi_1(\Omega_2)\right|^2 S_{F_1F_1} = \tag{3.5}$$
$$= \frac{4\Gamma_1 k_B T x_{\mathrm{zpf},1}^2}{\hbar} \frac{\Omega_1}{(\Omega_2^2-\Omega_1^2)^2+\Gamma_1^2\Omega_2^2},$$

where we used (3.3) and $x_{\mathrm{zpf},i}^2 = \hbar/(2m_i\Omega_i)$ the zero-point fluctuation variance of mode i. Defining $\Delta\Omega \equiv \Omega_2 - \Omega_1$ and assuming that the mechanical modes are spaced by more than their linewidths ($\Gamma_1 \ll \{\Omega_1, \Delta\Omega\}$), the spectral density of these fluctuations at Ω_2 can be approximated by

$$S_{x_1x_1}(\Omega_2) = \frac{4\Gamma_1 k_B T x_{\mathrm{zpf},1}^2}{\hbar} \frac{\Omega_1}{\Delta\Omega^2(\Delta\Omega+2\Omega_1)^2}. \tag{3.6}$$

Importantly, for quantum measurements it is useful to compare any noise contribution with the zero point fluctuation amplitude of the mode of interest. For example, in feedback cooling protocols a negative feedback loop is created in which a displacement measurement is used to generate an optical drive of the right amplitude and frequency that produces a radiation pressure force such as to damp the resonator's motion. Any noise on this signal will set a limit on the amount of cooling that one can achieve, since it will be fed back to the force that acts on the resonator. If the goal is to reach the quantum ground state any mechanical noise contribution needs to have a magnitude below that of the ground state amplitude. The cavity fluctuations due to the ground state of the mode of interest are

$$\bar{S}_{\omega\omega}^{\mathrm{zpf},2} = \frac{2g_{0,2}^2}{\Gamma_2}. \tag{3.7}$$

We can thus finally define a figure of merit as

$$\frac{S_{\omega\omega}^{\mathrm{th},1}}{\bar{S}_{\omega\omega}^{\mathrm{zpf},2}} = 2\frac{k_B T}{\hbar}\Gamma_1\Gamma_2\frac{g_{0,1}^2}{g_{0,2}^2}\frac{\Omega_1}{\Delta\Omega^2(\Delta\Omega+2\Omega_1)^2}, \tag{3.8}$$

where we use the relation $g_0 = Gx_{\mathrm{zpf}}$. We see that the imprecision due to the unwanted mode scales with temperature, as the spurious mode population increases with it, with the ratio between the photon-phonon coupling rates of the two modes, and with the linewidths of both modes, as it scales effectively with the overlap of the two modes' response spectra. It scales with $\Omega_1^{-1}\Delta\Omega^{-2}$ for mode separations that are larger than the linewidths but smaller than the smallest mode frequency. For larger separations, and if the mode of interest has larger frequency than the spurious mode, the figure of merit scales with $\Omega_1\Delta\Omega^{-4}$ instead.

3.2.2. NOISE IN PULSED MEASUREMENTS INDUCED BY A SPURIOUS MODE

In pulsed optomechanical measurements, the mechanical resonator is probed by light pulses that are shorter than the mechanical oscillation period [44]. What is important for these measurements is the ability to predict the outcome of a measurement of a harmonic oscillator quadrature, given a previous measurement of the same quadrature. In other words we look at the difference between the outcome of a position measurements performed with a time delay of exactly one mechanical period. Keeping the convention of the last paragraph, T_2 is the period of the mode of interest. The difference between the two mode frequencies implies a difference in the oscillation periods that in turn implies an uncertainty on the difference of two measurements of position $\Delta x_\tau = x(\tau) - x(0)$, with $0 < \tau \leq 2\pi/\Omega$, except when τ is a common multiple of T_1 and T_2, as we will see in chapter 4. We quantify the mechanical decoherence added by a second mechanical mode by considering the expected variance of Δx_τ for two mechanical modes at any delay τ which is extracted through measurement of the cavity frequency $\omega_c = \bar{\omega}_c + \sum_i \delta\omega_i(x_i)$, where $\delta\omega_i$ is the cavity frequency shift due to the mode i and $\bar{\omega}_c$ the cavity frequency for all $x_i = 0$. We write the displacement-induced shifts $\delta\omega$ in terms of the quadratures (see section 2.2) $X_{m,i}$, $Y_{m,i}$ of the two modes ($i = 1,2$):

$$\delta\omega = \sum_i G_i (X_{m,i} \cos\Omega_i t + Y_{m,i} \sin\Omega_i t). \tag{3.9}$$

Ideally, if only mode 2 couples to the cavity, its quadratures can be determined from measurement of the cavity frequency through $\delta\omega/G_2$. The thermal fluctuations of other modes evolving at different frequencies at specific times t adds uncertainty to such estimations. For thermal motion, the variance of the individual quadratures is given by $\langle X^2_{m,i}\rangle \simeq x^2_{\mathrm{zpf}} k_B T/\hbar\Omega_i = x^2_{\mathrm{zpf}} n_{\mathrm{th},i}$, in the limit where $n_{\mathrm{th}} \gg 1$. Consequently the variance due to two contributions is the sum of their variances. At a generic time τ, the position of mode i relative to its position at $t = 0$ can be written as

$$\Delta x_{\tau,i} = x_i(\tau) - x_i(0) = \sqrt{2} x_{\mathrm{zpf},i} \left[X_{m,i}(\cos\Omega_i\tau - 1) + Y_{m,i} \sin\Omega_i\tau \right]. \tag{3.10}$$

By writing the time dependence of the quadrature variables in the cosine and sine terms, $X_{m,i}, Y_{m,i}$ are independent variables, i.e. they are no longer the time derivative each other, which means that their cross-correlations vanish, to calculate the variance of the differences

$$\langle \Delta x^2_{\tau,i}\rangle = 2\langle X^2_{m,i}(\cos\Omega_i\tau - 1)^2 + Y^2_{m,i}(\sin\Omega_i\tau)^2\rangle \tag{3.11}$$

$$= 4 x^2_{\mathrm{zpf},i} n_{\mathrm{th},i}(1 - \cos\Omega_i\tau). \tag{3.12}$$

The second line is valid for thermal states, where $\langle X^2_{m,i}\rangle = \langle Y^2_{m,i}\rangle$ due to the equipartition theorem. This means that the variance on the difference $\Delta\omega_c$ between two measurements of the cavity frequency taken at time τ apart reads

$$\langle \Delta\omega^2_\tau\rangle = \sum_i 4 g^2_{0,i} n_{\mathrm{th},i} (1 - \cos(\Omega_i\tau)) \tag{3.13}$$

in absence of decoherence during τ. From equation 3.13 we see that if the mechanical modes have comparable frequency and optomechanical coupling, they have nearly identical contributions to the variance when $\tau = T_i/4$ or $\tau = T_i/2$, since for delays around those values, $1-\cos\Omega_i\tau \simeq 1$ or $1-\cos\Omega_i\tau \simeq 2$, respectively. Importantly, for $\tau = T_i$, where for a single mode the difference vanishes, the other mode j still contributes to the variance of the difference

$$\langle \Delta\omega^2_{T_i}\rangle = 4g^2_{0,j}\, n_{\mathrm{th},j}\left(1-\cos\frac{2\pi T_i}{T_j}\right). \tag{3.14}$$

Now we consider the case of only two modes, with labels $i, j = 1,2$ so that we can retrieve the figure of merit

$$\frac{\langle \Delta\omega^2_{T_2}\rangle}{g^2_{0,2}} = 4\frac{g^2_{0,1}}{g^2_{0,2}}\, n_{\mathrm{th},1}\left(1-\cos\frac{2\pi\Omega_1}{\Omega_2}\right), \tag{3.15}$$

where we again compare the uncertainty added by the spurious mode to the cavity frequency shift $g_{0,2}$ of a quantum-level displacement of the mode of interest. Equation 3.15 scales again with the ratio of vacuum coupling rates of both modes, with the mean occupation number of the unwanted mode, and as a factor $\left(1-\cos\frac{2\pi\Omega_1}{\Omega_2}\right)$ that measures the relative dephasing of the two modes, i.e. it is equal to zero when the two modes are exactly degenerate.

3.2.3. COMPARISON

We want to now compare the two figures of merit that we list again here:

$$\frac{S^{\mathrm{th},1}_{\omega\omega}}{\bar{S}^{\mathrm{zpf},2}_{\omega\omega}} = 2\frac{k_B T}{\hbar}\Gamma_1\Gamma_2\frac{g^2_{0,1}}{g^2_{0,2}}\frac{\Omega_1}{\Delta\Omega^2(\Delta\Omega+2\Omega_1)^2}, \tag{3.8}$$

$$\frac{\langle \Delta\omega^2_{T_2}\rangle}{g^2_{0,2}} = 4\frac{g^2_{0,1}}{g^2_{0,2}}\frac{k_B T}{\hbar\Omega_1}\left(1-\cos\frac{2\pi\Omega_1}{\Omega_2}\right). \tag{3.15}$$

We can easily identify commonalities and differences. In particular both expressions are proportional to $g^2_{0,1}/g^2_{0,2}$, while if we look at the dependence on Ω_1 and Ω_2 we can see that a difference in the frequencies will be beneficial if one wants to minimize the continuous measurement figure of merit (3.8), while the pulsed measurement figure of merit (3.15) contains an oscillating term $0 \leq \left(1-\cos\frac{2\pi\Omega_1}{\Omega_2}\right) \leq 2$ that vanishes for small frequency difference or in the peculiar circumstance that Ω_1 is very close to an integer multiple of Ω_2.

Even though equations 3.8 and 3.15 have different forms, because of the different dependency on the frequencies Ω_1 and Ω_2, both figures of merit are obviously optimized when the ratio of optomechanical coupling rates $g_{0,1}/g_{0,2}$ is minimized. We will address and quantitatively compare the full figures of merit later in the chapter. We first focus on strategies to minimize the ratio of coupling rates. One way to do so is to rely on symmetries in the system at hand. If a mode of a specific symmetry is designed to be parametrically coupled to the light, by making sure

that spatial overlap between mechanical and optical modes exists, then a mode of opposite symmetry would be 'invisible' (or 'dark'), having zero effective overlap. However, in various systems, such as pairs of vibrating beams or membranes, modes of opposite symmetry are close in frequency. Then, in practical realizations, retaining those symmetries is often challenging because of imperfections. The process of fabrication of mechanical resonators suited for cavity optomechanics experiments is indeed not immune to disorder. In the next section we describe a strategy for the design of a more robust solution that relies on controlling the frequency difference of the normal modes, in order to enforce mode symmetry also in the presence of disorder. We will then compare how this affects the figures of merit for the two considered measurement scenarios.

3.3. ROBUST MODE SYMMETRIES IN OPTOMECHANICAL SYSTEMS

Understanding the influence of disorder to symmetry breaking in actual systems can be done in the context of perturbation theory. Here we will consider how a pair of orthogonal modes (i.e. *normal modes*) $\psi_1^{(0)}$ and $\psi_2^{(0)}$ that are near but not at degeneracy are affected by disorder. We follow the formalism of Cotrufo et al. [80]. The disorder can be described by a potential $\hat{V}(r,t)$, which modifies the eigenvalues of the system. In nondegenerate perturbation theory, one can calculate the new energy eigenvalues by

$$\begin{aligned} E_1' &= E_1^{(0)} + \langle \psi_1^{(0)} | \hat{V} | \psi_1^{(0)} \rangle \\ E_2' &= E_2^{(0)} + \langle \psi_2^{(0)} | \hat{V} | \psi_2^{(0)} \rangle \end{aligned}, \tag{3.16}$$

where $E_i^{(0)}$ are the eigenvalues for the bare system, in the absence of perturbation. The second term in equation 3.16 that describes the change of the eigenvalues is nonzero if the potential has some non-zero diagonal elements.

If the case that the potential also has off-diagonal elements, for example caused by an asymmetric disorder, also the eigenfunctions will be modified, giving rise to a different spatial configuration of the modes. This can be written as

$$\begin{aligned} |\psi_1'\rangle &= |\psi_1^{(0)}\rangle + \frac{\langle \psi_2^{(0)} | \hat{V} | \psi_1^{(0)} \rangle}{E_1^{(0)} - E_2^{(0)}} |\psi_2^{(0)}\rangle \\ |\psi_2'\rangle &= |\psi_2^{(0)}\rangle + \frac{\langle \psi_1^{(0)} | \hat{V} | \psi_2^{(0)} \rangle}{E_2^{(0)} - E_1^{(0)}} |\psi_1^{(0)}\rangle \end{aligned} \tag{3.17}$$

Equations 3.16 and 3.17 show that in the presence of a disorder potential both the energy eigenvalues, hence the frequencies of the eigenmodes of the system, and the eigenvectors, hence the spatial configuration of the eigenmodes, is modified. In particular, equation 3.17 shows that the correction in the spatial configuration is such that it has the symmetry of the orthogonal mode. Indeed, if modes $|\psi_1^{(0)}\rangle$ and $|\psi_2^{(0)}\rangle$ are symmetric and antisymmetric, respectively, any asymmetrically

distributed disorder $\hat{V}$ will make the numerators $\langle\psi^{(0)}_{1,2}|\hat{V}|\psi^{(0)}_{2,1}\rangle$ in eq.3.17 nonzero. The consequence of this perturbation is to progressively mix the shape of the two modes as its importance increases, destroying the initial symmetries of the individual eigenmodes. For example, an initially perfectly symmetric mode may lose that quality as an asymmetric disorder mixes it with a mode of orthogonal symmetry.

In the next section we will show a practical observation of this effect in a specific geometry of interest. Experimentally we cannot eliminate the perturbation present in the fabrication process. We can try to reduce it by improving the fabrication quality of structures, but there will always be a practical limit to it. By looking once again at equation 3.17 we see that it is possible to reduce the impact of disorder in an alternative way, as the magnitude of the symmetry breaking is inversely proportional to the energy difference $E^{(0)}_1 - E^{(0)}_2$ of the modes of the unperturbed system. Thus, if one intentionally shifts the frequency of the unwanted mode further away from that of the mode of interest, each corrected eigenvector keeps the shape of the unperturbed system solution. Such a design principle thus forces the system to retain the symmetries also in presence of disorder. Controlling mode spectra through geometry is in other words a practical way to render symmetries robust against disorder. We note that the strategy presented here not only affects the ratio of the coupling rates $\frac{g_{0,1}}{g_{0,2}}$ but also the terms in the figure of merits that depend on the modes frequencies Ω_1 and Ω_2. The impact is therefore different for the two cases of continuous and pulsed measurements, which we will examine in section 3.5.

3.4. MECHANICAL DESIGN STRATEGY

The sliced photonic crystal nanobeam that we study consists of two beams that are free to oscillate and share a clamping mechanism. Each beam possesses standing modes of vibration whose frequency and amplitude are determined by the length and mass density of the beam. In a perfect structure the two beams would be the exact copy of each other, oscillating with the same frequency and amplitude. This kind of structure would present perfect normal modes of vibration, to first order: a common mode in which the beams move in plane exactly in phase and a differential mode in which the beams move in anti-phase (see Fig.3.2). From the perspective of optomechanics this idealized case is optimal since only the differential mode couples to the light field. In actual devices, fabrication imperfections result in a different mass or strain profile of the two beams. In turn this leads to different oscillation frequency (within 3% in practice) and amplitude for each beam. The intrinsic coupling between the two beams through strain in the clamping supports is usually quite weak, such that the breaking of this symmetry forces the hybridization of the modes of vibration of the individual beams to nearly vanish. The result is that each beam oscillates independently from the other (Fig.3.3a)) and the eigenmodes are neither symmetric nor antisymmetric. This implies that the sliced nanobeam typically presents two bright opto-mechanical modes that are close in frequency. Our aim is to find a nanobeam geometry that has an anti-symmetric mode that is

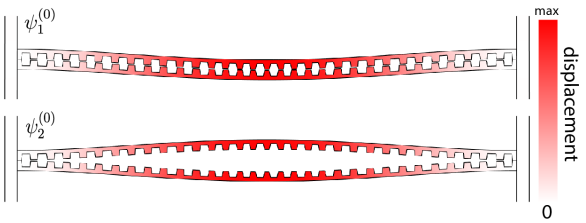

Figure 3.2: The two first order in plane modes in the ideal scenario of perfectly symmetric beam halves. The normal modes are the common (top) and differential (bottom) modes. Only the latter couples to the light field as it modifies the gap width. The two modes are just not degenerate as the beam halves are coupled through strain in the supports. Figure courtesy of Rick Leijssen.

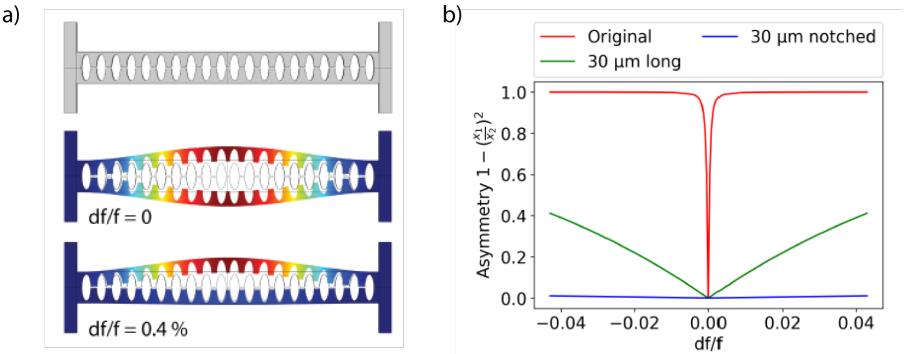

Figure 3.3: Effect of disorder in the nanobeam structures. a) When the two halves of the nanobeam are perfect and have nearly degenerate symmetric and anti-symmetric modes then both halves have equal amplitude in the anti-symmetric mode. However, even a small amount of disorder causes the motion to be fully localized in either of the halves (bottom). Here df denotes the frequency difference between the individual beams caused by disorder. In the simulation, this is controlled by changing the mass density of only the top beam half. (b) Asymmetry as a function of frequency difference between the beams for three designs: original, long, and notched structures.

immune to disorder. We quantify the asymmetry of this mode as

$$A = 1 - \left(\frac{x_{\text{up}}}{x_{\text{down}}}\right)^2, \tag{3.18}$$

where x_{up} and x_{down} are the amplitudes of oscillation of the individual beams in the center of each beam. We choose x_{down} to be always the larger so that $0 < A < 1$. The case of $A = 0$ corresponds to a perfect anti-symmetric (differential) mode. We quantify the strength of the symmetry-breaking perturbation (i.e., the strength of the disorder), by a parameter df. In the finite-element simulation, the perturbation is introduced by varying the mass density of one beam half. The parameter df is the shift of frequency that that density change induces on the fundamental flexural mode of a *single* half of the beam.

We investigate numerically how the asymmetry varies with disorder in Fig.3.3b), for structures in which we increase the length of the nanobeam outside of the

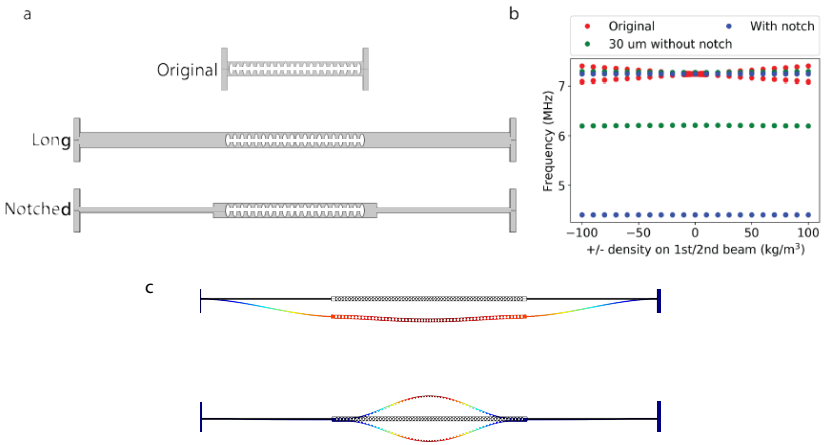

Figure 3.4: (a) Types of geometries that were used in the simulations. (b) Frequency splitting is observed in the longer and notched geometries. The lower frequency in the original and long geometry corresponds to the symmetric motion. (c) Simulated common (top) and differential (bottom) modes for the notched geometry.

photonic crystal region and the case in which we create a notched extension also outside the photonic crystal (Fig.3.4). The notched geometry gives additional protection of the anti-symmetric mode against disorder by pushing the symmetric mode to lower frequencies while maintaining the anti-symmetric mode frequency close to the original. However, it should be noted that the notched structure becomes floppy for other (higher frequency) flexural modes and lowers their frequency, bringing it closer to that of the anti-symmetric mode. This puts a practical constraint on how far the fundamental common mode can be pushed away. In Fig.3.3b) we show the asymmetry for the aforementioned structures with the geometries of Fig.3.4. The original structure is seen to quickly become fully asymmetric for small values of the asymmetry $df/f \gtrsim 0.001$. In contrast, the notched structure shows good stability against disorder even at a disorder strength $df/f \approx 0.04$. From experiments we know that for a disorder level of $df = f * 3\%$ the measured spectrum contains two peaks of equal heights corresponding to the individual motions of the two halves. The simulated asymmetry of the original structure supports this observation as we see that for disorder of 3% the asymmetry is close to unity (red curve in Fig.3.3b)). The alternative designs, in particular the notched structure, feature a much greater resilience to disorder as the frequencies of the symmetric and antisymmetric modes in the unperturbed structure are pushed much further apart.

3.5. RESULTS

We fabricate sliced nanobeams in silicon that share the design of a sliced photonic crystal in the middle, but vary in their connection to the outside, as per the design

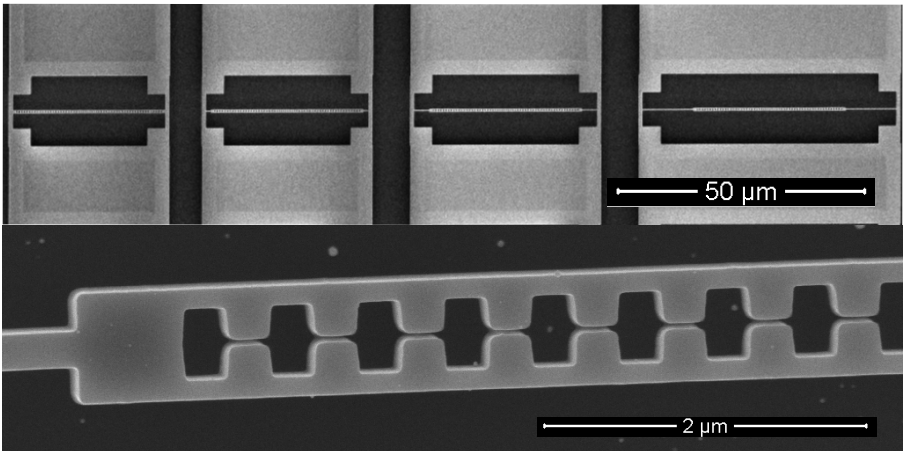

Figure 3.5: Fabricated devices that share the same photonic crystal in the middle (top). From left to right the length of the extension on both sides of the photonic crystal is of 0, 1, 3 and 10 μm. The bottom picture is a zoom in on one of the devices.

strategy of Fig.3.4. Figure3.5 reports scanning electron micrographs of fabricated structures. We vary the length of the notched extension that is symmetrically placed on both sides of the photonic crystal region. To characterize the mechanical performance we perform optical reflection measurements on the devices (as described in section 2.3.3). A focused laser beam that is tuned to resonance with the optical mode is used to excite the cavity and the reflected signal from the cavity is collected by a homodyne interferometer. The signal carries a modulation that is due to the mechanical thermal fluctuations at room temperature. The Fourier transform of the voltage signal generated by the balanced photodetector of the interferometer displays the mechanical fluctuation spectrum. A typical spectrum is shown in Fig.3.6. We can recognize a multitude of fluctuation peaks. Only three of those correspond to distinct mechanical modes frequencies, namely the first-order in-plane flexural modes (symmetric and anti-symmetric), that in this thesis we also call common and differential modes, and the third-order in-plane flexural mode. The other peaks are a signature of the large optomechanical coupling that gives rise to nonlinear transduction (see section 2.4) hence to the generation of higher harmonics in the spectrum that occur at sums of integer number of bare mode frequencies.

In this chapter we are interested in studying the response of the first order flexural modes to the modified design. In Fig.3.7 we show spectra with a span limited around those modes, for devices of the kind of those shown in Fig.3.5. The spectra shown in the figure directly represent the output of our spectrum analyzer. The signal P_{ESA} is directly proportional to the spectral density $S_{\omega\omega}$. By studying the spectra in Fig.3.7, it is possible to characterize the mechanical response around the frequency of interest. The anti-symmetric flexural mode of the sliced nanobeam is the higher frequency mode. Its frequency slightly lowers when the nanobeam length

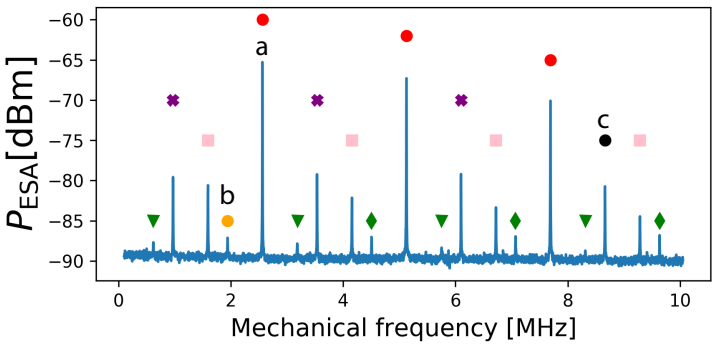

Figure 3.6: Spectrum for a structure with 10 μm notch extension. The spectrum has a bandwidth of 10 MHz and shows multiple mechanical peaks. We can recognize three distinct mechanical modes and other peaks that correspond to linear mixing of these three (section 2.4). If we call the three modes $a = 2.563603$ MHz, $b = 1.942114$ MHz and $c = 8.6619$ MHz, then we can recognize the following peaks: a, $2a$, $3a$ (red circles), b (yellow circle), c (black circle), $a-b$, $2a-b$, $3a-b$, $4a-b$ (green triangles), $a+b$, $2a+b$, $3a+b$ (green rhombus), $c-a$, $c-2a$, $c-3a$ (purple crosses) and $c-a-b$, $c-b$, $c-2a-b$, $c+a-b$ (pink squares).

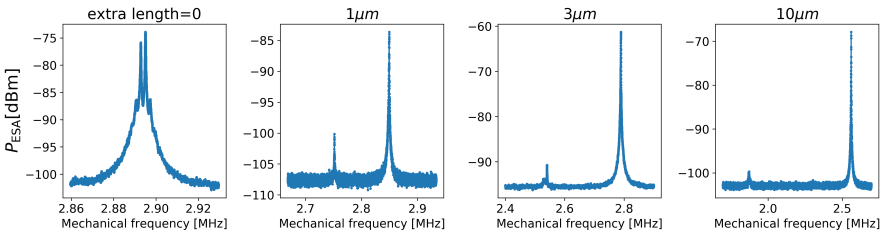

Figure 3.7: Spectra of four structures with notch length of $0, 1, 3$ and 10 μm, showing the reduced magnitude of the spurious mode of longer notch length.

becomes longer. This is potentially related to the change of the precise clamping point geometry or of the remaining compressive stress [50]. At the same time, as the notch extension becomes longer, the lower frequency mode shifts towards lower frequencies. This shift reflects the increase in the overall length of the device and follows the expected trend (see simulation results of Fig.3.4). We note that the two side-peaks in the leftmost spectrum of Fig.3.7 are due to the linear mixing of the two modes related to nonlinear transduction (see section 2.4).

In Fig.3.8 an overview of the mechanical frequencies for different notch lengths is shown, together with results obtained by calculations of the mechanical eigenfrequencies obtained for the same geometries simulated with finite-element software COMSOL. We observe a discrepancy in the absolute value of the modes frequencies when we compare simulations and the experiment (Fig.3.8a). The origin of this discrepancy is unknown: normally we would expect that the simulated frequencies would have a higher value than the experimentally observed ones,

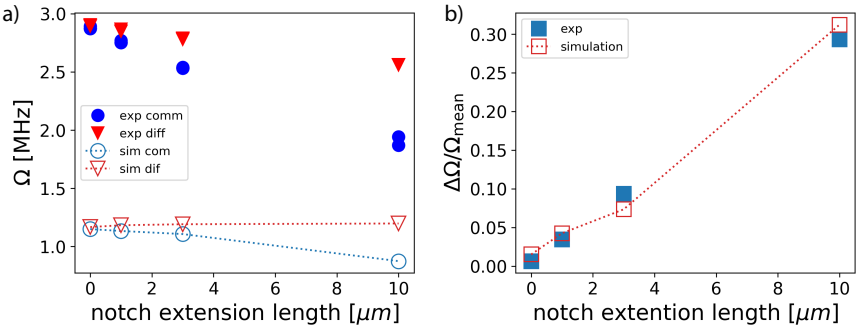

Figure 3.8: a)Frequencies of common (circles) and differential (triangles) modes for the structures in Fig.3.7 . Comparison between experimental data (full markers) and simulation results relative to the same geometries (empty markers, dashed lines). b) Relative frequency difference comparison.

due to compressive stress as shown in [50]. However, the *relative* frequency shift between the two modes as we increase the notch length is well reproduced (Fig.3.8b). As the notch length increases, also the 'band power' BP, i.e. the integral of the power spectrum

$$BP = \int_{\Delta\Omega \gg \Gamma} S_{\omega\omega}\, d\Omega, \tag{3.19}$$

associated with to the common mode, decreases[1]. In Fig.3.9 the ratio between the band power of the common and the differential mode is shown as a function of extension length. We expect the ratio to decrease monotonically as the increase in the notch length should correspond to a lower visibility (g_0) for the common mode. The trend is respected for medium lengths but seems to deviate at 10 μm. We do note that this expectation is only valid for the average fabrication asymmetry. The results we show are averaged over three realizations but statistical variations in disorder can still lead to deviations from trends predicted for fixed disorder. Finally we can see how the Lorentzian linewidths of the two mechanical modes behave as we change the overall beam length (Fig.3.10). For the longer extension (10 μm) the mechanical linewidth of the common mode increases at least a factor 4. The reason for this increase is not known, as it is contrary to the typical trend for increasing beam length. It could potentially be due to hybridization with other mechanical modes near these frequencies that exhibit larger dissipation, in particular modes of the tethered support structure.

In order to verify the efficacy of our design we now want to evaluate the figures of merit discussed in sections 1.1 and 1.2. We can use the Wiener-Khinchin theorem to relate the band power directly to the thermal fluctuations that populate the mechanical modes

$$BP = \int_{\Delta\Omega \gg \Gamma} S_{\omega\omega}\, d\Omega = \langle \delta\omega^2 \rangle_{\mathrm{th}} = G \langle x^2 \rangle_{\mathrm{th}} = 2 n_{\mathrm{th}} g_0^2 \tag{3.20}$$

[1] In the plots we use the integral of a Lorentzian fit to the experimental data and refer to it as band power BP_i where $i = 1, 2$ indicates either of the two modes.

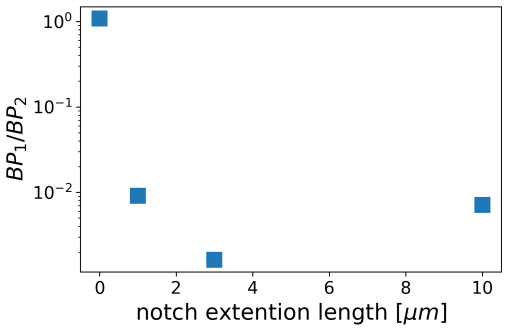

Figure 3.9: Ratio of the band powers (peak areas) of common versus differential modes for the structures above in Fig.3.7. The plot reports average values corresponding to three structures for each notch extension length.

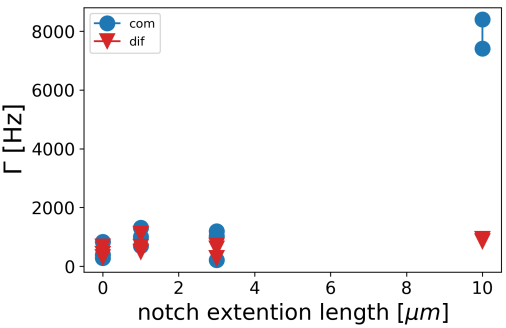

Figure 3.10: The linewidth of mode 1, Γ_1 (blue) and the one of mode 2, Γ_2 (red) versus added extra nanobeam length.

where for the last step we have used the expression for the variance of the mechanical displacement induced by thermal fluctuations $\langle x^2 \rangle_{\text{th}} = 2x^2_{\text{zpf}} n_{\text{th}} = 2x^2_{\text{zpf}} k_B T/\hbar\Omega$. Using equation 3.20, from the experimental data (Fig.3.7) we can evaluate the ratio of the single photon-phonon coupling rates g_0 of the two modes. In Fig.3.11 we plot the ratio $g_{0,1}/g_{0,2}$ of the optomechanical coupling rates of the two modes. We compare the experimental data to simulations where we plug in different amounts of disorder, by varying the relative material density of one of the nanobeam slices with respect to the other half. A disorder of 2% is found to be a typical value for fabricated devices. For comparison we also show a best case scenario of 0.2%. The data fall within the two curves indicating that structures of intermediate notch lengths suffer less from disorder. The reason for the seeming deviation from the trend at notch length of 10 μm is not fully clear: it could be of statistical origin, but we note that the strong alteration of dissipation in this design (Fig.3.10) may point to other mechanisms that could be at play.

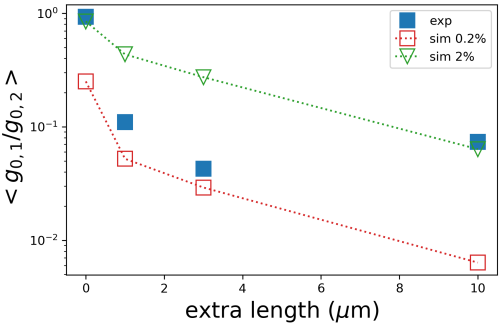

Figure 3.11: Ratio between the coupling strength of mode 1 and 2 versus extension length. Experimental points blue full squares. Two simulation curves are shown: for disorder equal to $df/f = 0.2\%$ (empty red squares, dashed line), and for disorder equal to $df = 2\% * f$ (empty green triangles, dashed line).

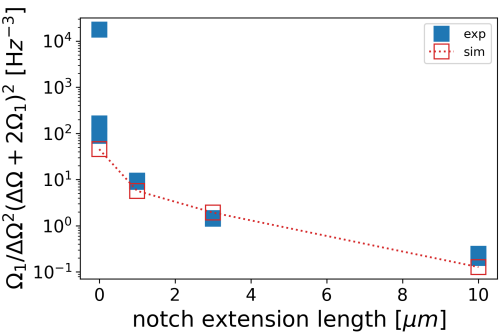

Figure 3.12: Frequency factor present in the figure of merit for continuous measurements. We rescale the frequencies in order to take into account the absolute value mismatch between simulated and measured mechanical resonance frequencies.

To construct the figure of merit for CW measurements we also need to look at the factor in equation 3.8, that depends on the mode frequencies. This factor is depicted in Fig.3.12. To compare this result to a simulated prediction, we take into account the discrepancy between simulated absolute frequencies and the experimentally measured values (Fig.3.8). We therefore rescale the predicted frequencies by a global factor such that the predicted and measured frequencies match for 0 μm notch length. The frequency factor in eq.3.8 appears to follow the same trend in experiment and simulations, except for a singular point (for zero extension) that corresponds to a device where the separation between the two modes is very small ($\sim$ 5 kHz) making the denominator of the factor blow up to a singularly high value. Finally we plot the figure of merit for CW measurements in Fig.3.13. Figure 3.13b reports the figure of merit from experiment. Increasing the length of the nanobeam, dramatically decreases the the value of the spectral density of mode 1 at the frequency of mode 2. The method therefore is indeed successful in reducing

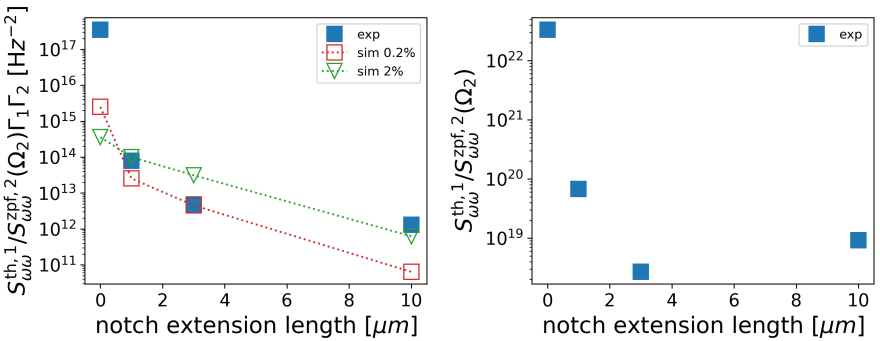

Figure 3.13: The added imprecision noise from mode 1 in a measurement of mode 2 as a function of the beam extention. a) Results of simulation together with the experimental values (blue full squares) for a modified figure of merit that rules out the mechanical linewidth that cannot be estimated by COMSOL. Two simulations curves are shown: for disorder equal to $df = 0.2\% * f$ empty red squares dashed line, and for disorder equal to $df = 2\% * f$ empty green triangles dashed line. b) Full expression for equation 3.8.

the spurious mode noise contribution. In Figure 3.13a we report a comparison of experiment and simulation. Since in the simulation no mechanical linewidths are calculated, we compare $S^{\mathrm{th},1}_{\omega\omega}/S^{\mathrm{zpf},2}_{\omega\omega}(\Omega_2)\Gamma_1\Gamma_2$ instead of $S^{\mathrm{th},1}_{\omega\omega}/S^{\mathrm{zpf},2}_{\omega\omega}(\Omega_2)$. However we observe a discrepancy between the simulated structures and the experimental evidence that is particularly relevant for longer notch extensions. Two factors could play a role: on the one hand the evident discrepancy in the prediction of the g_0 ratio compared to the experimental data. On the other hand, the stochastic nature of the occurrence of disorder means that potentially more data points are needed to draw definitive conclusions on the distribution of occurrences of a given disorder amount and dependencies that arises from the geometry. We see that structures with intermediate notch lengths are best predicted by the simulations. We note that they are easier to fabricate than longer notches, whose length could play a role for other types of phenomena that have not been taken into account such as deformations, buckling, and coupling to other mechanical modes.

For pulsed measurements, with figure of merit in equation 3.15, the same dependence on the ratio of g_0 appears as in Eq.3.8 for CW measurements, but the frequency factor is different. We report the frequency factor for pulsed measurements in Fig.3.14. Compared to the simulation the monotonic increasing trend is reproduced, even though in absolute value the experimental points are smaller since the spread in frequencies increases slower in the experiment than in the simulation, as we can see from Fig.3.8. In Fig.3.15 we show the full expression of the figure of merit. Our method is modestly successful in reducing the spurious mode contribution for relatively small values of the length of the notch extension. For longer beams, we pay the penalty that the occupation number of the common mode $n_{\mathrm{th},1} = k_B T/\hbar\Omega_1$ increases since now the frequency of the common mode is much smaller. Due to the larger frequency difference the rate at which the two

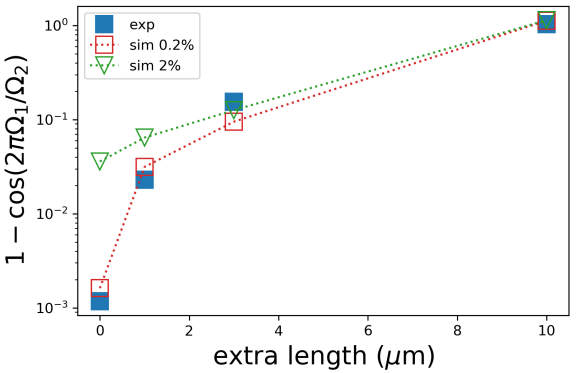

Figure 3.14: Factor dependent on the modes frequencies appearing in the figure of merit for pulsed measurements. Experimental points are blue full squares. Two simulations curves are shown: for disorder equal to $df = 0.2\% * f$ empty red squares dashed line, and for disorder equal to $df = 2\% * f$ empty green triangles dashed line.

modes dephase also increases the degree to which the first mode adds uncertainty to the prediction of a quadrature of the second mode after one full period. We remark that after some longer time, close to $2\pi/\Delta\Omega$, the mechanical modes regain the phase difference that they exhibited at $t = 0$. This allows an alternative way to minimize imprecision, as we will show in chapter 4. The increased frequency difference $\Delta\Omega$ in the notched design will reduce the time at which this occurs, potentially to within thermal decoherence times at practical temperature. This could, in some cases, make the design approach more effective also for pulsed measurement.

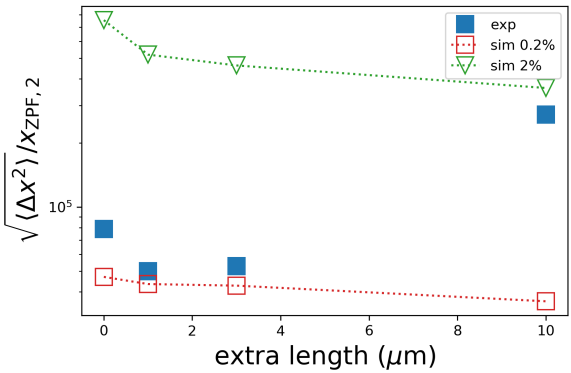

Figure 3.15: Comparison between simulation and experimental results (blue full squares) for the pulsing figure of merit of equation 3.15. Two simulations curves are shown: for disorder equal to $df = 0.2\% * f$ empty red squares dashed line, and for disorder equal to $df = 2\% * f$ empty green triangles dashed line.

3.6. LIGHT-MEDIATED MECHANICAL COUPLING

In section 5.2, we introduced the general design principle that reduces symmetry breaking due to imperfections from perturbation theory. A different but related perspective on this approach is gained from the viewpoint of coupled mode theory. We can view the mechanical system depicted in Fig.3.3 as hosting two mechanical modes, i.e. the lowest-order flexural vibration of each individual string, which are weakly coupled through the clamping support. The modes hybridize only if the coupling strength overcomes the intrinsic frequency detuning of the two strings, which is related to fabrication imperfection. The frequency splitting for degenerate strings $\Delta\Omega$ is equal to twice the rate J at which the two strings are coupled. Thus, if one increases the mechanical coupling rate, the hybridization into even and odd modes becomes more resilient to disorder. The mechanical designs we presented thus far can only be described to a limited extent from this specific viewpoint, as for larger notch lengths the new eigenmodes can no longer be described as even and odd superpositions of the individual string modes of the structure without a notch. However, we can imagine a different coupling mechanisms, in which we can describe them in this way. In this section, we explore the use of mechanical coupling of the individual strings through radiation pressure, which can lead to normal mode splitting and associated hybridization as demonstrated by Shkarin et al.[81]. Due to the orthogonality of the hybrid modes and the spatial dependence of the optomechanical coupling, such induced coupling can render one of the two new modes optomechanically dark. We demonstrate that principle below for our structures, and evaluate the merits of this optically-induced coupling for single-mode measurement.

In Fig.3.16b, we show a generic prediction of *strong coupling* for two normal modes at frequencies $\omega_{1,2}$, characterized by the Rabi frequency splitting for $\omega_1 \simeq \omega_2$, that quantifies the coupling rate between the modes. In the presence of strong

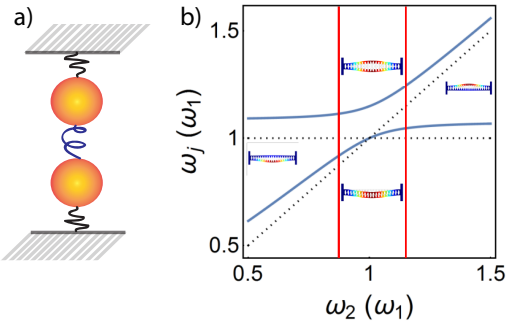

Figure 3.16: a) Illustration of two coupled oscillators. Each oscillators is represented by as a mass attached to a spring. In turn, the two oscillators share a spring that couples them to each other. b) In the presence of coupling, independent resonant modes $\omega_{1,2}$ (dashed lines) are hybridized into coupled modes (blue solid lines) with frequencies ω_j, which is plotted here as one of the bare frequencies ω_2 is varied. In the left and in the right side of the plot the hybrid modes resemble the bare modes, while in the center of the plot the hybrid modes clearly show a distinct behaviour. The shape of the normal modes in these regimes are shown for the sliced nanobeams. Both the range of detunings over which hybridization occurs, and the magnitude of the mode splitting, are given by the Rabi splitting $2J$.

coupling, coupled modes are generated, which converge to the original modes when the frequency difference $\omega_2 - \omega_1$ is large, far away from the strong coupling region which is spanned by the Rabi splitting between the coupled modes. For the coupled modes, a spring in the middle is added which produces a stiffening that is evident when comparing the coupled modes and the bare modes energies far detuned from resonance. For the nanobeams, the two uncoupled modes, characterized by the independent vibration of the individual nanobeam slices, are transformed by the coupling into an even and an odd normal mode.

Let us now consider the interaction of this system of two mechanical modes with the optical field in an optomechanical system. When the laser detuning is $0 < |\Delta| \leq \kappa$ the radiation pressure force exerted by the driving light causes an optical spring shift (section 1.2.2) that causes the mechanical frequency to decrease (increase) for red (blue) detuning. Moreover, since we are in the regime of nonlinear transduction, we observe a broadening of the mechanical resonances which become asymmetric at room temperature. For cavities in this regime (see section 2.3), the optical spring effect cannot be estimated with a model based on linearized equations of motion as the magnitude of the spring shift varies with the particular amplitude of oscillation at a given time. The behaviour in this case can be accounted for by considering the thermal distribution of the mechanical oscillation amplitude. This is done by calculating an effective spring constant from the distribution of results obtained by modeling the spring shift using the first Fourier coefficient of the radiation pressure force [82]. The light field that is modulated by the motion of one of the two mechanical modes will in turn drive the other mechanical mode. If the spring shift is such that it tunes the modes to spectrally overlap, the two modes can become degenerate. This constitutes an optically mediated coupling that can give rise to the creation of mechanical hybrid modes with opposite symmetry. The magnitude of

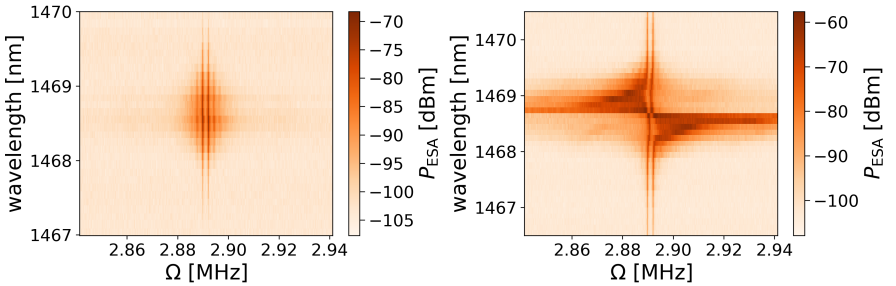

Figure 3.17: Spectra of mechanical motion expressed in dBm (color scale), as a function of laser wavelength. a) Spectrogram taken with incident power P_{in} = 440 nW. b) Spectrogram with incident power P_{in} = 34.5 μW. In a), the spectral peaks corresponding to nonlinear transduction (section 2.4) are visible at the sides of the two main peaks at Ω_1 = 2.88995 MHz and Ω_2 = 2.89214 MHz.

the induced coupling rate is maximally

$$J_{opt} = 2g_{0,1}g_{0,2}\frac{n_c}{\kappa}, \tag{3.21}$$

where n_c is the number of intracavity photons. The effect is closely connected to the spring effect for a single mechanical resonator (eq.1.10).

In Fig.3.17 we show optomechanical spectra as we scan the laser wavelength across the cavity resonance. The spectra depict the behaviour for two different regimes of power for a structure for which the separation between the frequencies of oscillation of the individual beam slices is only $\Delta\Omega = \Omega_2 - \Omega_1 \simeq 2.19$ kHz. The individual, uncoupled, behaviour of the two modes is evident at low powers (Fig3.17a) for all detunings and for high power but far detuned from resonance $|\Delta| \gg \kappa$. For high power (Fig.3.17b), in the region where the optical spring shift $\delta\Omega$ is larger than the frequency separation $\delta\Omega \gg \Delta\Omega$, we observe strong coupling between the two modes. The coupling is mediated by the light since the spring shift is caused in the first place by the optomechanical interaction. Interestingly, the coupled modes are such that the bright mode converges to the lower frequency bare mode for positive detunings (higher wavelengths) and to the higher frequency mode for negative detunings (lower wavelengths). This is in accordance with the behaviour in the coupled mode picture (Fig.3.16). In particular, for each value of the detuning we observe that only one of the modes is bright while the other is strongly suppressed. Two main observations support this conclusion: on the one hand we observe a strong spring shift for only one of the two modes, on the other hand, we observe an asymmetric broadening of the linewidth for the same mode [81]. To address how the optically induced coupling modifies the response of the system we look at the single photon-phonon coupling efficiencies for the two modes as a function of laser wavelength (Fig.3.18). In order to evaluate the g_0 ratio we use equation 3.20 and the data of Fig.3.17b

$$\frac{g_{0,i}}{g_{0,j}} = \sqrt{\frac{BP_i\Omega_i}{BP_j\Omega_j}}, \tag{3.22}$$

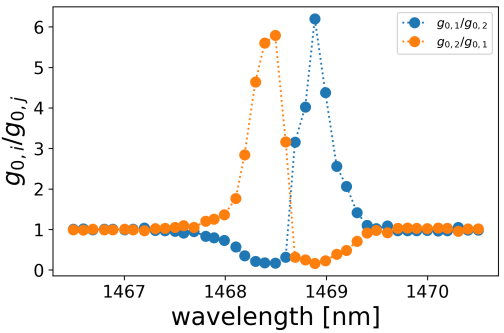

Figure 3.18: Ratio between single photon-phonon coupling efficiencies versus laser wavelength.

where $i \neq j = 1,2$ are indexes that indicate the two mechanical modes. For the band power BP_i we take the area underneath the mechanical peak of mode i at a specific laser wavelength, while for the frequency Ω_i we take the frequency corresponding to the maximum value for the P_{ESA}. From Fig.3.18 we observe that the coupling of the two mechanical modes to the light field becomes strongly asymmetric as the light mediated coupling forces one of the coupled modes to become optomechanically dark. In order to compare this scenario to the results for the design presented previously in this chapter we evaluate the figures of merit (section 3.2.3). The ratio $g_{0,2}/g_{0,1}$ is less than or equal to 6. For continuous measurements this corresponds to having a noise contribution from mode 1 of $S_{\omega\omega}^{\mathrm{th},1}/S_{\omega\omega}^{\mathrm{zpf},2}/\Gamma_1\Gamma_2 \geq 3\times10^{20}$ Hz^{-2} which is better by a factor of $\sim 10^4$ with respect to the off resonance $\Delta \neq 0$ or low power cases. Here we disregard enhancement of the apparent mode linewidths, as this effect would be absent at low temperatures [82]. For pulsed measurements the noise contribution is $\langle \Delta\omega_{T_2}^2 \rangle / g_{0,2}^2 \geq 3.8\times10^3$ which is a factor of ~ 2.5 better than for off-resonance and low power configurations. We remark that the results presented in this section correspond to a device for which the disorder induced by the fabrication is exceptionally low. In this circumstance, there is a clear benefit for pulsing experiments since the figure of merit goes to *zero* for degenerate modes. We conclude that by using a second laser that serves as a coupling laser, the noise contribution for pulsed measurements can be in principle brought to a value that is lower than for the notched structures. We do note that for quantum-limited operation, the influence of that coupling laser in terms of radiation pressure shot noise fluctuations and heating through absorption should be considered carefully.

3.7. CONCLUSIONS

We reported a mechanical design strategy that produces mechanical mode symmetries robust against imperfections. Our method is inspired by perturbation theory, which suggests that mechanical spectral control can be used to minimize the symmetry breaking that is due to fabrication disorder. The goal of this strategy is to minimize the detrimental effects due to the presence of a spurious mode

in optomechanical measurements. We defined figures of merit for continuous and pulsed measurements schemes, that take into account both the values of the optomechanical coupling strength g_0 of the different modes and their frequencies. We implemented the reported strategy in practical realizations of sliced nanobeam cavities, through mechanical notched design and through coupling via radiation pressure. Evaluating the figures of merit, we conclude that the strategy is expected to greatly mitigate spurious mode noise in continuous measurement, while in pulsed measurement a more modest enhancement is expected corresponding to a factor between 1 and 10.

4

BACKACTION EVADING MEASUREMENTS OF MECHANICAL MOTION

This chapter presents pulsed measurements of the displacement of a cryogenic nanomechanical resonator with a sensitivity that approaches the quantum regime. We demonstrate state preparation, tomography, and tracking of a state's thermal decoherence. We discuss the experimental considerations that limit the measurement imprecision and conditional state purity.[1]

[1] Part of this chapter was published in Phys. Rev. Lett. 123, 113601 (2019).

4.1. BACKACTION EVADING MEASUREMENTS

In section 1.1 we introduced the concept of the *standard quantum limit* (SQL), for continuous displacement measurements of a mechanical resonator. We have seen how the backaction introduced by the measurement itself sets a limit to the precision with which one can acquire knowledge on the position of a mechanical resonator. In an optomechanical measurement, this quantum backaction comes about through the probing laser's shot noise exerting a stochastic radiation pressure force on the resonator. The minimum noise added by a measurement, including both imprecision and backaction, is fundamentally limited to x_{zpf} [3, 18, 19, 25, 83]. While the SQL limits the precision of continuous measurements of displacement, Braginsky and coworkers proposed certain classes of *back action evading* (BAE) measurements that can overcome this quantum limit and have a total measurement uncertainty that is smaller than the mechanical ground state size, by probing a particular variable while imprinting all backaction noise on its conjugate variable [28, 29]. Backaction evading measurements have been shown in a number of quantum systems, including besides mechanical systems also optical fields and spin ensembles [21, 23, 35, 36, 42, 78]. In optomechanical systems they avoid back-action by probing only one of the motional quadratures (introduced in section 2.2), while acquiring no knowledge of the orthogonal quadrature. We distinguished two main classes of optomechanical systems, that operate either in the resolved sideband regime or the unresolved, so-called 'bad cavity' limit (section 1.3). The protocols that allow BAE measurements differ for these two parameter regimes. With resolved-sideband cavities ($\kappa \ll \Omega_m$), two-tone driving measurements have been demonstrated [39–41]. In these measurements, the optomechanical interaction is modulated in time with a frequency of twice the mechanical frequency, such that effectively both the upper and lower cavity sideband are pumped by a laser drive. One has to keep in mind that within an optical decay time, $2\pi/\kappa$, many mechanical oscillations occur. Modulating the intensity of the light field inside the optical cavity synchronizes the optomechanical interaction with the evolution of a specific quadrature. In the opposite scenario of the bad cavity limit ($\kappa \gg \Omega_m$), the optical mode decays much faster than the mechanical oscillation period. For this reason it is possible to perform optomechanical measurements that are like snapshots, the light leaking very quickly. Such snapshot, pulsed measurements can also evade backaction, as originally envisioned by Braginsky in 1978 [43] and described in detail by Vanner and co-workers [44]. A pulsed measurement probes only the instantaneous position of a resonator, acquiring no knowledge of its momentum. In *pulsed optomechanics* one employs fast light pulses whose timing thus determines a specific quadrature that is being selectively observed. In this thesis we present a protocol for the realization of pulsed measurements, performed on the sliced nanobeam photonic crystal cavities described in section 1.3.

4.1.1. PULSED BACKACTION EVASION

In optomechanical measurements the Heisenberg limit is enforced by the shot noise fluctuations of the optical field that performs the measurement, creating random displacement fluctuations. While it is fundamentally impossible to

eliminate all measurement backaction, in backaction evading measurements one chooses to probe a degree of freedom on which the backaction simply does not act. One way to understand practical realizations of BAE measurements is to consider the measurement process in the time domain, and realize backaction evasion by choosing wisely when to 'glance' at the mechanical resonator and when not. Because of the regular exchange between kinetic and potential energy in a harmonic degree of freedom, the commutation relation of position and momentum can also be seen as one between positions at different times. The evolution of position and momentum variables x and p can be written as

$$x(t) = X\cos\omega_m t + Y\sin\omega_m t \tag{4.1}$$

$$\frac{p(t)}{m\omega_m} = Y\cos\omega_m t - X\sin\omega_m t, \tag{4.2}$$

where ω_m is the mechanical oscillation frequency, m the motional mass, and X and Y are the position and momentum quadratures (we drop the subscript 'm' used in section 2.5). While the mechanical oscillation is oscillating with period $2\pi/\omega_m$, the quadratures vary slowly. If one measures position at time $t = 0$ one is only measuring the quadrature X. The backaction on this measurement, i.e. the impulse given by radiation pressure that is stochastic because of shot noise on the laser pulse, affects the momentum variable p, such that the position is affected only at a later time t' such that $\omega_m t' = \pi/2$. At the time $t = 0$, instead, the backaction is thus imparted in the Y quadrature that one is not measuring. This ensures the Heisenberg uncertainty relation for $\Delta x\Delta p$, enforced by the fluctuations in the intensity of the measuring optical field that result in a shifted and broadened probability distribution for the quadrature Y. For the case of fluctuations induced by shot noise, the fluctuating force produced in the optical field shifts the probability density of the quadrature Y by an amount that scales with the optical power P_{in} and broadens the distribution of an amount proportional to $\sqrt{P_{\text{in}}}$. In an ideal measurement one can have unlimited sensitivity on the measurement of one of the quadratures while causing all the uncertainty to end up in the un-measured quadrature.

4.1.2. CONDITIONAL STATES AND MEASUREMENT-INDUCED SQUEEZING

In the context of both classical and quantum theory, a physical system is described by using the concept of the system *state*. The state of a system describes an observer's ability to predict the outcomes of future measurements on the system [84], for example quantified through a probability distribution. It thus represents an incomplete knowledge of the system, and is defined with respect to a specific external observer: in principle, it is possible that another observer ascribes a different state to the same system, because she/he has gained more or less information through measurements conducted in the past. To *measure* means to acquire further knowledge, hence change a given system initial state. In quantum measurement theory one talks about projective measurements, meaning that the act of measuring brings the state of a system from an undefined superposition of

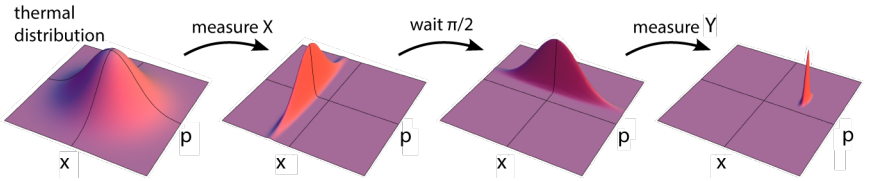

Figure 4.1: From left to right the figure shows three dimensional representations of a mechanical state in the position-momentum phase space [44]. The left most plot is a Gaussian thermal state. After the first pulsed measurement of position x is performed, measuring the quadrature X, the system is prepared in a squeezed state (second plot). The system is left to evolve for a time corresponding to a quarter of the oscillation period $\theta = \pi/2$ (third plot), before a second measurement on x is performed, measuring the quadrature Y. The end result (fourth plot) is a state with a lower occupancy than the initial thermal state; the system has been *cooled* by the measurement. [44]

possible configurations to a specific one[2]. The state of a system is thus changed through a measurement. One can call the a-posteriori state after the measurement a *conditional* state; conditioned by the measurement result. The concept of conditional state is general and applies to classical as well as quantum states [84].

The scenario we focus on here is the one in which a mechanical resonator is initially found in a classical thermal state defined by the environmental temperature T, to which the system thermalizes at equilibrium (Fig.4.1). In a thermal state, the position x of the resonator is represented by a Gaussian distribution that has a width of $\sigma_{\text{th}} = \sqrt{2n_{\text{th}}}x_{\text{zpf}}$, and the momentum by a Gaussian distribution of width $\sigma_{\text{th}} = m\omega_m\sqrt{2n_{\text{th}}}x_{\text{zpf}}$. Imagine now that one performs a measurement on this state: depending on how much knowledge one can obtain, or in other words how strong this measurement is (see section 4.1.3), the result will be a new state with a distribution that depends on the measurement outcome. The new state is *prepared* by the measurement.

To understand the principles of state preparation, consider a measurement at $t = 0$, measuring X, Fig.4.1. With just this measurement, and no extra knowledge over the orthogonal quadrature, the best possible prediction for the oscillator's position at later times is $\cos(\theta)X$ where $\theta = \omega_m t$, differing from the actual position by $x(\theta) - \cos(\theta)X = \sin(\theta)Y$ (with variance $\sin^2(\theta)(Y) = 2n_{\text{th}}x_{\text{zpf}}^2\sin^2(\theta)$ for a thermal state). This notably goes to zero at $\theta = \{\pi, 2\pi\}$, demonstrating that the knowledge of one quadrature allows ideally predicting the mechanical position exactly every half-period. In a phase-space defined by the two quadrature amplitudes this is a *squeezed* state.

Combining two ideal measurements (a quarter period apart) then allows to measure both quadratures. In the hypothetical case without any quantum noise, this would fully predict the oscillator's evolution. In other words, we have then prepared a *pure* state with no classical uncertainty in x. This pure state will then

[2]The resulting configuration of a system will be in general a subsection of possible outcomes, hence leaving still some uncertainty in the system state (*weak* measurements). A special case of projection is a strong measurement, where the measurement projects into a (quantum) pure eigenstate of the measured observable. The amount of information extracted by the measurement, determined by the *measurement strength*, distinguishes between these different outcomes.

decay towards the thermal equilibrium distribution with the time constant $2\pi/\Gamma$, which is the coherence time of the oscillation.

4.1.3. MEASUREMENT STRENGTH

In the above idealized case, the pulsed measurements are assumed to be infinitely accurate and backaction-free. In practice, finite measurement imprecision leads to a Gaussian probability distribution for the measured quadrature amplitude, and backaction increases the width of the orthogonal quadrature probability distribution. We want now to quantify the ability of a measurement to extract knowledge, hence to perform state preparation. In order to arrive at an expression for such a quantity we have to consider the measurement scheme we employ. In section 2.2 we have shown the formal derivation of the optomechanical signal we obtain by performing homodyne detection. The expression is

$$H = |s_{\mathrm{LO}}| \frac{4\sqrt{\kappa_{\mathrm{in}}\kappa_{\mathrm{out}}}}{\kappa} \frac{|s_{\mathrm{in}}|}{1+\left(\frac{2\Delta}{\kappa}\right)^2} \left(\cos\phi + \frac{2\Delta}{\kappa}\sin\phi\right), \tag{4.3}$$

where s_{LO} and s_{in} are the amplitudes of the field in the local oscillator arm and in the signal arm before the interaction with the cavity, κ_{in} and κ_{out} are the in-coupling and out-coupling rates to the collection channel and κ is the total loss rate of the optical cavity, $\Delta = \Delta(t) = g_0 x(t)/x_{\mathrm{zpf}}$ is the time dependent laser detuning with respect to the cavity mode and ϕ is the homodyne angle.

When $\phi = \pi/2$, meaning at the phase-sensitive operation point of the homodyne interferometer, the expression becomes

$$H = 4|s_{\mathrm{in}}||s_{\mathrm{LO}}|\eta \frac{\beta x_n}{\beta^2 x_n^2 + 1}, \tag{4.4}$$

where $\beta = g_0/\kappa$ and $x_n = x/x_{\mathrm{zpf}}$, and $\eta = \sqrt{\kappa_{\mathrm{in}}\kappa_{\mathrm{out}}}/\kappa$ is the total coupling efficiency. Note how the signal is a product of three parts: the amplitude of the local oscillator, the amplitude of the signal beam after interaction with the cavity, and the homodyne-angle-sensitive part. At $\phi = 0$ the signal is proportional to only the amplitudes of the two fields, whereas at $\phi = \pi/2$ it becomes linearly proportional to the detuning of the cavity, meaning in our case the mechanical displacement.

Assuming the linear transduction regime (see section 2.4) in which $4\Delta^2 \ll \kappa^2$ and $\phi = \pi/2$, we have

$$H \simeq 4\,|s_{\mathrm{LO}}|\,|s_{\mathrm{in}}|\,\eta\beta x_n, \tag{4.5}$$

which we can integrate over a duration τ_P, corresponding to the duration of a light pulse:

$$\int_0^{\tau_P} H dt \approx \langle H\rangle \tau_P = 4\langle|s_{\mathrm{LO}}|\rangle\sqrt{\tau_P}\langle|s_{\mathrm{in}}|\rangle\sqrt{\tau_P}\eta\beta x_n = 4\sqrt{N_{LO}}\sqrt{N_P}\eta\beta x_n = \sqrt{N_{LO}}\chi x_n, \tag{4.6}$$

where N_{LO} and N_P are the number of photons in the local oscillator and in the pulse interacting with the cavity. We used the definition [44][46]

$$\chi = 8\eta\sqrt{N_P}g_0/\kappa \tag{4.7}$$

for the quantity χ that we call *measurement strength*. Equation 4.6 gives an intuitive feeling for the parameter χ, which is simply the transduction parameter between normalized displacement and the homodyne output, with both quantities normalized to their respective vacuum state sizes. In addition, the output is amplified by the strength of the local oscillator as expected.

The parameter χ characterizes the pulsed measurement strength and hence the conditional state variance. Performing a measurement transforms one quadrature of an arbitrary initial state into a Gaussian with width $\sigma_m = x_{\mathrm{zpf}}/\chi$ and mean given by the random measurement result. Physical insight into χ is provided by noting that a displacement of size x_{zpf} could be resolved with unity signal-to-noise ratio when comparing two measurements of strength $\chi = 1$. In other words, to achieve a measurement imprecision below the SQL it is necessary to reach $\chi > 1$.

4.2. EXPERIMENTAL REALIZATION

In a practical realization of pulsed optomechanics, one wants to measure for a short time, significantly smaller than a mechanical period, while still having enough sensitivity. To reach quantum-level accuracy with a single pulsed measurement one needs to fulfill the challenging requirement $8\eta\sqrt{N_P}g_0/\kappa \gtrsim 1$, where g_0 is the cavity frequency shift for a displacement x_{zpf} (the vacuum optomechanical coupling rate), η the coupling efficiency of light to the cavity, and N_P the number of photons in the pulse (see previous section 4.1.3). At the same time the cavity linewidth κ should far exceed the mechanical angular frequency Ω_m to accommodate pulse durations much shorter than the mechanical period. In this work, we address these challenges using a cavity optomechanical system based on a sliced photonic crystal nanobeam, allowing large optomechanical coupling rates (Fig.4.2). In the

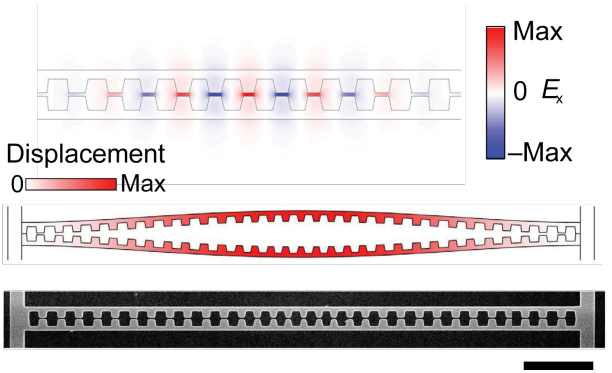

Figure 4.2: Sliced nanobeam photonic crystal cavity employed in the measurements of sections 4.2 and 4.3. The top panel shows a simulation of the optical TE mode hosted by the defect-induced optical cavity in the photonic crystal. The color bar shows the amplitude of the x-component of the electric field E_x. The second plot from the top is a simulation of the first order flexural mechanical mode, described in terms of displacement form the equilibrium position. The third plot from the top shows an SEM picture of such a cavity (scale bar $2\mu m$).

following, we explore how pulsed optomechanical measurements can be brought

close to the quantum regime, and show how these achieve a shot-noise limited single-pulse measurement imprecision of $9x_{\mathrm{zpf}}$, constrained by optical detection efficiency. We discuss the preparation of both thermally squeezed and purified (cooled) conditional mechanical states, and perform state tomography on these.

4.2.1. EXPERIMENTAL METHODS

Figure 4.2 shows a diagram of the sliced silicon nanobeam. The device hosts a photonic crystal nanocavity mode whose resonance frequency (204 THz) depends very sensitively on the flexural movement of the two beam halves. These move roughly independently of each other with two mechanical mode frequencies around $\omega_m/(2\pi) \approx 3$ MHz, separated by ~120 kHz. The photon-phonon coupling rate $g_0/(2\pi) \approx 25$ MHz is approximately equal for both modes. The optical cavity linewidth $\kappa/(2\pi) \approx 20.4$ GHz enables practically instantaneous measurements of mechanical position while still achieving $g_0/\kappa > 10^{-3}$. All reported measurements are performed on the same sample at a temperature of 3.2 K. The exact mechanical frequencies and damping rates drift with time for reasons not fully understood, and are mentioned in the captions for each dataset.

The sample is incorporated in a homodyne interferometer (section 2.1). A Jenoptic electro-optic amplitude modulator AM1470 driven by a waveform generator produces optical pulses using light from a continuous-wave New Focus Velocity 6700 (1430 – 1510 nm bandwidth) tunable narrowband diode laser, which are sent into both interferometer arms. Light is focused on the sample, that is embedded in a a closed cycle Montana C2 cryostat, through an NA ≈ 0.55 lens, coupling to the nanocavity with efficiency $\eta = \sqrt{\eta_{\mathrm{in}}\eta_{\mathrm{out}}} \approx 0.01$, which we estimate from the magnitude of the optical spring effect (see section 1.2.2), as described in detail in [82]. Here $\eta_{\mathrm{in,out}}$ are the efficiencies with which light is coupled from the incident laser beam to the cavity and from the cavity to the detectors, respectively. Each incident pulse carries $\sim 2 \times 10^6$ photons in a duration of $\tau_P = 20$ ns, such that the estimated maximum number of simultaneous intracavity photons is ~ 60. The same lens collects emitted cavity radiation, whose phase quadrature is measured by recording the output of a Newport balanced homodyne detector (9001700 nm wavelength range) after interference with the local oscillator pulse. The resultant detector voltage thus reflects optical phase and mechanical displacement x. This signal is then digitized by a Spectrum M4i.4450-x8 digitizer board with a sampling rate of 500 MS/s

Figure 4.3 shows examples of recorded pulse traces. It can be directly recognized that the recorded pulse heights are correlated when they are separated by a full oscillation period (two last pulses) whereas the pulses separated by half a period (e.g., the third and fourth pulse) are anti-correlated (around a non-zero offset voltage).

All pulse trains we apply are separated from each other by a time that is large compared to the mechanical damping time in order to 'reset' the mechanical state (~ 30 ms). For reasons not fully understood (but most likely deriving from the fact that our homodyne phase is not actively locked during measurements and/or technical laser noise) our measured voltages have an offset that is constant inside

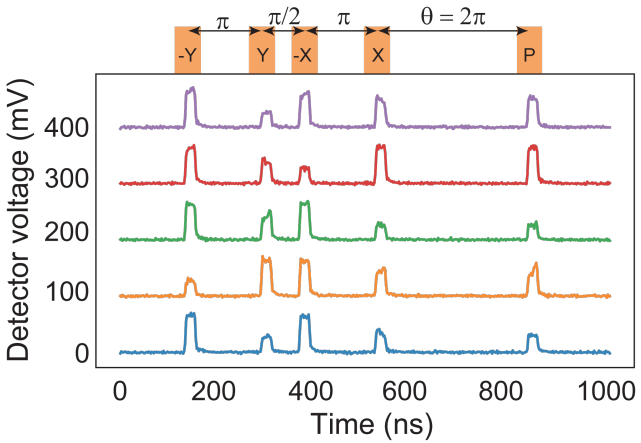

Figure 4.3: Example of measured traces. The first four pulses in each train are used for conditioning and the last pulse is used for read-out. A schematic of the pulsing sequence is drawn on top (where separations in $\omega_m t$ are indicated). The traces are offset for clarity.

a pulse train but varies between different pulse trains. In order to cancel out this offset we always take two pulses per quadrature for the state preparation.

The pulse train for two pulse conditioning is shown in Fig.4.3. The first four pulses of the sequence measure the instantaneous value of the two quadrature amplitudes X and Y, which vary slowly within pulse trains but are randomized between pulse trains with zero mean and variance $\mathrm{Var}(X) = \mathrm{Var}(Y) = 2n_{\mathrm{th}}x_{\mathrm{zpf}}^2$, where $n_{\mathrm{th}} = k_B T/(\hbar\omega_m)$ is the number of thermal phonons. We measure both $-X$ and X to cancel measurement offsets caused by low-frequency drifts. In addition to the first four pulses needed for state preparation, the pulse trains show a fifth pulse that we use for read-out. The fifth pulse is used indeed to perform *state tomography* as we will show in section 4.2.3.

Assuming the signal is given by $s(\omega t) = X\cos(\omega t) + Y\sin(\omega t) + V_{\mathrm{off}} + \delta$, where V_{off} is the offset and δ random noise, and setting $t = 0$ at the final pulse before the tomography pulse, the four preparation pulses read

$$P_0 = s(-5\pi/2) = -Y + V_{\mathrm{off}} + \delta_0 \quad (4.8)$$

$$P_1 = s(-3\pi/2) = Y + V_{\mathrm{off}} + \delta_1 \quad (4.9)$$

$$P_2 = s(-\pi) = -X + V_{\mathrm{off}} + \delta_2 \quad (4.10)$$

$$P_3 = s(0) = X + V_{\mathrm{off}} + \delta_3. \quad (4.11)$$

Hence, to extract the quadrature amplitudes we use $Y = (P_1 - P_0)/2$ and $X = (P_3 - P_2)/2$. Then the full two pulse conditional state reads

$$s_{\mathrm{cond}}(\omega t) = s(\omega t) - \frac{P_3 - P_2}{2}\cos(\omega t) - \frac{P_1 - P_0}{2}\sin(\omega t) - \frac{P_0 + P_1 + P_2 + P_3}{4}, \quad (4.12)$$

where the last term is used to cancel the offset in the final tomography pulse $s(\omega t)$. Note that replacing that term with either $(P_0 + P_1)/2$ or $(P_3 + P_2)/2$ cancels out some

of the noise terms in one quadrature at the expense of increasing the noise in the other quadrature.

4.2.2. DATA ANALYSIS: POSTSELECTION

Having shown the pulse sequence, we now look for the evidence of mechanical motion in the detected signal when the laser is set on resonance with the optical cavity. Figure 4.4 depicts histograms of the difference of the recorded pulses (integrating the voltage over the pulse duration), demonstrating the correlation and anti-correlation behaviour already observable by looking at the raw data of Fig.4.3. This directly indicates that the thermal nanobeam motion is imprinted on the detected pulses. To understand the histogram shapes, we need to consider the

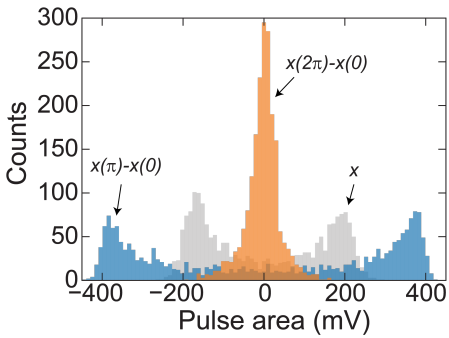

Figure 4.4: Extracted histograms: thermal state [random sampling, mean subtracted] (gray), difference of two pulses a half-period apart (blue), and difference of two pulses a full period apart (orange).

nonlinearity (section 2.4) of the transduction between the mechanical position and optical phase. At the phase-sensitive operation point of the homodyne interferometer and on cavity resonance the balanced detector output is

$$H = 4|s_{\rm in}||s_{\rm LO}|\eta\frac{\beta x_n}{\beta^2 x_n^2+1}, \tag{4.13}$$

with $\beta = 2g_0/\kappa$, $x_n = x/x_{\rm zpf}$ the normalized displacement and $s_{\rm in}$ and $s_{\rm LO}$ the optical field amplitudes towards the sample and in the local oscillator, respectively. This homodyne signal (Fig.4.7a) depends linearly on displacement only when $\beta x_n \ll 1$. Outside this regime, the relationship between signal and displacement is nonlinear and even multivalued. Therefore, our value of $\beta \approx 2.5\times10^{-3}$ causes the thermal Gaussian displacement due to both modes with width (square-root of variance) $\sigma_{\rm th} \approx 290 x_{\rm zpf}$ to be distorted into the double-peaked probability histogram in Fig.4.4. To calibrate the homodyne signal we fit this thermal histogram to an analytical model using the known sample temperature. The fit allows converting the measurement signal to normalized homodyne signal $H_{\rm norm} = H/4|s_{\rm in}||s_{\rm LO}|\eta$.

The homodyne signal as a function of the normalized displacement can be written as

$$H = A\frac{\beta x_n}{\beta^2 x_n^2+1} \equiv A\frac{\Delta}{\Delta^2+1}, \tag{4.14}$$

where we have made explicit the relative change in optical cavity frequency due to the mechanical motion $\Delta = \beta x_n$ and used a constant A to absorb all the normalization terms. Inverting this equation gives

$$\Delta^{\pm} = \frac{1 \pm \sqrt{1-4H'^2}}{2H'}, \tag{4.15}$$

where we have defined $H' \equiv H/A$. As expected,this is multivalued and hence we cannot generally reliably deduce the mechanical position from a single measurement. This is only possible in the linearised regime $\beta^2 x_n^2 \ll 1$, where $H \approx A\beta x_n$. Hence,we only use data where this approximation is valid (post-selection).

We can still, however, reliably predict ensemble histograms and this is used for calibrating the measurement signal. At thermal equilibrium x_n will have a Gaussian probability density with variance $\mathrm{Var}(x_n) = (2k_B T)/(\hbar\omega_m) = 2n_{\mathrm{th}}$, where k_B is the Boltzmann constant, T is temperature, $\hbar$ the reduced Planck constant and ω_m the mechanical oscillation frequency. For multiple independent mechanical modes, we need to sum the variances. The parameter β is approximately equal for both modes. It follows that $\mathrm{Var}(\Delta) = \beta^2\mathrm{Var}(x_n) = 8(g_0/\kappa)^2(n_{\mathrm{th},1} + n_{\mathrm{th},2}) \equiv \sigma_\Delta^2$, where we have marked $n_{\mathrm{th,i}}$ as the mean thermal phonon number for mode i. From probability calculus

$$\mathscr{P}(H') = \mathscr{P}(\Delta(H'))\left|\frac{d\Delta}{dH'}\right| = \frac{1}{\sqrt{2\pi\sigma_\Delta^2}}\exp\left(\frac{\Delta^2}{2\sigma_\Delta^2}\right)\left|\frac{d\Delta}{dH'}\right|, \tag{4.16}$$

where we use $\mathscr{P}$ to mark the probability density. In order to deal with the multivaluedness we need to sum over both branches

$$\mathscr{P}(H') = \frac{1}{\sqrt{2\pi\sigma_\Delta^2}}\exp\left(\frac{(\Delta^+)^2}{2\sigma_\Delta^2}\right)\left|\frac{d\Delta^+}{dH'}\right| + \frac{1}{\sqrt{2\pi\sigma_\Delta^2}}\exp\left(\frac{(\Delta^-)^2}{2\sigma_\Delta^2}\right)\left|\frac{d\Delta^-}{dH'}\right|. \tag{4.17}$$

Inserting Eq. 4.15 and its derivative

$$\left|\frac{d\Delta^{\pm}}{dH'}\right| = -\frac{1}{2H'}\left(1 \mp \frac{1}{\sqrt{1-4H'^2}}\right), \tag{4.18}$$

will give an algebraic form for the expected probability density, that only depends on the parameter σ_Δ^2. Hence, measuring the thermal equilibrium distribution of our pulse outputs and fitting it, allows us to relate the pulse outputs to the parameter H', and further, in the linear regime, to $x_n = H'/\beta$. This fit is plotted together with data in Fig.4.5.

In order to avoid any errors caused by low frequency drifts the thermal histogram points are extracted by taking the difference of two pulses half an oscillation period apart and dividing by two. For one mode, this would give exactly the same histogram as random sampling. Although the fact that we have two modes with differing frequencies produces an error to this procedure, the two frequencies are close enough that the error in σ_Δ^2 is less than 0.5% in all cases considered in this chapter. (The error is the difference between a factor of 8 and factor $(6-2\cos(r\pi))$.)

It should also be emphasized that with the parameters relative to the structure of Fig.4.2 of which the measurements until section 4.3 are shown, the expected distribution will always be doubly peaked around $H' = \pm 0.5$. Any small uncertainty in parameter σ_Δ^2 will not change the position of the peaks. Hence, our calibration is relatively insensitive to any imprecision in σ_Δ^2. On the other hand, the vertical scale here is fixed (with proper normalization) and hence the correctness of the height of the center flat part of the histogram will show the accuracy of our σ_Δ^2 extraction. As can be seen in Fig.4.5 (and this was true generally) the line does lie somewhat above the measured histogram (this error would correspond to ~ 10% higher σ_Δ^2). We note that if this error would be in the β parameter, this would make the extracted imprecisions lower (meaning, better) by ~ 5%. Finally, we note that

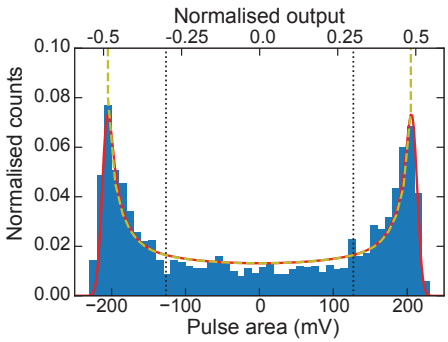

Figure 4.5: Example of a thermal probability histogram of measurement outputs and fit to equation 4.17 (dashed line). From this we can relate the measured voltages (bottom x-axis) to the normalized output (H', top x-axis). Solid line shows a numerical convolution of the analytical solution (that diverges at $H' = \pm 0.5$) and a Gaussian with the width given by our noisefloor. The thermal histogram points are extracted by taking the difference of two pulses half an oscillation period apart and dividing by two. This eliminates errors from a constant offset drift (see previous section). Time between individual measurements is roughly three times the mechanical damping time. Dotted lines show our post-selection thresholds at $H' = \pm 0.31$.

we obviously cannot use this method for the off-resonance data we extract the noise floor and single-pulse imprecision from. For that data we first gathered data on-resonance to run the above analysis and then without changing anything except laser frequency run the off-resonance measurement and used the on-resonance data for calibration.

By running the same pulse sequence (equation 4.12) and analysis for measurement data gathered with the laser tuned off-resonance with the optical cavity we extract the noise floor. The resulting conditional state histogram with $\theta = 2\pi$, shown in Fig.4.6, has the width $11.67 x_{\mathrm{zpf}}$, when converted to displacement.

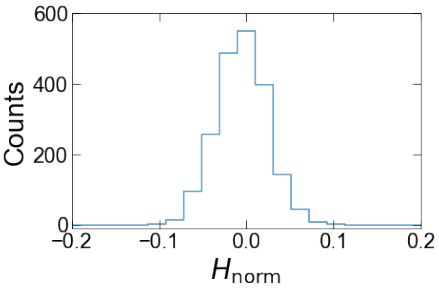

Figure 4.6: Reference measurement away from optical resonance, from which the measurement noise floor is extracted.

As the off-resonance data will presumably have no signal (X, Y=0) we can write

$$s_{\mathrm{cond}}^{\mathrm{noise}}(2\pi) = s(2\pi) - \frac{P_3 - P_2}{2}\cos(2\pi) - \frac{P_0 + P_1 + P_2 + P_3}{4} \tag{4.19}$$

$$= V_{\mathrm{off}} + \delta_4 - \frac{V_{\mathrm{off}} + \delta_3 - V_{\mathrm{off}} - \delta_2}{2} - \frac{4V_{\mathrm{off}} + \delta_0 + \delta_1 + \delta_2 + \delta_3}{4} \tag{4.20}$$

$$= \delta_4 - \frac{\delta_0 + \delta_1}{4} - \frac{3\delta_3}{4} + \frac{\delta_2}{4}. \tag{4.21}$$

Hence, we have for the variance (we assume all noise terms are independent and hence have no mutual covariance)

$$\mathrm{Var}\left[s_{\mathrm{cond}}^{\mathrm{noise}}(2\pi)\right] = \mathrm{Var}(\delta_4) + \frac{\mathrm{Var}(\delta_0) + \mathrm{Var}(\delta_1) + \mathrm{Var}(\delta_2) + 9\mathrm{Var}(\delta_3)}{16} \tag{4.22}$$

$$= (1 + \frac{3}{4})\mathrm{Var}(\delta_{\mathrm{sn}}), \tag{4.23}$$

where for the last line we have assumed that the variance of noise in each pulse is the same and marked it $\mathrm{Var}(\delta_{\mathrm{sn}})$. The noise floor variance is the sum of the imprecision in the measurement of X [$\mathrm{Var}(\delta_{\mathrm{sn}})/2$ as two pulses are used], the imprecision in the tomography pulse [$\mathrm{Var}(\delta_{\mathrm{sn}})$] and the added variance due to the offset correction [$\mathrm{Var}(\delta_{\mathrm{sn}})/4$]. Hence, in order to extract the single-pulse imprecision $\sqrt{\mathrm{Var}(\delta_{\mathrm{sn}})}$ we need to divide the variance we extract by 7/4, meaning we need to divide the width we extracted $11.67x_{\mathrm{zpf}}$ with square root of 7/4, giving $8.8x_{\mathrm{zpf}}$.

We can make an easy check on this, as we can also extract the variance of the "non-conditional state" from the off-resonance data as

$$s_{\mathrm{non-cond}}^{\mathrm{noise}}(2\pi) = s(\omega t) - \frac{P_0 + P_1 + P_2 + P_3}{4} \tag{4.24}$$

$$= \delta_4 - \frac{\delta_0 + \delta_1 + \delta_2 + \delta_3}{4}, \tag{4.25}$$

from which using similar arguments as before we can extract $\mathrm{Var}\left[s_{\mathrm{non-cond}}^{\mathrm{noise}}(2\pi)\right] = (1+1/4)\mathrm{Var}(\delta_{\mathrm{sn}})$. From the data (not shown) we can extract a non-conditional width of $9.92x_{\mathrm{zpf}}$ which would again give a single pulse shot-noise of $8.8x_{\mathrm{zpf}}$. Note that the

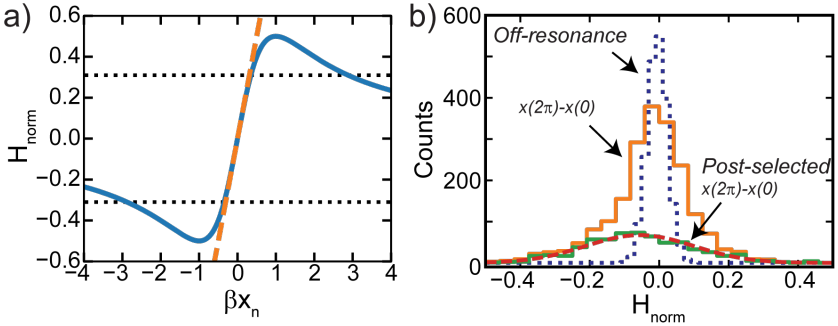

Figure 4.7: a) Full transduction function (equation 4.13, solid line), linear approximation (dashed line), and postselection threshold (dotted lines). b) The histogram of the difference of two pulses a full period apart (as in Fig.4.4), before and after postselection (solid lines). After postselection we recover a Gaussian shape (the dashed line shows the fit). The dotted line is a reference measurement away from optical resonance, from which the measurement noise floor is extracted (Fig.4.6).

actual imprecision in the measurement of X (without the tomography pulse) is half the single-pulse imprecision, due to the fact that we use two pulses to measure it.

To maximize sensitivity and allow single-valued estimation, we post-select the data so that the measured value for the quadrature amplitude of interest falls in the linear transduction regime. The dotted lines in Fig.4.7a show the chosen post-selection thresholds. Figure 4.7b shows the effect of post-selection on the histogram of the difference of two pulses separated by $\theta = 2\pi$. The original histogram had non-Gaussian shape with variance dominated by shot-noise due to a large contribution from parts of the transduction function with reduced sensitivity at $|\beta x_n| \approx 1$. The post-selected histogram has a Gaussian shape with larger variance. Hence, the post-selection protocol allowed recovering the linear operating regime.

4.2.3. STATE TOMOGRAPHY

In section 4.2.1 we have introduced the experimental protocol. In addition to the state preparation pulses (Fig.4.3), the last pulse allows quantifying the difference between the expected and actual mechanical position, and thus characterize the state prepared by the first measurements. By varying the waiting time between state preparation and tomography, we can map this difference in all quadrature angles and perform full *tomography* of the conditional state [64]. In Fig.4.8, we report the histograms as a function of the angle $\theta = \omega_m t$. The top-left image shows the data before the postselection. To show the effect of the postselection (full data shown in Fig.4.8, top-right plot), we show in Fig.4.9 the original data together with the postselected data for some of the tomography angles. The non-Gaussian distribution shape, as in Fig.4.4, is related to the nonlinearity, as explained in section 4.2.2. The top plots in Fig.4.8 show distributions of the tomography pulse P. The bottom plots show the histograms conditioned on the second pulse pair that measures X (left, corresponding to $P - \cos(\theta) X$) and on all four preparation pulses (right, corresponding to $P - \cos(\theta) X - \sin(\theta) Y$).

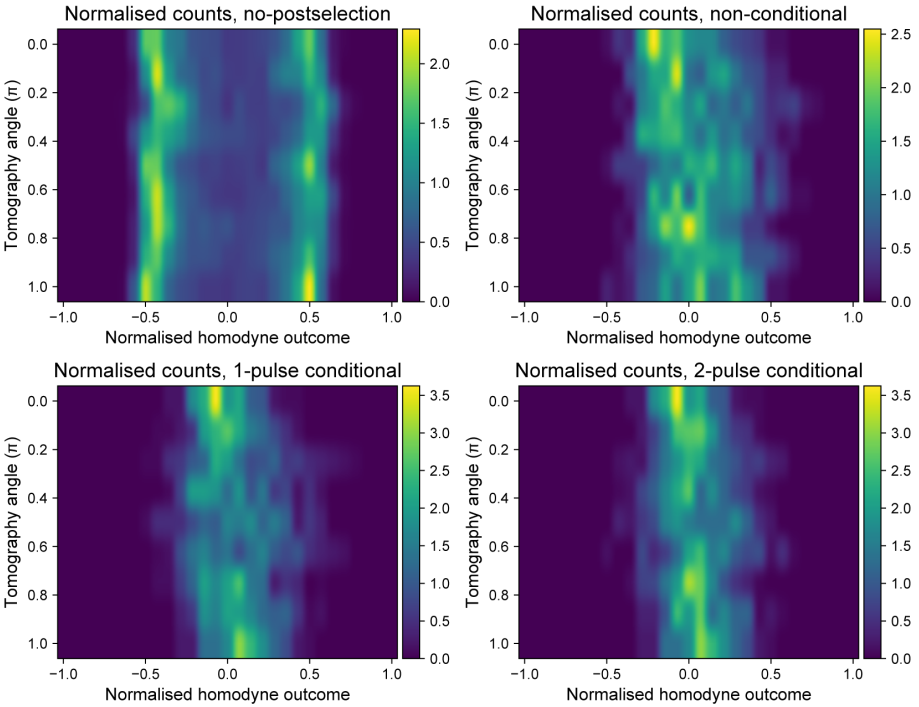

Figure 4.8: We reconstruct the images from the measured histograms at different tomography angles $\theta = \omega_m t$ using Python package scikit-image [85] (version 0.15), with the function *iradonsart* and relaxation parameter of 0.0001.

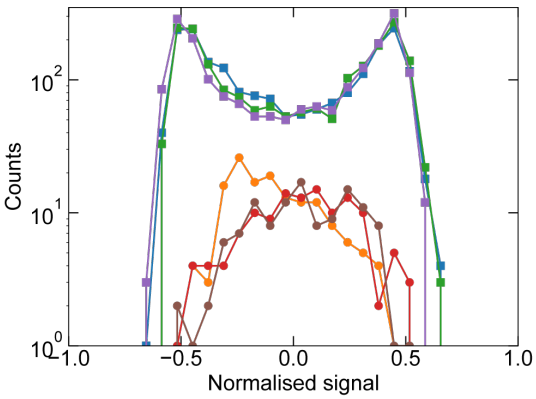

Figure 4.9: Original histogram data at tomography angles π,$3\pi/2$ and 2π, before (squares) and after (circles) post-selection.

The histograms of Fig.4.8 constitute the mechanical marginals. Applying an inverse Radon transform to those histograms one can reconstruct the phase-

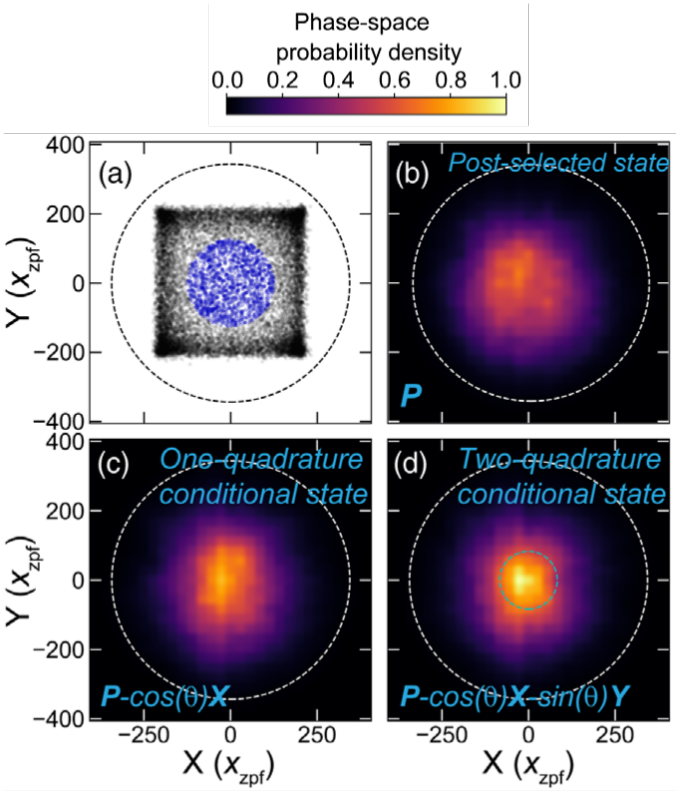

Figure 4.10: (a) Values of X and Y from state preparation pulses, post-selected measurements as blue data points. (b)–(d) Reconstructed phase-space probability densities, for unconditional data (b), one-quadrature conditional data (c) and two-quadrature conditional data (d). A single normalization is applied on panels (b)–(d). White dashed lines show the calculated full-width-halfmaximum (FWHM) of the thermal state at 3.2K, and green dashed line the measured FWHM of the conditional state. Reconstructions use nine different angles θ each combining 2000 acquired traces.

space probability density of the conditional states [44][85]. Figure 4.10 presents experimental results of conditional state preparation and tomography. Figure 4.10a shows X and Y obtained from the state preparation, where only the blue instances are postselected to be considered for tomography. Figure 4.10b shows this Radon transform for only the tomography pulse, depicting a small central part of the thermal Gaussian distribution, determined by the postselection. As we subtract the measured (random) values for the quadrature amplitudes when retrieving the marginals, the subsequent panels depict the conditional state *shifted to the origin* [44, 72]. Figure 4.10c shows the thermally squeezed state prepared with single-quadrature conditioning. Finally, in Fig.4.10d we plot the phase-space probability density for the state conditioned on both quadratures, which would have the ground state area if the measurements would be ideal. In our case the

state has an average width that corresponds to a one-mode thermal state at a temperature of 380 mK, purified from the original temperature of 3.2 K. We again note that to obtain this diagram, the values of X and Y that are different for each particular measurement (pulse train) have been subtracted. That means that for a given instance of measurement, the conditional state is centered on the values of X and Y (as plotted in Fig.4.10a for many instances), with a purity (uncertainty in phase space) as given by Fig.4.10d.

The width of this conditional state is plotted in Fig.4.11 as a function of the tomography angle. In the measured data the minimum width reached is $58x_{\mathrm{zpf}}$, significantly exceeding the shot noise floor, and is maximized at $\theta = 3\pi/2$. We will discuss in the next section how this value arises from the presence of a spurious mode, that limits our ability to predict the outcome of subsequent measurements.

4.3. IMPERFECTION INDUCED SECOND MODE NOISE

The width of the conditional state shown in Fig.4.10d is explained through the existence of a second mechanical mode. As in this device the two mechanical modes couple equally strongly to the cavity, the contribution of the second mechanical mode is captured by

$$x(\theta) = X_1 \cos(\theta) + Y_1 \sin(\theta) + X_2 \cos(r\theta) + Y_2 \sin(r\theta) \tag{4.26}$$

with r the ratio of the mechanical frequencies and subscripts 1,2 referring to the two modes. The resulting uncertainty caused by the second mode as a function of θ is plotted in Fig.4.11, matching the data well. For a derivation of the fitting curve see appendix 4.6. There are no fitting parameters here, as for both modes frequency

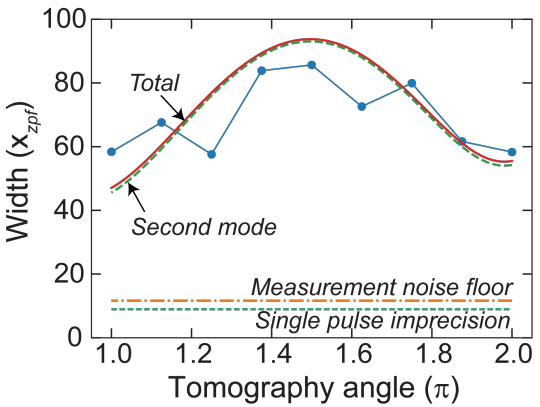

Figure 4.11: Width of mechanical marginals for the two-quadrature conditional data. The dash-dotted line shows the measurement noise floor, the dashed line the expected second mechanical mode contribution, and the solid line their squared sum. The noise floor differs slightly from the single-pulse imprecision (dotted line) as the measurement uses multiple pulses and shot noise of the tomography pulse is not subtracted.

and temperature are known. The non-monotonic shape is caused by measuring

the Y quadrature before the X quadrature, causing it to have a larger variance as it has more time to evolve out of sync with the mode of interest. Assuming $r \simeq 1$ and equal n_{th} and x_{zpf} for both modes, the expected contribution to the conditional state width is approximated as

$$\sqrt{4n_{\mathrm{th}}\left[1-\cos(r\theta)\cos(\theta)-\sin(r\theta)\sin(\theta)\right]}x_{\mathrm{zpf}}. \tag{4.27}$$

This vanishes when $\cos(\theta)\cos(r\theta) = 1$ and $\sin(\theta)\sin(r\theta) = 0$, or vice versa. Although this cannot be fulfilled exactly unless r is a rational number, it is approximated when $\theta = 2n\pi$, where $n \simeq \omega_m/(r\omega_m - \omega_m)$.

We demonstrate how mechanical decoherence and rethermalization can be tracked by recording the state evolution at longer timescales. In Fig.4.12a and 4.12b we compare the one-pulse conditional state width after one mechanical period ($\theta = 2\pi$) and where this condition is fulfilled ($n \sim 54, 56$). A slightly lower conditional state width is measured at $\theta = 54\pi, 56\pi$ than at $\theta = 2\pi$. The state widths at $\theta = 54\pi, 56\pi$ differ strongly from expectation based on the formula above. This is because we neglected thermal decoherence, which will cause the state width to increase in time as $\sqrt{8n_{\mathrm{th}}[1-\exp(-t\Gamma/2)]}x_{\mathrm{zpf}}$ for two mechanical modes, assuming the modes have identical n_{th} and x_{zpf}, and Γ. Figures 4.12c and 4.12d show measurements around the times where the second mode contribution should vanish on a longer timescale, tracking the loss of coherence due to thermalization quantitatively in time domain.

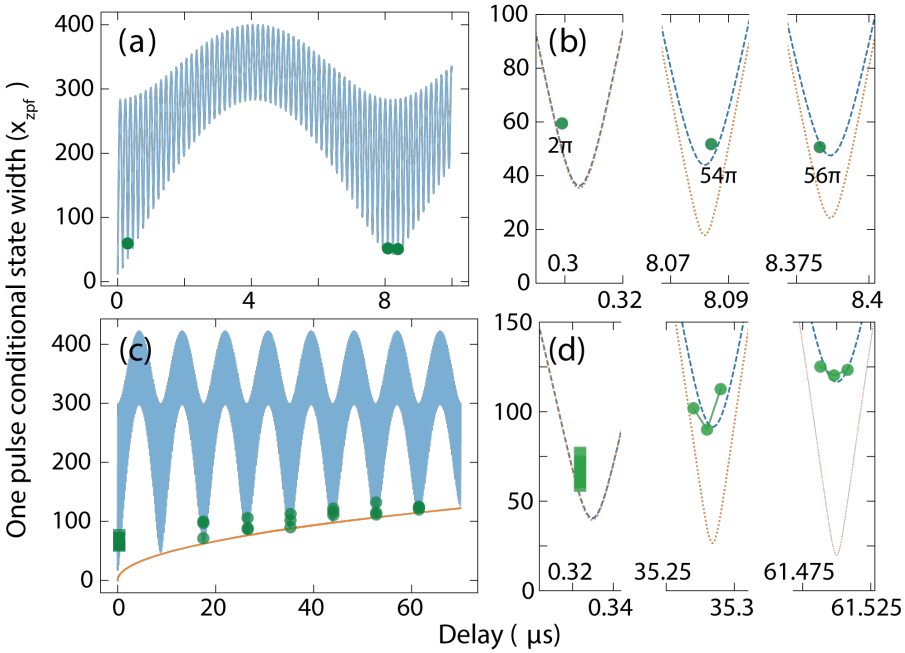

Figure 4.12: (a-b) Common mode measurement, showing that smaller conditional state width is achieved at $\theta = 54\pi, 56\pi$ than at $\theta = 2\pi$ due to minimization of the second mode contribution at these times. Panel (b) shows close-ups of (a). The blue line shows the expected behaviour with fitted $\Gamma/(2\pi) = 400$ Hz, the yellow dashed line [only shown in (b)] without any decoherence. The circles are measured data. Frequencies $\omega = 2\pi \times 3.340$ MHz and $r\omega = 2\pi \times 3.218$ MHz. **(c-d)** Thermal decoherence measurement demonstrating the growing conditional state width. Panel (d) shows close-ups of (c). Yellow line in (c) is the envelope function $\sqrt{[1-\exp(-t\Gamma/2)]8n_{\rm th}}x_{\rm zpf}$, and the blue line the full expected curve, both with fitted $\Gamma/(2\pi) = 400$ Hz, yellow dashed line in (d) without decoherence. Each pulse sequence here has two tomography pulses, one at $\theta = 2\pi$ (shown as squares) and other at variable distance (circles). Also shown is data at ± 10 ns around $\theta = 2n\pi$ points. Frequencies $\omega = 2\pi \times 3.090$ MHz and $r\omega = 2\pi \times 2.976$ MHz. All datasets contained 1000 samples before post-selection.

4.4. PULSED MEASUREMENT WITH ONE MECHANICAL MODE

In section 4.2.3 we presented the conditional state result (Fig.4.10) and quote that the width of the conditional state ammounts to $58x_{\rm zpf}$, limited by the presence of a second mechanical mode. In chapter 3 we present a strategy to purify the mechanical response of systems of the kind of Fig.4.2, with the intent to overcome this limit. The strategy relies on mechanical spectral design that makes the modes robust against imperfections. For the structures of Fig.4.2 the mechanical symmetry of the system is broken by structural imperfections introduced by disorder in the fabrication process and one cannot actually consider that an in-plane flexural mode is governing the motion of the sliced nanobeam, but has to consider instead the two nanobeam slices as independent resonators whose resonance frequencies are almost degenerate. In contrast, in properly designed structures the symmetric

in-plane flexural mode is the only first-order mechanical mode that has a large optomechanical coupling.

The device that we employ for the following measurements is of the kind presented in Fig.3.5, with a notch extension of 3 μm on both sides of the photonic crystal. This device is characterized by a mechanical resonance frequency of 2.528 MHz, see Fig.4.16. To estimate the uncertainty we measure and verify now only a single quadrature, and thus employ a simplified protocol with three optical pulses (Fig.4.13):

$$\begin{aligned} P_0 &= s(0) = -X + V_{\text{off}} + \delta_0 \\ P_1 &= s(\pi) = X + V_{\text{off}} + \delta_1 \\ P_2 &= s(3\pi) = X + V_{\text{off}} + \delta_2. \end{aligned} \tag{4.28}$$

We use the first two pulses to normalize the histograms, by recognizing that the

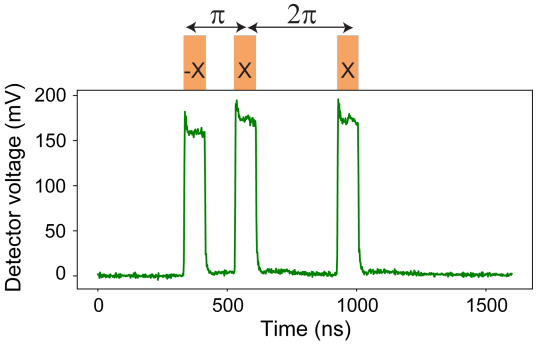

Figure 4.13: Example of a pulses sequence employed for the measurements. The pulses here have a length of 80 ns, longer than the ones of Fig.4.3. The scheme on top shows that the pulses are separated half a mechanical period $\theta = \pi$ and one period $\theta = 2\pi$ respectively.

measured signal

$$s_{\text{th}} = s(\pi) - s(0) = \frac{P_1 - P_0}{2} = X + \frac{\delta_1 - \delta_0}{2}, \tag{4.29}$$

has a variance

$$\sigma_{\text{th}}^2 = \sigma_x^2 + \frac{1}{2}\text{Var}[\delta] \tag{4.30}$$

which is proportional to the variance of the position $\sigma_x^2 = \sigma_{\text{th}}^2 = 2n_{\text{th}}x_{\text{zpf}}$. In equation 4.30 we have used the fact that the noise terms are independent hence $\text{Var}[\delta_0] = \text{Var}[\delta_1] = \text{Var}[\delta_2] = \text{Var}[\delta]$. Moreover, the Gaussian shape of the resulting histograms (Fig.4.14) indicates that the parameters of the system are such that we are in the linear transduction regime for this sample ($\beta x_n \ll 1$), so we do not perform post-selection as in the previous measurements. The thermal histogram has a variance of $\sigma_{\text{th}} \simeq 259 x_{\text{zpf}}$.

In Fig.4.15 we show the histogram corresponding to the conditional state

$$s_{\text{cond}} = s(3\pi) - s(\pi) = \frac{P_2 - P_1}{2}, \tag{4.31}$$

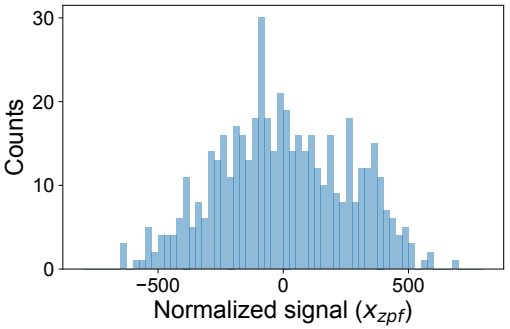

Figure 4.14: Normalized thermal histogram as in equation 4.29. The width of the histogram is $\sigma_{\rm th} \simeq 259 x_{\rm zpf}$, which is used to calibrate the homodyne signal to a normalized displacement as plotted on the horizontal axis here.

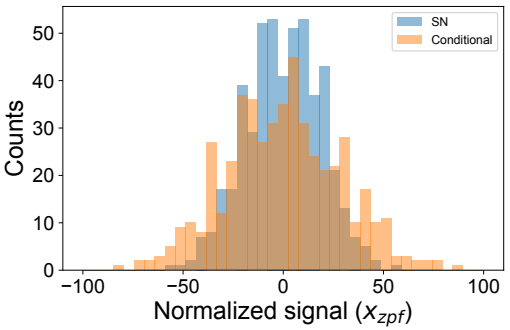

Figure 4.15: Conditional histogram as in equation 4.31 (orange). In blue is the histograms obtained using the same formula but with data taken off-resonance, i.e. with the same power but with the laser blue detuned of about 10 nm.

together with the histogram obtained with data using the same pulses differences as in the equation but with *off-resonant* data. The latter constitutes our noise floor (see section 4.2.1). The conditional state has a width of $\sigma_{\rm cond} \simeq 28.27 x_{\rm zpf}$, notably smaller than in the previous measurements performed on structures with multiple nearly degenerate modes. The variance of the two histograms in Fig.4.15: $\sigma^2_{\rm cond} \equiv \sigma^2_{\rm sn} = 1/2 {\rm Var}[\delta]$ should read the same value if no other noise source related to the mechanical motion were to be present in our measurement. This is what we expect for structures that truly show only one mechanical mode. However, the width of the noise histogram reads $\sigma_{\rm sn} \simeq 18.57 x_{\rm zpf}$, corresponding to a single pulse imprecision of $13.13 x_{\rm zpf}$ (slightly higher than in the measurements reported in Fig.4.6).

In order to address the residual noise contribution we study the presence of other mechanical modes and evaluate their contribution. In Fig.4.16 we report a mechanical spectrum for the structure employed in the measurements of this

section. While there is only one peak near the frequency of interest, showing that the lowest-order common mode is practically uncoupled to the light field, we observe that the structure exhibits another mechanical mode at 8.289 MHz. This should correspond to the mechanical mode of third order, i.e. the mode for which the standing wave formed by each nanobeam slice has three antinodes. By using equation3.15, which quantifies the noise contribution introduced by the presence of another mode in pulsing experiments, we can calculate the expected noise contribution to the conditional state width caused by the presence of this mode to be of $\sigma_{3\text{rdorder}} \simeq 11.71 x_{\text{zpf}}$.

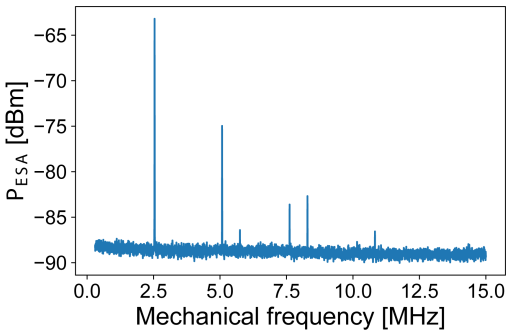

Figure 4.16: Mechanical spectrum acquired operating the homodyne interferometer in continuous measurement regime (see section 2.3.3), with the cavity driven on resonance. It is possible to recognize five peaks: the peak with the highest signal to noise ratio is the in-plane antisymmetric flexural mode with frequency $\omega_m \simeq 2.538$ MHz. By looking at $2\omega_m$ and $3\omega_m$ we find the higher harmonics of that mode (see section 2.4). The peak with the second-highest signal to noise ratio is a higher-order mechanical mode at $\omega_{m,3^{rd}order} \simeq 8.289$ MHz. The final two observed peaks are nonlinear mixing of the two modes.

Since we must sum the variances of each noise contribution we have $\sqrt{\sigma^2_{3^{rd}order} + \sigma^2_{\text{sn}}} = \sqrt{11.71^2 + 18.57^2} x_{\text{zpf}} = 21.95 x_{\text{zpf}}$. We conclude that the third mode alone cannot explain the excess noise in the conditional mode histogram of Fig.4.15. In the following we discuss possible sources of such extra noise (Fig.4.17) we show the extra noise contribution

$$\sigma_{\text{extra}} = \sqrt{\sigma^2_{\text{cond}} - \sigma^2_{\text{sn}} - \sigma^2_{3^{\text{rd}}\text{order}}} \tag{4.32}$$

as a function of pulse duration for two optical powers. The fact that the extra noise does not increase with pulse width indicates that backaction is not its cause, since that would scale with the pulse duration as the number of photons per pulse scales with duration. We observe that σ_{extra} depends inversely on the optical power in the signal beam arm. We can therefore also rule out other mechanical modes as dominant sources, as those would be constant with power. Indeed, we do not observe other relevant peaks at least in a 20 MHz wide spectrum except the two considered modes and their harmonics (Fig.4.16). Finally, we remark that excess laser phase noise, transduced by the cavity is also unlikely source of noise. At low powers we observe $\sigma_{\text{extra}} \simeq 42 x_{\text{zpf}}$. To produce such significant

noise, laser frequency fluctuations would need to shift the optical resonance by $\sim 40g_0$ in a mechanical period, i.e. of the order of a GHz. Since this is much larger than the linewidth of the lasers we employ in the experiment (< 1 MHz), it is unlikely that classical laser phase noise is contributing to the measurement imprecision. Finally, we remark that the fact that the noise, expressed in units of x_{zpf}, decreases with increasing signal power indicates a noise source whose magnitude rises less fastly with probing power than the mechanical signal. An example is electronic noise. However, that can be excluded as it would affect the shot noise measurement as well as the measurements that probe the cavity. As such, the extra noise is still of unknown origin. Further measurements should point out if calibration errors could play a role, and if taking into account the full mechanical fluctuation spectra can lead to further insights. For now, we can conclude that the mechanical design can lead to an improvement of the size of the conditional states. Although in these measurements the shot-noise imprecision was larger than before, we believe this could be improved through cavity design (see the next chapter). Finally, we note that the third-order mechanical mode plays a limiting factor at these temperatures. Mitigation of this mode, through either active or passive cooling, is an important next step towards reaching the quantum regime of pulsed optomechanical measurement.

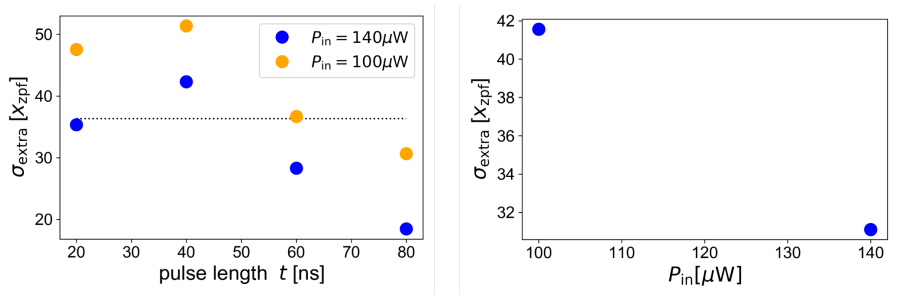

Figure 4.17: Dependence of extra noise contribution, equation 4.32, with pulse duration t (left plot) and signal power P_{in} (right plot).

4.5. CONCLUSIONS

The results presented in this chapter show that nano-optomechanical systems can bring quantum-level mechanical measurements with single nanosecond pulses within reach. We demonstrated a minimum pulse sensitivity of $\sim 9x_{\mathrm{zpf}}$, and state tomography with a conditional state width of $\sim 28x_{\mathrm{zpf}}$, limited mostly by other mechanical modes. Notably, achieving larger light coupling efficiency without changing any other parameters would bring the measurement uncertainty in one quadrature below x_{zpf}, allowing squeezed state preparation and observing quantum backaction [19]. Preparing a pure state of a single resonator would require reducing the second mode contribution. We have explored the performance of devices designed to show a single mechanical mode around the desired frequency. In this

case we can further squeeze the width of the thermal distribution via measurement, which allowed us to improve the squeezing of the thermal distribution after one mechanical period. Further improvements could be reached by additional cooling (cryogenic or feedback). Alternatively, one could exploit the fact that with quantum level precision, a single pulse entangles the quadratures of the two mechanical modes, providing a new path to explore many-mode quantum optomechanics in the time domain. Indeed, our experiments demonstrate how pulsed measurements yield interesting possibilities for measurement and control of mechanical motion, complementing the conventional frequency domain analyses. This "time-domain optomechanics" could allow new protocols for quantum sensing that exploit fast backaction-free determination of a mechanical quadrature, as well as new paradigms to create quantum states of motion and mechanical entanglement [86].

4.6. APPENDIX: CONDITIONAL STATE VARIANCES

To illustrate the basic principle of calculating the conditional state variances, consider first the variance of the difference between two pulses separated by angle $\theta = \omega t$, assuming the motion is given by $x(\theta) = X\cos\theta + Y\sin\theta$

$$\begin{aligned} \mathrm{Var}[x(\theta) - x(0)]_{1\mathrm{mode}} &= \mathrm{Var}\left[X\cos\theta + Y\sin\theta - X\right] \\ &= \mathrm{Var}\left[X(\cos\theta - 1) + Y\sin\theta\right] \\ &= (\cos\theta - 1)^2\,\mathrm{Var}(X) + \sin^2\theta\,\mathrm{Var}(Y) \\ &= (2 - 2\cos\theta)\mathrm{Var}(Q), \end{aligned} \tag{4.33}$$

where we have marked $\mathrm{Var}(Q) = \mathrm{Var}(X) = \mathrm{Var}(Y)$ as the variance of the quadrature amplitudes, which for a thermal state is given by $\mathrm{Var}(Q) = 2n_{\mathrm{th}}x_{\mathrm{zpf}}^2$. Note that for the difference of two uncorrelated pulses we would expect the variance to be $2\mathrm{Var}(Q)$.

Any dephasing process can be added to this formula by requiring that the covariance of the quadrature amplitude with itself goes down with time as $\mathrm{Cov}[X(t), X(0)] = \exp(-\gamma t)\mathrm{Var}[X(0)]$, where $\gamma = \Gamma/2$ for the mechanical damping. Note that this produces the correct limits $\mathrm{Cov}[X(0), X(0)] = \mathrm{Var}[X(0)]$ and $\mathrm{Cov}[X(\infty), X(0)] = 0$. Then using the formula $\mathrm{Var}\left[aX + bX'\right] = a^2\mathrm{Var}[X] + b^2\mathrm{Var}[X'] + 2ab\mathrm{Cov}[X, X']$ we have

$$\begin{aligned} &\mathrm{Var}\left[X'\cos\theta - X + Y\sin\theta\right]_{1\mathrm{mode}} = \\ &= \cos^2\theta\mathrm{Var}(X') + \mathrm{Var}(X) - 2\cos\theta\exp(-\gamma t)\mathrm{Var}(X) + \sin^2\theta\mathrm{Var}(Y) \\ &= \left[2 - 2\exp(-\gamma t)\cos\theta\right]\mathrm{Var}(Q), \end{aligned} \tag{4.34}$$

which produces the expected limits. Note that we assume $\mathrm{Cov}(X, Y) = 0$ at all times. Going through similar algebra for the one and two pulse conditional state will produce

$$\begin{aligned} \mathrm{Var}[x(\theta) - \cos\theta x(0)]_{1\mathrm{mode}} &= \{1 + \cos^2\theta[1 - 2\exp(-\gamma t)]\}\mathrm{Var}(Q) \\ \mathrm{Var}[x(\theta) - \cos\theta x(0) - \sin\theta x(\pi/2)]_{1\mathrm{mode}} &= [2 - 2\exp(-\gamma t)]\mathrm{Var}(Q). \end{aligned} \tag{4.35}$$

Now, we want to derive the same formulae in the case of two mechanical modes, $x(\theta) = X_1\cos\theta + Y_1\sin\theta + X_2\cos r\theta + Y_2\sin r\theta$, where r is the ratio of the

two mechanical frequencies. For generality we can assume they can have different $n_{\rm th}$ and/or $x_{\rm zpf}$, and hence $\mathrm{Var}(Q_i) = \mathrm{Var}(X_i) = \mathrm{Var}(Y_i)$, where $i = 1,2$. Note that although we do not consider the coupling from the modes to the light field explicitly here, ultimately differing coupling constants would affect the results similarly as differing $x_{\rm zpf}$. Going through similar algebra as above will then produce

$$\begin{aligned}
\mathrm{Var}[x(\theta) - x(0)]]_{\rm 2modes} &= [2 - 2\exp(-\gamma_1 t)\cos\theta]\mathrm{Var}(Q_1) \\
&\quad + [2 - 2\exp(-\gamma_2 t)\cos r\theta]\mathrm{Var}(Q_2) \\
\mathrm{Var}[x(\theta) - \cos\theta x(0)]_{\rm 2modes} &= \{1 + \cos^2\theta[1 - 2\exp(-\gamma_1 t)]\}\mathrm{Var}(Q_1) \\
&+ \{1 + \cos^2\theta[1 - 2\frac{\cos r\theta}{\cos\theta}\exp(-\gamma_2 t)]\}\mathrm{Var}(Q_2)
\end{aligned} \tag{4.36}$$

$$\begin{aligned}
\mathrm{Var}[\quad x(\theta) \quad & - \cos\theta x(0) - \sin\theta x(\pi/2)]_{\rm 2modes} = \\
& [(2 - 2\exp(-\gamma_1 t)]\mathrm{Var}(Q_1) \\
& + \{2 - 2\exp(-\gamma_2 t) \times [\cos\theta\cos r\theta \\
& + \sin\theta\sin r\theta\sin r\pi/2 + \cos r\pi/2\sin\theta(\cos\theta + \cos r\theta)]\mathrm{Var}(Q_2) \\
\approx \quad & [(2 - 2\exp(-\gamma_1 t)]\mathrm{Var}(Q_1) \\
& + \{2 - 2\exp(-\gamma_2 t)[\cos\theta\cos r\theta + \sin\theta\sin r\theta]\}\mathrm{Var}(Q_2),
\end{aligned} \tag{4.37}$$

where the last approximation ($\sin r\pi/2 = 1, \cos r\pi/2 = 0$), assumes r is sufficiently close to one.

As our pulsing sequence consists actually of more pulses than what is assumed above, the exact analytical formulae are more complicated but the above derivations capture the essential physics. For completeness we quote here the full formula that is plotted with data in Fig. 3(b), which is for the pulse sequence given by Eq. 4.12

$$\begin{aligned}
\sigma^2 = \quad & \Big[\frac{1}{8}(2\cos(\theta) + (1 - 2\cos(\theta))\cos(\pi r) - 4\cos(\theta r) \\
& + (2\sin(\theta) + 1)\cos\left(\frac{3\pi r}{2}\right) + (1 - 2\sin(\theta))\cos\left(\frac{5\pi r}{2}\right) + 1\Big)^2 \\
+ \quad & \frac{1}{8}\Big((2\sin(\theta) + 1)\sin\left(\frac{3\pi r}{2}\right) + (1 - 2\sin(\theta))\sin\left(\frac{5\pi r}{2}\right) \\
& + 4\sin(\theta r) + (1 - 2\cos(\theta))\sin(\pi r))^2\Big]\mathrm{Var}(Q_2)
\end{aligned} \tag{4.38}$$

This is without thermal dephasing (meaning $\gamma_i = 0$), which means there is no contribution from $\mathrm{Var}(Q_1)$.

5

IMPROVING OPTICAL COUPLING TO SLICED NANOBEAM DEVICES IN A FREE SPACE SETUP

We present the design and realization of sliced photonic crystal nanobeam cavities that are coupled to on-chip waveguides, to facilitate efficient optomechanical displacement measurement.

5.1. MOTIVATION

One of the central goals in quantum optomechanics is to characterize mechanical states at the quantum level through the most sensitive possible measurements of mechanical motion. The parametric coupling of a mechanical mode to a cavity allows conversion of quantum-level information on mechanical displacement to a light field that leaks out of the cavity. Detection of the emanating photons enables control over the quantum state of the resonator through projective measurement or active feedback [44, 78]. Moreover, the mechanism allows mechanical resonators to be used as transducers of quantum information, enabled by the conversion of a mechanical quantum state to that of propagating photons and vice versa [74, 87, 88]. For any of these applications, having an efficient coupling of light waves to and from the cavity is an important requirement. Inefficient coupling unavoidably leads to loss of (quantum) information on the mechanical state, thus limiting the fidelity of conversion or control. For example, to cool a mechanical resonator to a thermal occupancy below unity through measurement feedback, a total measurement efficiency (including detection losses and coupling to the cavity mode) of at least 1/9 is needed to ensure that heating through excess measurement backaction is not too large [78, 89–91]. Such conditions often come *in addition* to reaching a sufficient measurement strength or (quantum) cooperativity.

In the previous chapter we have shown how nano-optomechanical systems can bring quantum-level mechanical measurements with single nanosecond pulses within reach. A pronounced limitation of the employed devices was the efficiency η with which the cavity mode coupled to the light field that could be detected. Indeed, we project that improving this coupling efficiency to $\eta \geq 8\%$, without changing any other parameters including the pulse power, would bring the uncertainty in one quadrature below the value of the ground state motional amplitude x_{zpf}. That would allow squeezed state preparation and observing quantum back-action [19] from a single pulsed measurement. For the measurements shown in the preceding chapter we use a form of direct free-space coupling to our structures. The collimated laser beam in the excitation path is focused to couple to the far-field scattering profile of the nanobeam at normal incidence. Regular photonic crystal cavities are designed not to radiate to free space. While the introduction of a double-period grating can increase the coupling to normal-incidence light to a certain degree [51], the typical coupling efficiencies that we can obtain in this configuration are still modest: of the order of $\eta \leq 1\%$.

Various possible solutions for efficient coupling to photonic crystal nanobeams cavities have been presented in literature. In figure 5.1a) a dimpled fiber is employed [5]: the dimple consists of a region of an optical fiber that is first tapered (by stretching the fiber while heating the fiber glass close to the melting point) and then bent to produce a curved section that allows to closely approach to the nanobeam. The tapering guarantees that the optical mode in the fiber converts adiabatically from one that is confined to the core of an optical fiber to one that has a significant evanescent field outside the fiber in its thinnest part. That evanescent field allows coupling to the nanobeam cavity mode, with a rate that is tuned by varying the dimple-nanobeam separation distance. At the same time the curvature allows to

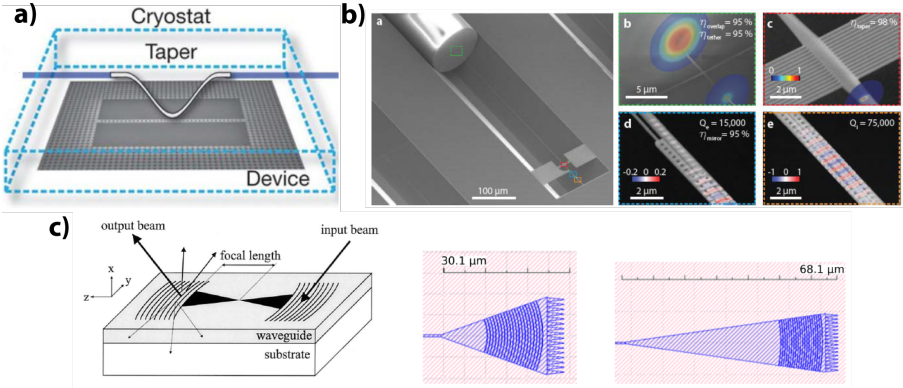

Figure 5.1: Different coupling strategies. Panel a) shows a schematic of the dimpled fiber method shown by Chan et al. [5]. In panel b) Meenehan et al show the coupling from a cleaved fiber to a waveguide, that is side-coupled to a nanobeam cavity[92]. In panel c) Schmeing et al couple light from a lensed fiber with a grating coupler to a waveguide, which can in turn be coupled to a nanobeam cavity[93]. The drawing on the left [94] encompasses the whole geometry.

have a better mechanical control over the point where the fiber makes contact with the sample to keep it stable, while maintaining a finite distance between the fiber and the nanocavity. In figure 5.1b a cleaved fiber is used to couple light to a waveguide through end-fire coupling [92]. Careful alignment and mode matching of the fiber core to the waveguide end are needed. The waveguide runs parallel to the nanobeam cavity such that the waveguide mode can couple evanescently to the adjacent cavity, with a rate that is again controlled through the (now lithographically defined) waveguide-cavity separation. In figure 5.1c a grating coupler is used to couple light from a optical fiber to an integrated waveguide which feeds light to a nanobeam device as in the previous case [93].

5.2. DESIGN

In this chapter we explore the possibility to achieve efficient coupling to sliced photonic crystal nanobeam cavities by making use of integrated waveguides. We are particularly interested in a solution that allows coupling to free-space focused laser beam, such that it can be directly incorporated in the existing cryogenic optical homodyne setup. This also removes the complication of introducing piezo-electric positioning stages for fiber alignment in the cryostat. Figure 5.2 shows a schematic that illustrates the concept. It incorporates a waveguide that ends in an inverted taper [95], which allows the efficient conversion of the optical mode in the waveguide to one with weaker confinement near the end of the waveguide, that can be end-coupled to a beam or fiber. Inverted tapers have been shown to allow efficient coupling to lensed fibers, which produce beams that are focused down to a few micrometers [96]. It is therefore likely that the taper can be designed such that its mode is also matched well to beam profile in the free-space focus of a macroscopic

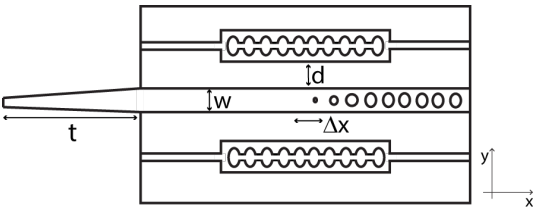

Figure 5.2: Illustration of the top view of the design architecture we employ. Two sliced nanobeams are placed on each side of a central waveguide. The waveguide includes a Bragg reflector (on the right side) and terminates in a tapered ending on the left. The dimensions are on purpose not in scale, to allow recognition of the main futures that characterize the design.

objective lens. The light that is then coupled into the waveguide is brought in the evanescent field of the cavity mode of a sliced nanobeam device. In order to double the yield we design two cavities positioned at either side of the waveguide. Moreover, we design a Bragg reflector in the waveguide such that it becomes single-sided, maximizing the collection efficiency in reflection measurements. In the following paragraphs we discuss the optimization steps needed for the design by tackling the different components separately.

5.2.1. COUPLING A SLICED NANOBEAM TO A WAVEGUIDE

In order to achieve good coupling efficiencies between a sliced nanobeams cavity and the waveguide, we need to design the waveguide to have a good spatial overlap of the (evanescent) fields of the waveguide and the cavity. In particular, their wavevectors, which determines the periodicity of the standing wave profile in both elements, should be equal. This can be attained by matching the effective refractive indices of the modes. Because the cavity mode is a weakly localized standing wave profile, it contains a range of spatial frequencies along the direction of the beam. We can quantify the spatial frequency content by taking a Fourier transform of the mode profile along a line parallel to the nanobeam. From the mean of the Fourier distribution, we estimate the effective wavevector k of the cavity mode. Together with the mode frequency ω, this allows us to define an effective refractive index as

$$n_{\text{eff}} = \frac{kc}{\omega}. \tag{5.1}$$

We expect that the best coupling is achieved for a waveguide that has a matching effective index. We use the corresponding waveguide width as a starting point for further (computationally more expensive) three-dimensional simulations of the coupled waveguide-cavity system. In order to create a slot waveguide that is compatible to the designed cavity mode, we vary the waveguide width w and look for a mode with an effective refractive index that matches that of the sliced nanobeam cavity mode, as depicted in Fig. 5.3. We note that we cannot vary the thickness as this is fixed by the SOI wafer to be $\simeq 220$ nm. The result is shown in Fig.5.3c, where we show the result of simulations of the waveguide eigenmodes using COMSOL finite-element method, yielding n_{eff} for a given value of ω and the

refractive index of silicon $n = 3.6730$.

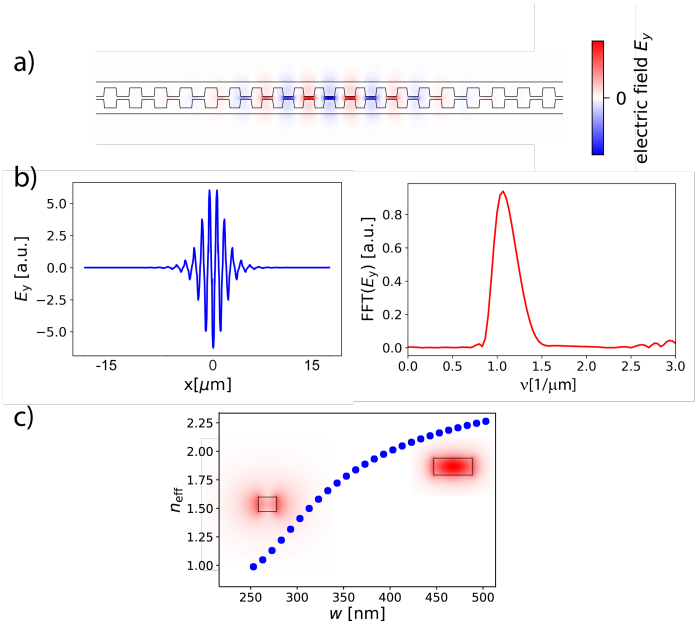

Figure 5.3: a) Simulated nanobeam cavity mode using COMSOL finite-element method, the color bar shows the y component of the electric field E_y. b) The electric field profile of the cavity mode is calculated along a crosscut that extends through the length of the nanobeam in the center of the gap, and its Fourier transform is evaluated yielding a mean $n_{\text{eff}} \simeq 1.62$ for the 205 THz mode shown in the plot. The plot shows the y component of the electric field E_y along the spatial direction x, and the absolute value of its Fourier transform as a function of the linear wavenumber ν. c) We simulate an infinitely extended waveguide of rectangular cross section (insets show the energy density): as the width is varied we obtain a field profile that is more localized in the core (edges) of the waveguide for larger (smaller) widths. By reading the corresponding refractive index we can choose the waveguide width of ~ 309 nm.

To study the coupling of the sliced nanobeam cavity mode to the chosen waveguide we simulate the collective optical modes of the combined waveguide-nanobeam system (Fig.5.4a), by solving for Maxwell's equations in the absence of a driving field. We focus in the first instance on the system that includes a simple straight waveguide without the Bragg reflector, such that it has two open ends. We limit the simulation to only half of the nanobeam since the structure is mirror symmetric with respect to the middle, where we use a symmetric boundary condition (*perfect electric conductor*). The surface corresponding to this mirror symmetry is perpendicular to the top view shown in Fig.5.4 and corresponds to the leftmost vertical edge of the domain shown in the figure. Around the rest of the domain, including the rightmost edge parallel to the aforementioned mirror symmetric surface, we use *perfectly matched layer* (PML) boundaries which absorbs all the energy. The structure eigenmode in the waveguide presents a standing wave close to the left edge that is due to the presence of the symmetric boundary condition, and matches the standing wave in the cavity to which it is coupled.

On the right end of the waveguide, no standing wave is seen as the field there resembles an outward propagating wave that is absorbed in the PML on the right. The nanobeam will in fact radiate into both the left and the right waveguide in the considered geometry, but due to our use of a mirror boundary condition we only show the waveguide that leaves to the right. By bringing the waveguide close to the nanobeam we introduce that decay channel to the cavity mode: the field can evanescently leak from the waveguide to the nanobeam and vice versa with a rate that depends on the distance between the two elements. In order to calculate the coupling rate to the waveguide we divide the power that passes through the end facet of the waveguide in the simulation domain P_{wg} by the total energy E_{tot}, i.e. the integrated energy density in the full simulation domain. Figure 5.4b (blue dots) shows the coupling rate of the nanobeam to the waveguide as a function of the distance between the two elements. It shows an exponentially decaying trend with increasing distance, as expected for the overlap of evanescently decaying fields. Finally we evaluate the corresponding coupling efficiency by comparing

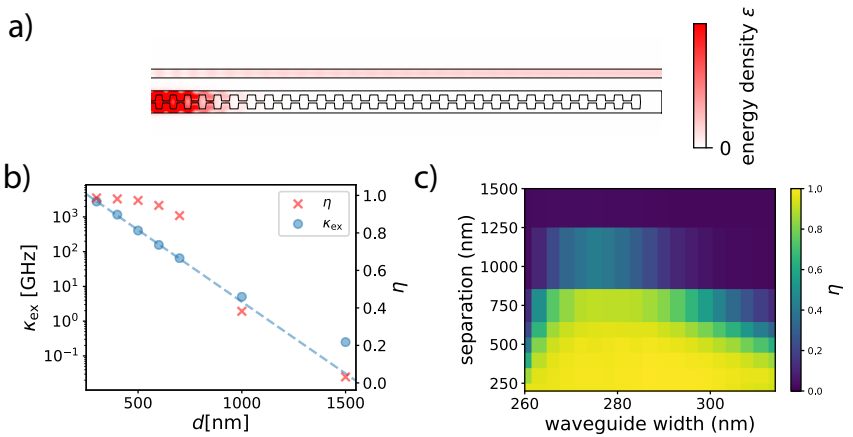

Figure 5.4: a) Simulated energy density for the waveguide-nanobeam system. The scale of the energy density is clipped to 13.6% of the maximum value, to enhance the the visibility of the field in the waveguide. b) Dependence of coupling rate κ_{ex} and coupling efficiency η on the separation d between the two components for a waveguide of fixed width $w = 270$ nm. c) Three dimensional plot showing the efficiency η (color bar) as the waveguide-nanobeam separation distance as well as the waveguide width is varied.

the coupling rate to the waveguide with the total loss rate of the cavity mode $\kappa = 2\,\mathrm{Im}\,(\tilde{\omega})$, where $\mathrm{Im}\,(\tilde{\omega})$ is the imaginary part of the complex mode frequency $\tilde{\omega}$, as obtained from the eigenmode simulation with open (perfectly matched layer) boundary condition[1]. The coupling efficiency to the waveguide is defined as

$$\eta = \frac{\kappa_{\mathrm{ex}}}{\kappa} = \frac{\kappa_{\mathrm{ex}}}{2\,\mathrm{Im}\,(\tilde{\omega})}. \tag{5.2}$$

[1]The factor 2 accounts for the conversion from amplitude to energy decay rate.

In general, three regimes of under-coupling ($\eta < 0.5$), critical coupling ($\eta = 0.5$) and over-coupling ($\eta > 0.5$) can be distinguished [65]. We note that in this simulation, the calculated decay rate in absence of the waveguide is given by $2\pi \times 1.3$GHz, and related only to the residual free-space radiation in this design. Of course, in a realistic experiment, other loss mechanisms due to imperfections may play a role, affecting the value of η. Importantly, we recognize in Fig. 5.4b that for small separations, the calculated efficiency approaches unity[2]. That means that the presence of the waveguide does not induce extra losses into radiation other than the waveguide mode. In other words, the so-called 'ideality' of the coupling is high[97]. Figure 5.4c shows the calculated coupling efficiency η as a function of both the waveguide-nanobeam separation distance d and the waveguide width w. We can see that the resulting optimal waveguide width obtained with this method is close to the initial guess obtained through the effective index analysis in Fig.5.3.

5.2.2. WAVEGUIDE MIRROR

With the aim of performing reflection measurements in which the incoming light carried by the waveguide interacts with the sliced nanobeam cavity mode and is then scattered back solely to the same input/output-coupling channel, we design a Bragg reflector at one end of the waveguide that suppresses transmission [98, 99]. We design the Bragg reflector while keeping the constraint for the effective index of the waveguide to remain equal to the one of the 270 nm waveguide without holes, which we have found in the previous section (Fig.5.5). A Bragg reflector is a photonic crystal with a bandgap in the desired range of frequencies [99], such that a plane wave with frequency in the bandgap has an imaginary wavevector in the photonic crystal and therefore decays exponentially in the crystal. In order to engineer it we study the dispersion curve of the photonic crystal. We study an infinite crystal by simulating a single unit cell with periodic (Floquet) boundary conditions, opting for elliptic holes[3]. We transition adiabatically from the waveguide (without holes) to the mirror (with unit cell taken from simulations) by linear tapering of the bandgap size (from 0 to 30 THz). We use this design principle in order to vary the *mirror strength* (i.e. the relative size of the bandgap) to reduce scattering that would arise from an abrupt change in the reflection coefficient at the boundary with the Bragg reflector. Thus, the boundary is tapered, much like the mirrors that define the photonic crystal cavity. In Fig.5.5b we show how the size of the Bragg reflector bandgap depends on the hole radius and the waveguide width. By fixing the desired bandgap size and reading the corresponding hole radius one can choose the optimal waveguide width that hole radius. This can be done for each hole such as to create the desired structure.

The last ingredient we need is the optimal relative longitudinal position of the mirror with respect to the cavity mode. By sliding the mirror alongside the nanobeam we vary the overlap between the nanobeam cavity mode and the

[2] The value of η here corresponds for the full structure to the decay into both left and right waveguides. Per waveguide direction, the coupling efficiency is 0.5, as expected for an ideal two-sided cavity.

[3] By matching the aspect ratio of elliptic holes with the one of mirror unit cell, it is possible to avoid thin features in the design while maximizing the amount of vacuum in the structure hence the bandgap size.

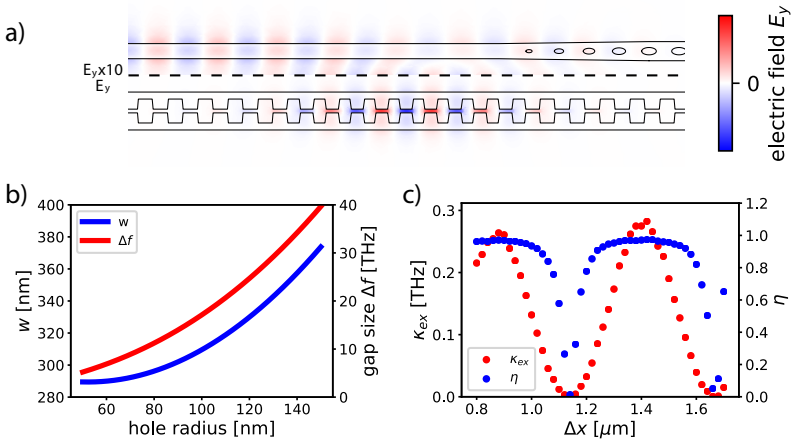

Figure 5.5: a) Simulated electric field profile (E_y component of a calculated eigenmode) of the nanobeam-waveguide system, including a Bragg reflector. The electric field in the waveguide is enhanced by a factor 10 to make it visible. b) Waveguide width corresponding to the constant effective mode index and mirror strength as a function of the Bragg reflector hole radius. c) Coupling rate κ_{ex} and efficiency η as a function of the relative horizontal position between the nanobeam and waveguide.

waveguide mode by modifying the relative phase difference between the two. In Fig.5.5c we plot the effect on both the coupling rate κ_{ex} and η, calculated from the eigenmodes as described in the previous section. The resulting parameters for the mirror are the following: the unit cell length is 540 nm and its width 345 nm, the ellipse diameters are 264 nm and 132 nm. The tapering of hole diameters is done linearly in 5 steps, while the waveguide width is smoothly varied. The optimal δ_x distance is 1.4 um, which is independent of the cavity-waveguide separation distance.

5.2.3. TAPERED WAVEGUIDE

One of the main objectives of this coupling strategy is to facilitate coupling to a free-space, Gaussian-like light beam. For this purpose we design an inverted taper ending to the waveguide. The tapering serves to match the mode in the waveguide with the large Gaussian mode diameter of the in-coupling laser after the objective lens, which should simultaneously permit an efficient collection of light from the waveguide through the same lens. By varying the width of the taper we change the refractive index of the waveguide. By progressively lowering the refractive index contrast the corresponding mode effective index n_{eff} becomes smaller, causing the mode to become less confined. This means that the mode's energy density becomes progressively located in the evanescent field outside of the waveguide.

We compare the expanding diameter of the beam that is radiated by the waveguide into free-space with the spatial profile of a beam focused on the end facet of the waveguide (Fig.5.6). We see that the beam radiated by the waveguide has a nearly Gaussian beam profile (Fig.5.6a). Figure5.6b shows how the width of

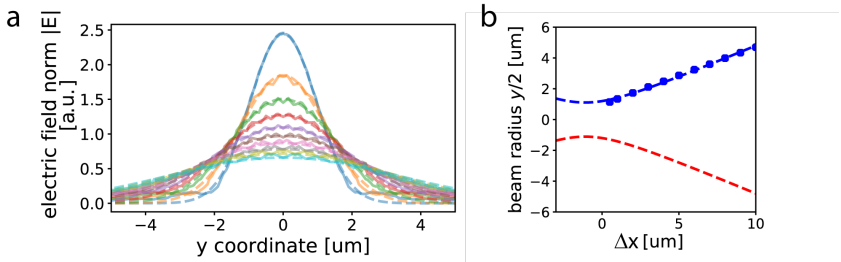

Figure 5.6: a) Beam profile (electric field norm) in the y-direction of the field scattered by a (non-tapered) waveguide similar to the one in Fig.5.7a. The different curves represent crosscuts of the beam along the propagation direction z. The blue curve is 1μm distant from the end facet of the waveguide and the others follow at a pace of 1 μm distance to each other. b) Comparison between the beam spot size in the propagation direction after a lens, equation 5.3, with the radius of the scattered field as in a) (blue dots). The blue dashed curve is a fit of equation 5.3 to the blue data points.

the fitted Gaussian increases with distance from the waveguide end, defining the opening angle of a lens used to collect from or excite the waveguide. For a focused laser beam, the spot size parameter y describes the beam diameter as the field propagates in the direction $\hat{z}$. Its expression [100] as a function of the position z is

$$y(z) = y_0 \sqrt{1 + \left(\frac{z}{z_R}\right)^2}, \tag{5.3}$$

where y_0 is the width of the beam at the focal plane and $z_R = \pi y_0^2/\lambda$ is the Rayleigh length[4].

To assess whether a tapering profile will convert the guided mode adiabatically in the propagation direction one can use the definition of the adiabaticity parameter δ (as given by Meenehan [92])

$$\delta = \max\left[\left(\left| n_{\text{eff},0} - n_{\text{eff,j}} \right| \right)^{-1} \frac{dw}{dz} \right]_{z,j} \tag{5.4}$$

where $n_{\text{eff},0}$ is the effective index of the guided mode and $n_{\text{eff,j}}$ is the effective index of the j-th radiation mode in the continuum outside the waveguide. When $\delta \ll 1$, the given tapering profile successfully converts the confined mode adiabatically in the propagation direction. We assume that the radiating modes that propagate in air have $n_{\text{eff,j}} \leq 1$. Since the field has to be almost completely evanescent to be able to have a waist size that is compatible to the beam focused from the objective lens then $n_{\text{eff},0} \simeq 0$. This means that dw/dz has to be small in order to avoid unwanted scattering to other modes.

In order to estimate the collection efficiency at the objective lens, we simulate the far field scattering profile and compare it with the 0.55 NA of the objective lens. We compare the results for a straight ending (Fig.5.7a) and for a tapered end of

[4]The distance along the propagation direction of a beam from the waist to the place where the area of the cross section is doubled [101].

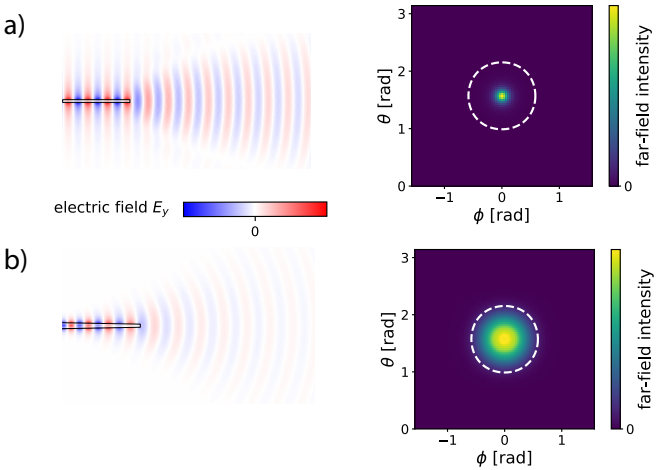

Figure 5.7: a) Simulated scattered field from the ending facet of the waveguide without tapering and corresponding radiation pattern. The white dashed ring represents the collection lens. b) Simulated scattered field for a tapering profile with an initial width of $w = 500$ nm and an ending width of 200 nm, with a length of 15 μm and corresponding radiation pattern.

the waveguide (Fig.5.7b) together with the radiation pattern calculations for the two cases. The radiation profiles are compared with the aperture of the existing collection lens in the setup (white dashed line). The fraction of intensity within the NA for the taper is 92% and without the taper is 97%, considering for both structures an end facet of 200 nm. We therefore conclude that the method in principle should yield good results, even though these could be hindered by imperfections in the alignment with respect to the taper and limited by fabrication imperfections which could induce unwanted scattering.

5.3. NANOFABRICATION

In the following, we describe the methods we developed to realize the designed devices. For the structure that we experimentally investigate in section 5.5, the design parameters chosen for the fabrication are: 272 nm waveguide width at the cavity, 500 nm waveguide width at the tethers crossing, 17 μm is the length of the taper from the tethers until the end facet, and 200 nm end facet width. For the mirror we use 19 holes (plus 5 tapering holes). We fabricate structures with three different waveguide-cavity separation distances of 450, 700 and 950 nm (corresponding to design coupling rates of $2\pi \times (200, 20, 2)$ GHz, respectively. To fabricate the devices presented in this chapter, we modify the procedure described in section 1.3.2. The main difference in this case is that we want to fabricate the devices such that the tapered waveguide ending sits at the edge of the silicon chip. We will describe in the next section a measurement scheme that will allow us to access the structures with a free space in-coupling laser beam. For this to be possible the ending facet of the tapered waveguide has to lie as close as possible to the chip edge. In the previous

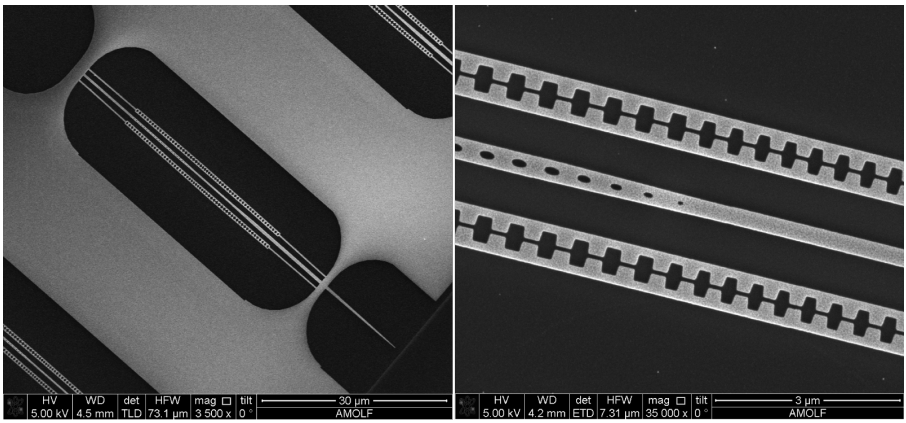

Figure 5.8: SEM top view of fabricated nanodevices. Left picture shows the entire architecture composed of two sliced nanobeams with the waveguide in the middle ending at the edge of the chip. On the right we show a close up of the central part of the architecture at the inset of the Bragg reflector.

fabrication procedure we would prepare a mask layer of HSQ on a squared 0.5 inch× 0.5 inch SOI chip and pattern the mask layer in the middle where its thickness is uniform. For the new devices, a patterning at the edge of the chip, without changing the preparation of the HSQ mask would not yield good results due to the gradient in the resist thickness from center to edge of the spincoated region. To circumvent this problem we cleave the chips after applying the resist layer with the following procedure. We first use a diamond tip to mark the edges of the surface along which we want to cleave. We work once again with 0.5 inch× 0.5 inch SOI chip and we apply the markers in the middle of two opposite sides. To avoid unwanted particles generated by the diamond marking depositing on the top silicon layer, we sonicate the samples. At this point we apply the resist layer by spincoating with the usual procedure. After baking the resist we finally perform mechanical cleaving of the chips along the surface determined by two diamond-marked spots. The crystalline nature of the silicon ensures that the sample cleaves along a crystal plane. This is important since it determines how straight the sample edge is and how well we will be able to perform the electron beam alignment for the patterning step.

Once we have created a uniform layer with the desired ∼ 50 nm HSQ thickness at the edge of the chip we proceed with the electron beam patterning step. To determine the region along the chip edge where we want to write the devices mask we use the optical microscope and check that we have a straight region along the edge that is at least 2 mm wide. We therefore record a microscopic map of the edge. When performing the alignment of the electron beam coordinate system we will use the points at the two extremes of this region. Since we need to avoid exposing the region that we want to pattern with the electron beam during the alignment step, we are left with some uncertainty about the quality of the edge within the exposure region. The only information we have about this region is indeed given by optical microscopy. We can resolve indentations that have a width of about 1 μm. For this

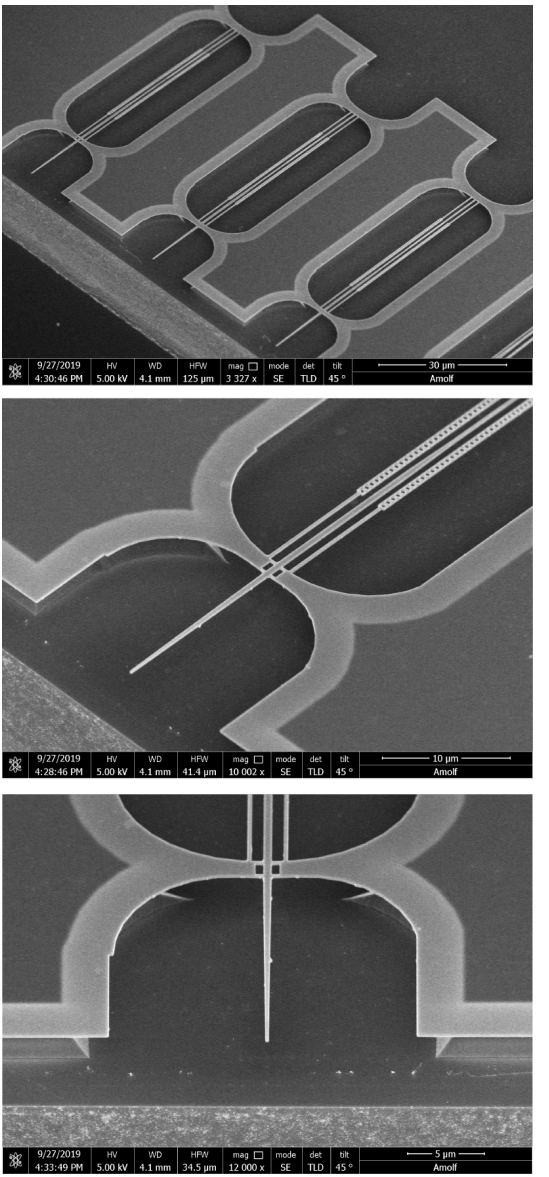

Figure 5.9: The three SEM images show tilted views of the devices. The suspended parts appear brighter under SEM, making it possible to see the central part of support pads in a darker contrast because of the presence of glass underneath. The waveguide tapers face the edge of the chip, which is also visible in the images.

reason we pattern multiple copies of the structures at different distances that span from $+1$ μm to -1 μm with respect to the estimated position of the sample edge. The remaining steps of the fabrication procedure are practically unchanged, except for

the obvious need to avoid handling the edge of the sample on which the structures are written. Figures 5.8,5.9 depict results of fabricated devices, showing that these can indeed be fabricated within distances of approximately 1 μm from the cleaved edge. The successful fabrication of these devices is dependent also on the correct suspensions geometry we chose. Due to tensile stress in the top silicon layer of the SOI, the membranes tend to buckle if the support structure is too bulky. On the other hand, very thin suspension tethers tend to collapse due to the electrostatic attraction of the top silicon layer to the bottom substrate.

5.4. OPTICAL CHARACTERIZATION

These samples are expected to allow significant optical coupling efficiencies to a focused Gaussian light beam, either coming from a macroscopic lens such as in our cryogenic setup, or from a lensed fiber as long as the numerical aperture of the lens is matched to the divergence of the field radiated from the inverted taper waveguide. In appendix 5.7, we describe some practical suggestions of how to facilitate free-space coupling in the cryostat while allowing imaging of the sample at the same time. In the following, we characterize the optical coupling efficiency of the devices in a room-temperature setup where we achieve end-fire coupling to a lensed fiber. We start by deriving expressions for the optical response including the various efficiencies in part of the system, which hold generally for any way of optically addressing the waveguide.

5.4.1. COUPLING EFFICIENCY IN INPUT-OUTPUT RELATIONS

We proceed to derive an expression for the reflectivity of the tapered waveguide based on the system parameters as indicated in the sketch of Fig. 5.10. As we saw in

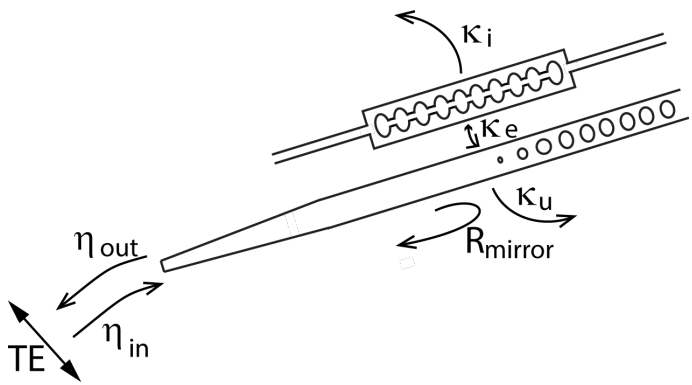

Figure 5.10: The drawing indicates the relevant quantities for the quantitative description. These are defined in the main text.

chapter 2 the intracavity amplitude of the mode in the nanobeam is

$$a = \frac{\sqrt{\kappa_e}}{-i\Delta + \kappa/2}\sqrt{\eta_{\text{in}}}s_{\text{in}}, \tag{5.5}$$

where the total cavity decay rate $\kappa = \kappa_i + \kappa_e + \kappa_u$ is the sum of the intrinsic cavity decay rate in absence of the waveguide κ_i, the coupling rate of the cavity to the waveguide mode $\kappa_e = \kappa_e(d)$ that depends on the cavity-waveguide separation distance d, and $\kappa_u = \kappa_u(d)$ which represents the unwanted extra losses of the cavity to undetected channels, induced by the presence of the waveguide. The symbol η_{in} is the coupling efficiency of a focused input beam with the *TE*-polarized mode in the waveguide, and includes mode overlap and propagation losses. The amplitude of the in-coupling beam s_{in} is normalized such that $|s_{\text{in}}|^2 = P_{\text{in}}$ is the power in the beam. We can write the output field amplitude as

$$\begin{aligned} s_{\text{out}} &= -\sqrt{\eta_{\text{in}}\eta_{\text{out}}R_{\text{mir}}}s_{\text{in}} + \sqrt{\kappa_e}a\sqrt{\eta_{\text{out}}} \\ &= -\sqrt{\eta_{\text{in}}\eta_{\text{out}}R_{\text{mir}}}s_{\text{in}} + \frac{\kappa_e}{-i\Delta+\kappa/2}\sqrt{\eta_{\text{in}}\eta_{\text{out}}}s_{\text{in}}, \end{aligned} \tag{5.6}$$

where R_{mir} is the reflectivity of the Bragg mirror and η_{out} is the output efficiency to the *TE* beam, which includes aperture losses and propagation losses. The efficiencies η_{in} and η_{out} are not necessarily the same as the incident and outgoing beams can generally have different shape. If the input and output fields propagate in a single well-defined mode, such as that of a fiber, reciprocity dictates $\eta_{\text{in}} = \eta_{\text{out}}$. From input-output theory (section 2.2.1) we can retrieve an expression for the reflectance

$$|r_{\text{TE}}|^2 = \left|\frac{s_{\text{out}}}{s_{\text{in}}}\right|^2 = \eta_{\text{in}}\eta_{\text{out}}\left(R_{\text{mir}} - \frac{\kappa_e(\kappa\sqrt{R_{\text{mir}}}-\kappa_e)}{\Delta^2+(\kappa/2)^2}\right). \tag{5.7}$$

Here we assume that there is no direct reflection back into the detected beam from the inverted taper end. By making the reasonable assumption of high mirror reflectivity $R_{\text{mir}} = 1$ we obtain

$$|r_{\text{TE}}|^2 = \eta_{\text{in}}\eta_{\text{out}}\left(1 - \frac{\kappa_e(\kappa-\kappa_e)}{\Delta^2+(\kappa/2)^2}\right) \tag{5.8}$$

5.5. CHARACTERIZATION WITH A FIBER COUPLED SETUP

In order to test the fabricated devices and investigate if the sliced nanobeams cavities can be coupled well to adjacent waveguides, we choose to use a direct detection scheme in a fiber-coupled setup. This is a convenient way of characterization since we can employ a lensed fiber coupling to the tapered waveguide which allows rapid investigation of multiple devices. The close proximity of the fiber with respect to the taper ensures us that we only probe the tapered waveguide. In this way we can test one-to-one the efficacy of the taper waveguide in feeding light in and out to the sliced nanobeams. In Fig.5.11 we show a schematic of the employed setup which employs a New Focus Velocity 6700 (1430 – 1510 nm bandwidth) tunable narrowband diode laser to probe the structures in high vacuum (pressure around $4 \cdot 10^{-5}$ mbar) obtained with a Pfeiffer Hicube classic pump. The signal is detected by a New Focus 1811 DC detector with a 125 MHz bandwidth and sent to a Tektronix DPO4034B oscilloscope (the bandwidth for the plot in Fig.5.14 is 350 MHz) and to a Agilent MXAN9020A electronic spectrum analyzer (the resolution bandwidth for the plot in Fig.5.12 is 191 Hz).

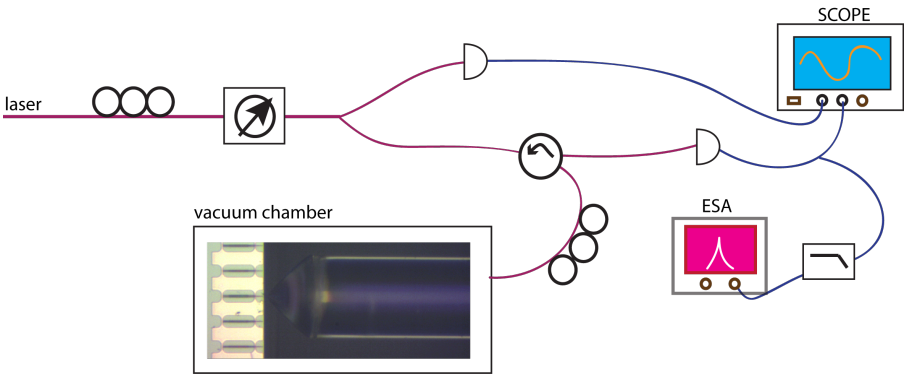

Figure 5.11: Schematic of the fiber-based characterization setup. The incoming laser beam is fiber coupled to the rest of the setup. After choosing the beam polarization with polarization pedals and its intensity with a variable attenuator, the beam is split into two fibers. One of the resulting beams is detected by a photodiode which output is given to an oscilloscope. The other beam is sent to a circulator such that the light in the input port is carried by a lensed fiber directly to the sample (the inset shows a microscope picture where a column of samples can be recognized together with the lensed fiber) in the vacuum chamber after it polarization is again controlled. The reflected signal is detected by a photodiode and consequently to the electronic devices: electronic spectrum analyzer and oscilloscope.

In direct detection measurements the reflectance R describing the optical resonance as a function of laser detuning can generally have a Fano lineshape, whose precise shape is determined by the relative phase of direct reflection and the cavity mode contribution to the reflected field. In eq. 5.8, we assume that there is no reflection from the taper end, and that the phase difference between the waveguide mirror reflection and the cavity radiation is zero. This leads to a prediction of a Lorentzian lineshape, which we will test in the following. It has been shown by Leijssen et al. [50] that the band power (i.e. the integral of the power spectrum) is proportional to the square of the reflectance derivative with respect to the relative detuning parameter $u = 2\Delta/\kappa$, with Δ the laser detuning and κ the total cavity decay rate. For thermal motion, the band power BP, i.e. the variance of the output signal P_{out} has the form

$$BP = \langle P_{\text{out}}^2 \rangle_{\text{th}} = \frac{8 n_{\text{th}} g_0^2 P_{\text{in}}^2}{\kappa^2} \left(\frac{\partial R}{\partial u} \right)^2 \tag{5.9}$$

where P_{in} is the incident power, g_0 the single photon-phonon coupling rate and $n_{\text{th}} = k_B T/\hbar\omega_m$ the thermal occupancy of the mechanical mode with frequency ω_m.

For the sample we investigate in this section, we observe optical wavelengths located in the range between 1450 nm and 1465 nm with quality factors of about $Q \sim 10^4$. When the cavity is getting closer to the waveguide, in the case of 450 nm spacing, the optical Q is on the order of 10^3, as we will quantify in detail later. Mechanical frequencies for this sample are between 1.25 MHz and 1.50 MHz typically. In Fig.5.12a we show a spectrogram of a 1.457 MHz frequency mechanical mode, detected through analyzing the intensity fluctuations of the light reflected from the lensed fiber as we vary the in-coupling laser frequency. The optical spring

shift typical for direct measurements (see [50]) shows the characteristic shape of nonlinear transduction (see section 3.6). The integral of the spectra for each value of the laser wavelength is shown in Fig.5.12b together with the fit of equation 5.9. From the fact that the measured band power is symmetric in laser frequency and zero for the center laser frequency (where the laser must thus be resonant with the cavity), we can conclude that the optical lineshape must be symmetric; with vanishing slope at $\Delta = 0$. As such, we see that the assumption for eq. 5.8 was correct, in contrast to the usual case for direct detection in free space [50]. By extracting the

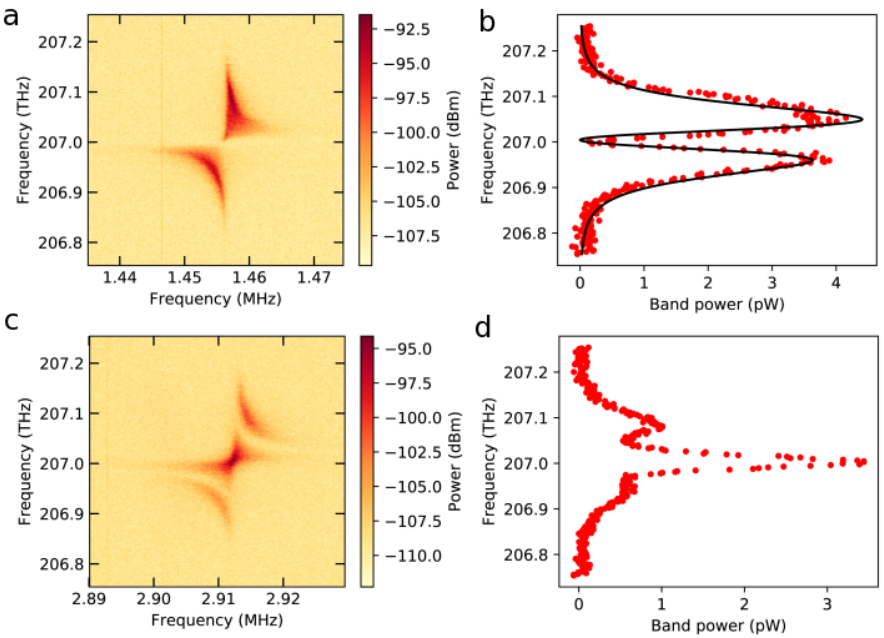

Figure 5.12: a) Spectrogram of the mechanical flexural mode's thermal fluctuations at about 1.46 MHz and b) corresponding band power versus laser frequency. c) Spectrogram of the second harmonic of the mode in a) and corresponding band power in d). The spectrograms are acquired by employing an input power of 10 nW.

linewidth of the resonance from the fit of the band power we can extract κ once we also know what is the root mean square frequency modulation driven by thermal motion $\delta\omega_{\mathrm{rms}}$. In presence of thermal broadening the resonance linewidth is indeed the linewidth of a Voigt function, we use then equation 2.24. In order to extract the parameter $\delta\omega_{\mathrm{rms}}$ we use the model presented in section 2.3.3. We need to get access to the ratio of the band power integrals of the first (Fig.5.12a) and second harmonic of mode ω_m. In Fig.5.12c we show a spectrogram of the second harmonic peak at frequency $2\omega_m$ and Fig.5.12d shows the corresponding band power[5]. By taking the

[5]In the model presented in section 2.3.3 (see Fig.2.10) we could take the ratio between the maximum of the band power as a function of detuning. This is possible since the quadrature averaging method

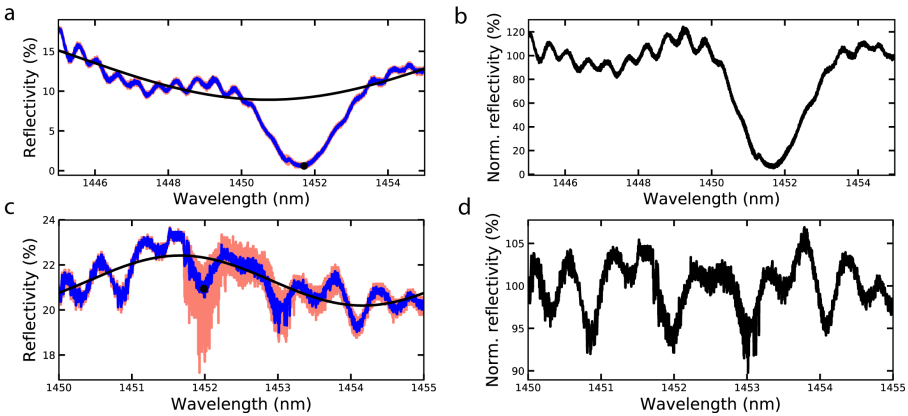

Figure 5.13: a,c)Reflection measurements for devices with a waveguide-nanobeam separation of 700 and 450 nm respectively. The slow modulation in the signal is due to a Fabry-Perot cavity. By taking into account this modulation we renormalize the signals as shown in b,d). Sent powers to the lens fiber: 700 nm device : 1,8 µW, 450 nm device: 3, 7 μW.

ratio of the band power integrals we obtain the parameter $\delta\omega_{\mathrm{rms}}/\kappa$ from which we can then extract κ, using equation 2.24.

In order to conclude whether the coupling between nanobeam and waveguide is successful we want to measure the coupling efficiency $\eta = \kappa_{\mathrm{ex}}/\kappa$, where κ_{ex} is the coupling rate to the waveguide. We can gain access to η in optical reflection measurements by using the expression for the reflection coefficient given in section 2.2.1

$$R = \alpha \left| 1 - \frac{\eta\kappa}{\kappa/2 - i\Delta} \right|^2 \tag{5.11}$$

where α accounts for the imperfect efficiency of the coupling to the waveguide and other experimental losses, η is the waveguide-cavity coupling efficiency, κ the optical decay rate and Δ the optical detuning from resonance. From equation 5.11 we see that the maximum and minimum reflectivity are $R_{\mathrm{max}} = \alpha$ and $R_{\mathrm{min}} = \alpha(1-2\eta)^2$. From those it follows that the efficiency can be written as

$$\eta = \frac{1}{2}\left(1 \pm \sqrt{\frac{R_{\mathrm{min}}}{R_{\mathrm{max}}}}\right), \tag{5.12}$$

where we assume that η does not depend on power, and R_{min} and R_{max} are the maximum and minimum value for the reflectance. In Fig.5.13a,c we show reflection measurements for two example devices whose main difference is the distance d

implies that the functional shape of the band power is the same for all harmonics (section 2.4.1). For the measurements that we are presenting now we take the ratio between the band power integral, which is possible since

$$\int \left(\frac{\partial R}{\partial u}\right)^2 du = \frac{1}{3}\int \left(\frac{\partial^2 R}{\partial u^2}\right)^2 du \tag{5.10}$$

.

between nanobeam and waveguide. The vertical scale is calibrated by measuring the transmission at the two output ports of the 50:50 beam splitter. Figure5.13a shows the reflection measurement for a structure with $d = 700$ nm. A slow modulation is present, which, from the observed free spectral range, we assume is due to a Fabry-Perot resonance caused by reflections between the Bragg mirror and the lensed fiber facet. In Fig. 5.13b we show the normalized reflectivity by dividing the signal by the fitted sine wave with offset shown in Fig. 5.13a. The dip we observe is the signature of the sliced nanobeam optical resonance. The fact that this dip reaches almost zero reflectivity suggests that this device is almost critically coupled to the waveguide, i.e., $\eta \approx 0.4$ or 0.6, according to equation 5.12.

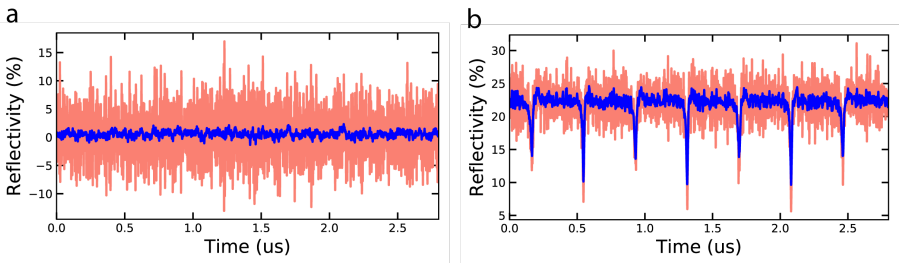

Figure 5.14: Time traces for two devices with waveguide-nanobeam separation of 700 a) and 450 nm b), respectively. The measurements are performed by tuning the laser on resonance with the nanobeam cavity mode and with a power of 100 μW. Red lines show raw data over the full MHz bandwidth of the oscilloscope. Blue data is smoothed with a Savitsky-Golay filtering with a bandwidth of 120 MHz.

Figure 5.13c shows a similar reflection measurement for a sample with cavity-waveguide separation $d = 450$ nm, which presumably should have a higher cavity-waveguide coupling rate. Here, it is much more difficult to discern the optical cavity resonance, even though a measurement of the thermomechanical fluctuations like that in Fig. 5.12 revealed that a cavity mode exists at this wavelength of ~ 1452 nm. In principle, a reduction of visibility is expected if the waveguide is overcoupled. In that case the rate at which the light leaks to the waveguide is higher than the intrinsic cavity decay rate $\kappa_e > \kappa_i$. However, when resolving the signal at high bandwidth on the oscilloscope using a fast photodetector (red curve), we recognize that it is fluctuating significantly more around the expected cavity resonance wavelength than for large detunings. These fluctuations occur at MHz frequencies and can be revealed when the reflectance is measured with a fast photodetector (orange line in Fig. 5.13c). As we know that the large mechanical cavity frequency modulations of order κ in some of our devices effectively 'smears out' the optical response, the measurement in Figs. 5.13c-d cannot be used to faithfully extract the value of η.

However, we can resolve the reflectance at large temporal resolution for the laser positioned at a fixed wavelength close to cavity resonance, as shown in Fig.5.14b for the same sample with $d = 450$ nm. This time trace shows reflection dips occurring every half mechanical period. These can be interpreted as the cavity resonance that is being swept across the laser frequency due to the mechanical oscillation. Although it is not certain that for this laser power the mechanical amplitude is

not driven through dynamical backaction, the depth of these dips should only be related to the optical Lorentzian lineshape in the bad cavity limit. Thus, we can use this time trace to estimate η through the observed minimal and maximal reflection R_{min} and R_{max}, respectively, as observed in the trace. We note that for some other structures, like the one with $d = 700$ nm that is shown in Figs. 5.13a and 5.14a, the thermomechanical detuning excursions are smaller, and the fast oscillations are not observed. In that case, a regular reflection spectrum should be used to obtain R_{min} and R_{max}.

Figure 5.15a and b show the values of κ and η extracted from the mechanical spectrograms and optical response measurements as explained above, for various samples with three different waveguide-cavity separations. First of all, we see that the cavity linewidth generally increases strongly when the waveguide-cavity separation is smaller, indicative of the introduction of an extra loss channel with a decay rate that can be much larger than the typical intrinsic decay of the cavities. Second, clear variations of η are observed. One measurement of the reflectivity gives two possible values for η according to equation 5.12. In other words, in principle from the dip of a Lorentzian in a reflection measurement it cannot be discerned if a cavity is overcoupled or undercoupled. However, we can reasonably assume that a decrease of cavity-waveguide separation leads to an increase of the efficiency rather than a strong decrease. Under that assumption, we select the most reasonable roots of equation 5.12 and plot the corresponding estimated values of the coupling rate κ_{ex} in Fig.5.15c. For the device that is nearly critically coupled (at 700 nm gap), we plot both possible estimates. The decreasing dependence of κ_{ex} with distance between waveguide and cavity in the three cases of $d = 450, 700, 950$ nm allows us conclude that we can successfully tune the coupling between the two elements by varying the structures geometry. In these devices, external coupling rates up to 270GHz are observed for the smallest separations. This is comparable with the theoretical values shown in the previous section. It leads to efficiencies of waveguide-cavity coupling as high as 87%, such that the cavities can be seen as highly overcoupled single-sided cavities.

5.6. DISCUSSION AND CONCLUSIONS

In this chapter we have shown that we can successfully couple the sliced nanobeams to optical waveguides and tune the value of the coupling rate. It is possible to enter the regime of overcoupling that allows fast leverage of photons from the cavity. This is particularly important in pulsing experiments as the measurement strength is proportional to the coupling efficiency (see section 4.1.3). The overall (off-resonant) reflectance in these tests was limited to a value of $\sqrt{\eta_{\mathrm{in}}\eta_{\mathrm{out}}} \approx 10-22\%$. However the results reported in this chapter regard measurements that employ a lensed fiber coupling configuration to the devices. From the theoretical results of the simulations we have the indication that the profile of the radiated beam from the waveguide is that of a Gaussian beam. This profile should be coupled to a free-space lens, matching the numerical aperture to optimize efficiency. With the improved coupling efficiency, the sliced nanobeam devices studied in this thesis are promising candidates for backaction evasion with an imprecision below x_{zpf}, which could lead

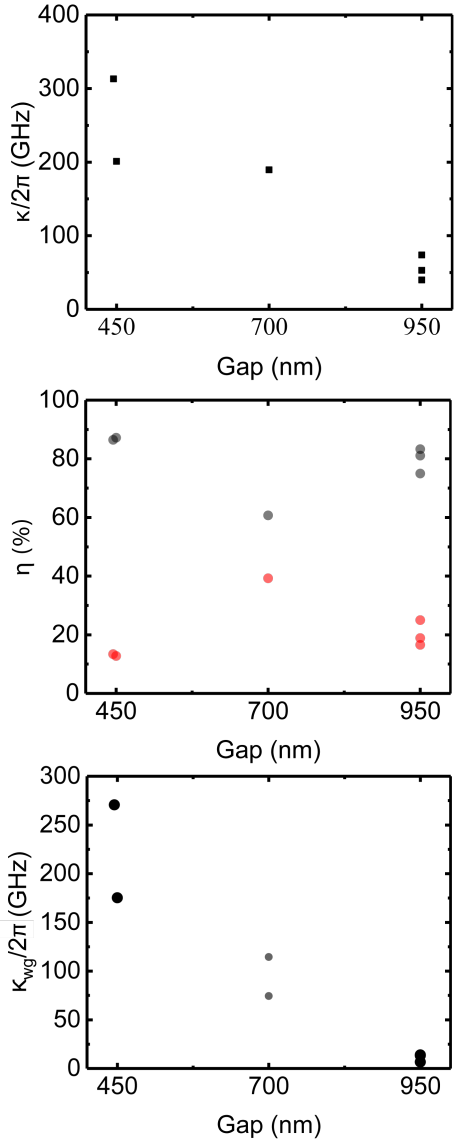

Figure 5.15: a) Optical linewidth as a function of waveguide-nanobeam separation distance extracted from the mechanical spectra. b) Coupling efficiency as a function of waveguide-nanobeam separation distance, equation 5.12. c) Coupling rate extracted by using the results in a,b).

to measurement-based control of quantum states and ultimately to the study of quantum decoherence as well as application as quantum sensors.

5.7. APPENDIX: MODIFICATION OF OPTICAL SETUP FOR FREE-SPACE COUPLING VIA INVERTED TAPER WAVEGUIDES

We design the integrated architecture presented in section 5.2 in order to perform experiments employing a free-space homodyne setup (section 2.2). To couple a free space beam to the tapered waveguide we design and construct a customized sample holder for the employed closed cycle cryostat Montana C2. In Fig.5.16 we show a drawing of the sample holder which is placed such that the silicon chip is parallel to the optical table. Moreover, we implement an imaging mirror that is oriented at 45° with respect to the silicon chip. This mirror is intended to allow imaging the devices from the top through the same window and objective lens that focuses the laser. This could facilitate imaging the samples using a white light source, and observing scattering from the devices when the waveguides are illuminated by the laser. The

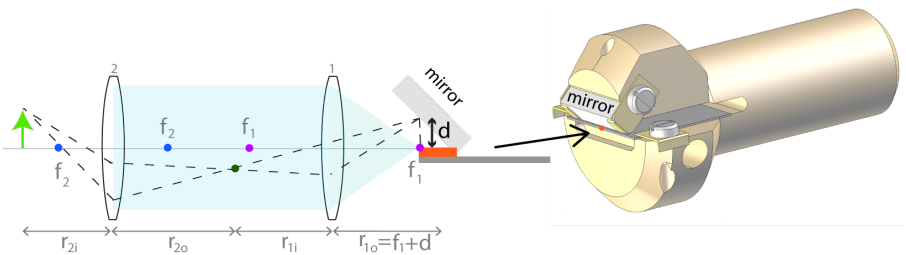

Figure 5.16: In the side view on the left, the laser beam represented in light cyan is focused on the devices (depicted in red) positioned at the edge of the silicon chip. A mirror is placed at 45° with respect to the sample plane. The configuration of two lenses used in the imaging path show how to retrieve an image of the sample edge through the mirror while keeping the objective lens focused on the tapered waveguide ending facet.

working distance that separates the cryostat optical window from the chip edge inside the chamber is approximately ~ 5mm. On the other hand we would like to image the devices at the same time while we keep the end facet of the tapered waveguide in the focal plane in order to use the lens to focus the laser beam. In Fig.5.16 a side view of the sample-mirror system and the excitation and imaging path are shown. The distance between the sample and the lens is $r_{1o} = f_1 + d$ where f_1 is the focal length of lens 1 and d the distance between the chip edge and the mirror surface at perpendicular incidence from the sample. The image generated from lens 1 is the object for the lens 2 which position is indicated by the green circle in the figure, at a distance r_{1i} from lens 1 and r_{2o} from lens 2. Lens 2 will generate an image at a distance r_{2i}. By using the lens formula

$$\frac{1}{f} = \frac{1}{r_i} + \frac{1}{r_o} \tag{5.13}$$

and using that the magnification is $m = d_i / d_o$, lens 2 can be chosen with focal length f_2 such as to obtain the desired magnification. If $L = r_{2o} + r_{1i}$, one can calculate

what the focal length of lens 2 should be

$$\frac{1}{f_2} = \frac{1}{L - d_{1i}} + \frac{1}{d_{2i}}. \tag{5.14}$$

GLANCING AT TINY VIBRATIONS

BACKACTION EVADING MEASUREMENTS OF MECHANICAL MOTION CLOSE TO THE QUANTUM REGIME

SUMMARY

Measurement plays a central role in quantum theory. This thesis explores fundamental and practical limits to the sensitivity of measurements of the mechanical motion of a macroscopic object. Optical measurements of mechanical motion are at the core of the research efforts in this thesis. Extremely sensitive optomechanical measurements can be performed in systems in which a mechanical vibrational mode is co-localized with an optical cavity field. In this work we perform measurements on sliced nanobeam photonic crystal cavities, that operate in the regime in which the mechanical frequency is smaller than the optical cavity linewidth and exhibit large photon-phonon coupling strength.

We employ balanced homodyne interferometry, a well-known detection technique that allows sensitive characterization of light fields. We discuss both continuous and pulsed measurements, distinguished by a measurement time much longer or shorter than an oscillation period, respectively. We show that in continuous measurements it can be useful to introduce a modulation of the reference beam arm length, that corresponds to averaging all optical phases. The measurement signal becomes easy to interpret and allows to characterize the absolute magnitude of a cavity frequency modulation. This is especially relevant in our case, where, due to a high ratio of optomechanical coupling to optical decay rate, the mechanical signal can be transduced nonlinearly. This means that spectroscopic measurements show higher harmonics of the fundamental mechanical modes. Pulsed measurements, in which light pulses have a length of a fraction of the mechanical period, allow probing selectively a single mechanical

quadrature with a sensitivity that can exceed the standard quantum limit.

In ideal optomechanical experiments an optical mode is coupled to a single mechanical mode. This allows optical characterization and control of the quantum state of that degree of freedom. Actual systems always show multiple modes that can limit the level of effective sensitivity and control that can be achieved. We present and experimentally implement a strategy to mitigate the effect of unwanted mechanical modes. We examine in detail the importance of the noise contributions due to the presence of spurious modes and argue how spectral design of the system can optimize those noise contributions even in the presence of perturbations due to random fabrication imperfections. We then implement this design strategy in the case of a sliced photonic crystal nanobeam cavity. We report the mechanical performance of experimental realizations, and evaluate the figures of merit for varying designs, in the contexts of either continuous or pulsed measurement. We finally discuss how the strategy can be interpreted in a model of two coupled modes.

We demonstrate pulsed optomechanical measurements on sliced nanobeams. We show that the sensitivity of these measurements can be close to the quantum regime, achieving a single-pulse measurement imprecision of 9 times the zero-point fluctuation size (x_{zpf}), constrained by optical detection efficiency. We prepare both thermally squeezed and purified (cooled) conditional mechanical states, and perform full state tomography on these. We study how additional mechanical modes affect the conditional state, limiting its width to $58x_{\mathrm{zpf}}$. We demonstrate how mechanical decoherence and re-thermalization can be tracked by recording the state evolution at longer time scales. Furthermore we perform pulsed measurements on structures designed to show a single fundamental first order mechanical mode. These show how the width of the conditional state can be brought down to $28x_{\mathrm{zpf}}$, limited mostly by higher-order mechanical modes.

The sensitivity of our pulsed optomechanics experiment is ultimately limited by detection efficiency. A modest increase of the coupling efficiency of the input/output laser field to the optical cavity mode would be enough to bring the measurement imprecision below the zero-point fluctuation size, allowing squeezed state preparation and studying quantum backaction. We investigate the possibility to increase measurement efficiency through alternative light extraction methods. We design an on-chip architecture that can be used in a free-space setup. We evanescently couple a slab waveguide to the sliced nanobeam cavity. The waveguide is designed to have a tapered ending with a radiation profile that can be mode matched to that of a focused laser beam incoming from the objective lens. We fabricate the devices on the edge of the silicon chip so that the ending facet of the tapered waveguide can lie at a distance equal to the objective focal length. We report spectroscopic measurements aimed at characterizing this on-chip optical coupling method for efficient measurement, and demonstrate that efficient coupling between waveguides and nanocavities can be achieved.

About the author

Giada La Gala was born in 1987 in Acquaviva delle Fonti (Italy). She studied physics at the University of Pavia, obtaining a Bachelor's degree in 2013 with a final research project about Raman spectroscopy applied to forensic sciences. During her studies in Pavia, Giada was active in cultural associations and collections of associations, performing the role of President of the non-profit organization Officine Multimediali Pavesi active in the organizations of events and cultural initiatives.

She continued her studies obtaining a Master's degree from the same University in 2016. During the Master's program she spent five months at Utrecht University following the European Erasmus+ study exchange program. For the final research project, she spent one year in the NWO institute AMOLF in Amsterdam in the Photonic Forces group of Professor Verhagen, working in the field of optomechanics.

In 2016, Giada started as a PhD researcher in the same group. The outcome of the research efforts are presented in this thesis. During her PhD she presented her results in international conferences and advanced schools. She continued being independently active as organizer of cultural and artistic initiatives. In 2019 she conceived and curated *Molding Nano*, an exhibition of ceramic sculptures connecting art and science. In the same year she kick-started the Amolf Sustainability Team, a self-organized group supporting ideas towards a greener culture in the institute.

ACKNOWLEDGEMENTS

Writing this page is not an easy task, I have to say. It requires to go through the memories of such an intensely populated period of my life in which many friends and acquaintances and even just the atmosphere of certain places played a role. A PhD can be a very challenging experience (if not "is" by definition). And in science, it confronts students with hard failures, as well as peer pressure and the sense that, no matter what, the clock is always ticking. So, it is important then to have friends and a good social life to balance out that stress. As such, it is important that they all get to be remembered and acknowledged to some extent in the following pages. I can say that without the other part of my life outside of AMOLF and outside of physics, I wouldn't have survived a PhD, or vice versa, the PhD wouldn't have survived me probably.

The good thing is that life is varied and offers endless possibilities, especially in Amsterdam. For this I want to start my acknowledgements in broad terms by thanking Amsterdam, which I loved during these years for all her varied atmospheres and inclusive character. Unfortunately, I am also seeing it impoverish with the destruction of places that were of paramount importance for myself as a source of inspiration worth gold. Naming one for all, the ADM. I am glad that even a physicist in her PhD thesis feels like thanking you for all the good inspiration you brought. (Hoping that politicians tune in to listen.) I thank Fred for showing me your talent and the electric circus.

A special thank also to my art masters. Det, I am grateful you showed me your ceramics word and I look up to you as a great source of inspiration. Thank you for collaborating with me and for making me feel supported. Marjan, I enjoy painting at the atelier really much. I admire your sharp eye and the passion that you put into discussing with me.

I am so grateful I was given the possibility of being part of many different communities here in Amsterdam, made by people joined by common values and objectives. Especially those projects closer to my hands and heart like Anna's Tuin & Ruigte, Oostindishgroen and Kaskantine have been very important. I am glad I met folks like Eelco, Paula and Joao, Sara, Joao and Machteld and Galizia, Marlene,

and all the other volunteers of Anna's and in these quarantine times I greatly miss the Kas and the faces of Menno, Rodney and Betty and all the volunteers of Kaskantine: Renzo, Shannon, Jona, Roberta... and, of course, Aron. We have been sharing such an incredible period of life together and given so much to each other that even though we are now apart, I feel like we will never be fully separated ever again. Thank you for showing me your special way of life and to bring inspiration, support, friendship and grounded feelings of love into my life. I am thankful for the other places and projects that gave space for exploration and discovery. I loved the Vondelbunker, for example, and I am excited about getting more involved with the Valparaiso community with all those amazing folks (Ulysses, Rami, Dan, Sabri, Margo, Alexis, Vivian...), both of which gave far reaching insights already since a while back. A special mention to all the activists in my life and to projects like Taste before you waste (and the dear Lara), Aseed (for the great initiatives), Nieuwland (and our life drawing club) and dNM (and our community group). I want to thank my old group of friends in Amsterdam whilst exploring the city in the early times of my PhD: Rosa, Jorge, Mauro, Dagmara, Sean aaand Istvan!!! Thank you to Marina and Jelle for our dinners at MKZ. I had so much fun with you guys.

However, the start of PhD, before all those explorations, was not fun at all. My health was not that great and I went through a long and difficult period. In those times, that seem so far from now, I was lucky to have a few angels that helped me cope with everything. I want to name Jenny and Juha and thank in particular my friend Juha, who made me feel that even in the circumstance, I was not alone. I enjoy that even if we have different ideas and approaches to things in life we care for each other in a very honest and stable way.

An important feeling of brotherhood has been nurtured in the course of all these years by my beloved Lukas. I feel safe because I know you are there for me, and I am so honored to represent a source of inspiration for you. My esteem for you is profound. Thank you for writing down the title of my thesis on the front page. A special mention to our friend Dario too, which I hope to see again some day.

And how about a life in Amsterdam without Davide, and all the folks orbiting around Montelbaanstraat? I want to thank Davide and all his girlfriends, especially Sheila, but also Giovanni, Cecilia, Letizia, Ceren. And how about when Italian connections intersect Colombian connections? My dear Luisa, and my dear Maurizia I love you so much! My spiritual life wouldn't make sense without you. Thank you for the nourishing experience of our woman circle and for being my partners in crime. I hope our live's projects will stay entangled.

When it comes to life changing encounters, all my gratitude goes to my dear friend Marieke who welcomed me to the magic world of the home boat Leonora. My love for you is pure. Leonora is my community and I am lucky to experience a shared life with all of you: Sacha, Chris, Justina, Maaike, Mirna, Henry and Daniel. You are so dear to me. A special thanks to Daniel for letting me intrude your creativity with the words of this thesis inspiring the beautiful drawings you made for my cover! And a special love note to Leonora itself that nourishes me every day with her colours and sounds, and with the special sense of safety of home. I wish we could sail away in some tropical paradise one day.

Thank you to my new friends that have kept my heart warm during the last crazy few months, including a pandemic quarantine period: Masha, Ludovica, Mislav. I hope our friendships will grow strong! Each of you brought me tons of inspiration in a very different personal and peculiar way. I am grateful I found you before lockdown.

And about this lockdown and what that means for my PhD defense ceremony, I have to say I am greatly disappointed I cannot show off with my beautiful paranymphs. Jana, you are a total blast. I am in love with the look you have at life and your sharp sense of humor. I appreciate your kindness and I feel excited we found each other. Agustin, you are my wife! I have been sharing three years with you back to back and you are a container of all my moods from very happy to very depressed. I appreciate you immensely and I know our connection will last for life. All the best for you and your love life, with the dear Bram.

I wouldn't be who I am now here in Amsterdam if it were not for my previous life in Pavia. Those times forged me into the person I was at the beginning of my Amsterdam adventure, and in a way I am still now. I will always keep in my heart my dear friends Pia, Gemma and Giada and Viola, Cris, Walzer, Riccardo, Ste, Mene, Luca, Aurora, Fra, Fra, Lucia. A special mention to my dearest friend Ginevra with whom I share activism and so many life experiences. I have the feeling that our parallel growth feeds into each other's lives in such a loving and harmonious way that I cannot live without you anymore! I feel strong as a woman and as an activist, because I know of your presence on Earth. Gianluca and Lucia I am happy that you moved from Pavia to Amsterdam. I feel a piece of the Kronstadt family is here with me. I care about you a lot. And how about my dearest brother Lodovico? I miss you all the time. Maria, Emilio and Marta I still didn't have the fortune to meet in real life.

And how can I not travel with my heart back south and find the kindest and special people Barbara, Lara, Grazia, Francesco, Lino, Anna, I am so glad you welcome me back home every time. And my life sister and best friend since 20, and I say 20 years, Romana. You are a rock in my existence. The more I get to know you the more I admire you, and this is going on since such a long time that I tend to believe you are my twin soul. Which, given our family tree is possibly even close to be true. Please do not ever leave me without you.

And this brings me directly to my only true beloved amazing sister! Delia, I am crying as I write about you because you are the most important person in my life. I wish I can always be there to protect you and to be blessed by the pure and soft light that you shine in my life. Thank you for taking care of our parents. Papà Carlo and Mamma Elena, this thesis is dedicated to you. My studies brought me away from you physically, and I am sorry for this. I wish we would spend more time together. I don't know how to express my love for you, other than say GRAZIE for everything and for being alive. You are amazing. I love you famiglia!!! Dear Gaetano you are one of us too! I want to mention in the extended family also Piera and Luciano. Thank you for being so inspiring, kind and present in our lives.

Last but not least, I want to thank all the people from AMOLF. Firstly I want to mention my old friends Agata, Parisa, Jenny and Cristina, our science girlfriends

group was great and served me well for a very important period of my life. I am thankful you were at AMOLF. I want to thank my special colleagues Anne, AnneMarie, Nasim, Mareike, Christiaan, Giorgio, Beniamino, Charlie, Lucie, Federica, Ariane. Thank you for the coffees and the mutual support! A special thank you to Clyde for being such a smiling person at AMOLF. I am truly grateful for all the people who embarked in the Molding Nano adventure and for those who made me feel supported in my art science quest: Bas, Kristina, Esther, Petra. Thank you all. I hope the climate group will keep being strong with the support of the amazing and committed Verena, Julia and Tom. Thank you and all the others for collaborating with me at this project. And now to my dear Photonic Forces group: I am really worried to leave you without any woman! I will always remember you guys and sometimes even girls as an extended science family. I want to name you all starting from Lars, Freek, Nikhil, John, Amy, Hessel, Roel, Jente, Rene, Johneph, Alejandro, Laura, Cesare, Robin, Javier. A special thanks to my very special colleagues and friends Rick and Juha with whom I shared this amazing nanobeam adventure, and to Jesse and Pascal, who later joined our efforts. Last and most importantly, Ewold. Thank you for being such a great scientist and for making me feel proud of our research efforts. Witnessing each other's scientific career during these years has been a very important and interesting process. I am very thankful for the opportunity you gave me to arrive where I am now. Thank you for fueling interesting perspectives and ideas into our discussions, and for giving me the possibility to fully be myself in the work environment.

BIBLIOGRAPHY

1. Arndt, M. & Hornberger, K. Testing the limits of quantum mechanical superpositions. *Nature Physics* **10,** 271–277 (2014).
2. Safavi-Naeini, A. H., Chan, J., Hill, J. T., Alegre, T. P. M., Krause, A. & Painter, O. Observation of Quantum Motion of a Nanomechanical Resonator. *Physical Review Letters* **108,** 033602 (2012).
3. Aspelmeyer, M., Kippenberg, T. J. & Marquardt, F. Cavity optomechanics. *Reviews of Modern Physics* **86,** 1391–1452 (2014).
4. Teufel, J. D., Donner, T., Li, D., Harlow, J. W., Allman, M. S., Cicak, K., Sirois, A. J., Whittaker, J. D., Lehnert, K. W. & Simmonds, R. W. Sideband cooling of micromechanical motion to the quantum ground state. *Nature* **475,** 359–363 (2011).
5. Chan, J., Alegre, T. P., Safavi-Naeini, A. H., Hill, J. T., Krause, A., Gröblacher, S., Aspelmeyer, M. & Painter, O. Laser cooling of a nanomechanical oscillator into its quantum ground state. *Nature* **478,** 89–92 (2011).
6. Verhagen, E., Deléglise, S., Weis, S., Schliesser, A. & Kippenberg, T. J. Quantum-coherent coupling of a mechanical oscillator to an optical cavity mode. *Nature* **482,** 63–67 (2012).
7. O'Connell, A. D., Hofheinz, M., Ansmann, M., Bialczak, R. C., Lenander, M., Lucero, E., Neeley, M., Sank, D., Wang, H., Weides, M., Wenner, J., Martinis, J. M. & Cleland, A. N. Quantum ground state and single-phonon control of a mechanical resonator. *Nature* **464,** 697–703 (2010).
8. Lee, K. C., Sprague, M. R., Sussman, B. J., Nunn, J., Langford, N. K., Jin, X.-M., Champion, T., Michelberger, P., Reim, K. F., England, D., Jaksch, D. & Walmsley, I. A. Entangling Macroscopic Diamonds at Room Temperature. *Science* **334,** 1253–1256 (2011).
9. Riedinger, R., Wallucks, A., Marinković, I., Löschnauer, C., Aspelmeyer, M., Hong, S. & Gröblacher, S. Remote quantum entanglement between two micromechanical oscillators. *Nature* **556,** 473–477 (2018).

10. Ockeloen-Korppi, C. F., Damskägg, E., Pirkkalainen, J.-M., Asjad, M., Clerk, A. A., Massel, F., Woolley, M. J. & Sillanpää, M. A. Stabilized entanglement of massive mechanical oscillators. *Nature* **556,** 478–482 (2018).

11. Palomaki, T. A., Teufel, J. D., Simmonds, R. W. & Lehnert, K. W. Entangling Mechanical Motion with Microwave Fields. *Science* **342,** 710 LP –713 (2013).

12. Palomaki, T. A., Harlow, J. W., Teufel, J. D., Simmonds, R. W. & Lehnert, K. W. Coherent state transfer between itinerant microwave fields and a mechanical oscillator. *Nature* **495,** 210–214 (2013).

13. Reed, A. P., Mayer, K. H., Teufel, J. D., Burkhart, L. D., Pfaff, W., Reagor, M., Sletten, L., Ma, X., Schoelkopf, R. J., Knill, E. & Lehnert, K. W. Faithful conversion of propagating quantum information to mechanical motion. *Nature Physics* **13,** 1163–1167 (2017).

14. Wollman, E. E., Lei, C. U., Weinstein, A. J., Suh, J., Kronwald, A., Marquardt, F., Clerk, A. A. & Schwab, K. C. Quantum squeezing of motion in a mechanical resonator. *Science* **349,** 952–955 (2015).

15. Pirkkalainen, J.-M., Damskägg, E., Brandt, M., Massel, F. & Sillanpää, M. A. Squeezing of Quantum Noise of Motion in a Micromechanical Resonator. *Phys. Rev. Lett.* **115,** 243601 (2015).

16. Safavi-Naeini, A. H., Gröblacher, S., Hill, J. T., Chan, J., Aspelmeyer, M. & Painter, O. Squeezed light from a silicon micromechanical resonator. *Nature* **500,** 185–189 (2013).

17. Brooks, D. W. C., Botter, T., Schreppler, S., Purdy, T. P., Brahms, N. & Stamper-Kurn, D. M. Non-classical light generated by quantum-noise-driven cavity optomechanics. *Nature* **488,** 476–480 (2012).

18. Murch, K. W., Moore, K. L., Gupta, S. & Stamper-Kurn, D. M. Observation of quantum-measurement backaction with an ultracold atomic gas. *Nature Physics* **4,** 561–564 (2008).

19. Purdy, T. P., Peterson, R. W. & Regal, C. A. Observation of radiation pressure shot noise on a macroscopic object. *Science* **339,** 801–804 (2013).

20. Riedinger, R., Hong, S., Norte, R. A., Slater, J. A., Shang, J., Krause, A. G., Anant, V., Aspelmeyer, M. & Gröblacher, S. Non-classical correlations between single photons and phonons from a mechanical oscillator. *Nature* **530,** 313–316 (2016).

21. Sudhir, V., Schilling, R., Fedorov, S. A., Schütz, H., Wilson, D. J. & Kippenberg, T. J. Quantum Correlations of Light from a Room-Temperature Mechanical Oscillator. *Physical Review X* **7,** 31055 (Sept. 2017).

22. Purdy, T. P., Grutter, K. E., Srinivasan, K. & Taylor, J. M. Quantum correlations from a room-temperature optomechanical cavity. *Science* **356,** 1265 LP –1268 (2017).

23. Kampel, N. S., Peterson, R. W., Fischer, R., Yu, P.-L., Cicak, K., Simmonds, R. W., Lehnert, K. W. & Regal, C. A. Improving Broadband Displacement Detection with Quantum Correlations. *Physical Review X* **7,** 21008 (2017).

24. Braginsky, V. B., Khalili, F. Y. & Thorne, K. S. *Quantum Measurement* (Cambridge University Press, 1992).

25. Clerk, A. A., Devoret, M. H., Girvin, S. M., Marquardt, F. & Schoelkopf, R. J. Introduction to quantum noise, measurement, and amplification. *Reviews of Modern Physics* **82,** 1155–1208 (2010).

26. Gerry, C., Knight, P. & Knight, P. L. *Introductory Quantum Optics* (Cambridge University Press, 2005).

27. Vanner, M. R., Pikovski, I. & Kim, M. S. Towards optomechanical quantum state reconstruction of mechanical motion. *Annalen der Physik* **527,** 15–26 (2015).

28. Thorne, K. S., Drever, R. W. P., Caves, C. M., Zimmermann, M. & Sandberg, V. D. Quantum Nondemolition Measurements of Harmonic Oscillators. *Physical Review Letters* **40,** 667–671 (1978).

29. Braginsky, V. B., Vorontsov, Y. I. & Thorne, K. S. Quantum Nondemolition Measurements. *Science* **209,** 547 LP –557 (1980).

30. Caves, C. M., Thorne, K. S., Drever, R. W., Sandberg, V. D. & Zimmermann, M. On the measurement of a weak classical force coupled to a quantum-mechanical oscillator. I. Issues of principle. *Reviews of Modern Physics* **52,** 341–392 (1980).

31. Bocko, M. F. & Onofrio, R. On the measurement of a weak classical force coupled to a harmonic oscillator: Experimental progress. *Reviews of Modern Physics* **68,** 755–799 (1996).

32. Brunelli, M., Malz, D., Schliesser, A. & Nunnenkamp, A. Stroboscopic quantum optomechanics. *arXiv:2003.04361* (2020).

33. La Porta, A., Slusher, R. E. & Yurke, B. Back-Action Evading Measurements of an Optical Field Using Parametric Down Conversion. *Physical Review Letters* **62,** 28–31 (1989).

34. Pereira, S. F., Ou, Z. Y. & Kimble, H. J. Backaction evading measurements for quantum nondemolition detection and quantum optical tapping. *Physical Review Letters* **72,** 214–217 (1994).

35. Vasilakis, G., Shen, H., Jensen, K., Balabas, M., Salart, D., Chen, B. & Polzik, E. S. Generation of a squeezed state of an oscillator by stroboscopic back-action-evading measurement. *Nature Physics* **11,** 389–392 (2015).

36. Møller, C. B., Thomas, R. A., Vasilakis, G., Zeuthen, E., Tsaturyan, Y., Balabas, M., Jensen, K., Schliesser, A., Hammerer, K. & Polzik, E. S. Quantum back-Action-evading measurement of motion in a negative mass reference frame. *Nature* **547,** 191–195 (2017).

37. Lei, C. U., Weinstein, A. J., Suh, J., Wollman, E. E., Kronwald, A., Marquardt, F., Clerk, A. A. & Schwab, K. C. Quantum Nondemolition Measurement of a Quantum Squeezed State beyond the 3 dB Limit. *Physical Review Letters* **117,** 100801 (2016).

38. Clerk, A. A., Marquardt, F. & Jacobs, K. Back-action evasion and squeezing of a mechanical resonator using a cavity detector. *New Journal of Physics* **10,** 95010 (2008).

39. Hertzberg, J. B., Rocheleau, T., Ndukum, T., Savva, M., Clerk, A. A. & Schwab, K. C. Back-action-evading measurements of nanomechanical motion. *Nature Physics* **6,** 213–217 (2010).

40. Suh, J., Weinstein, A. J., Lei, C. U., Wollman, E. E., Steinke, S. K., Meystre, P., Clerk, A. A. & Schwab, K. C. Mechanically detecting and avoiding the quantum fluctuations of a microwave field. *Science* **344,** 1262–1265 (2014).

41. Shomroni, I., Qiu, L., Malz, D., Nunnenkamp, A. & Kippenberg, T. J. Optical backaction-evading measurement of a mechanical oscillator. *Nature Communications* **10,** 1–7 (2019).

42. Ockeloen-Korppi, C. F., Damskägg, E., Pirkkalainen, J. M., Clerk, A. A., Woolley, M. J. & Sillanpää, M. A. Quantum Backaction Evading Measurement of Collective Mechanical Modes. *Physical Review Letters* **117,** 140401 (2016).

43. Braginsky, V. B., Vorontsov, Y. I. & Khalili, F. Y. Optimal quantum measurements in detection of gravitaion radiation. *JETP Lett.* **27** (1978).

44. Vanner, M. R., Pikovski, I., Cole, G. D., Kim, M. S., Brukner, C., Hammerer, K., Milburn, G. J. & Aspelmeyer, M. Pulsed quantum optomechanics. *Proceedings of the National Academy of Sciences of the United States of America* **108,** 16182–7 (2011).

45. Vanner, M. R. Selective Linear or Quadratic Optomechanical Coupling via Measurement. *Physical Review X* **1,** 21011 (2011).

46. Hoff, U. B., Kollath-Bönig, J., Neergaard-Nielsen, J. S. & Andersen, U. L. Measurement-Induced Macroscopic Superposition States in Cavity Optomechanics. *Physical Review Letters* **117,** 143601 (2016).

47. Bennett, J. S., Khosla, K., Madsen, L. S., Vanner, M. R., Rubinsztein-Dunlop, H. & Bowen, W. P. A quantum optomechanical interface beyond the resolved sideband limit. *New Journal of Physics* **18,** 053030 (2016).

48. Kepler, J. De cometis libelli tres (Typis Andreae Apergiri) (1619).

49. Weis, S., Rivière, R., Deléglise, S., Gavartin, E., Arcizet, O., Schliesser, A. & Kippenberg, T. J. Optomechanically induced transparency. *Science* **330,** 1520–1523 (2010).

50. Leijssen, R. & Verhagen, E. Strong optomechanical interactions in a sliced photonic crystal nanobeam. *Scientific Reports* **5,** 15974 (2015).

51. Leijssen, R. *Measuring mechanical motion at the nanoscale.* PhD thesis (Technische Universiteit Eindhoven, 2017).

52. Freisem, L. *Low-loss photonic nanocavities with strong optomechanical interactions* tech. rep. (University of Amsterdam, 2015).

53. Robinson, J. T., Manolatou, C., Chen, L. & Lipson, M. Ultrasmall Mode Volumes in Dielectric Optical Microcavities. *Physical Review Letters* **95,** 143901 (2005).

54. Seidler, P. Optimized process for fabrication of free-standing silicon nanophotonic devices. *Journal of Vacuum Science & Technology B, Nanotechnology and Microelectronics: Materials, Processing, Measurement, and Phenomena* **35,** 031209 (2017).

55. Olynick, D. L., Cord, B., Schipotinin, A., Ogletree, D. F. & Schuck, P. J. Electron-beam exposure mechanisms in hydrogen silsesquioxane investigated by vibrational spectroscopy and in situ electron-beam-induced desorption. *Journal of Vacuum Science & Technology B, Nanotechnology and Microelectronics: Materials, Processing, Measurement, and Phenomena* **28,** 581–587 (2010).

56. Wahlbrink, T., Mollenhauer, T., Georgiev, Y. M., Henschel, W., Efavi, J. K., Gottlob, H. D., Lemme, M. C., Kurz, H., Niehusmann, J. & Bolivar, P. H. Highly selective etch process for silicon-on-insulator nano-devices. in *Microelectronic Engineering* **78-79** (Elsevier, 2005), 212–217.

57. Tuda, M., Shintani, K. & Ootera, H. Profile evolution during polysilicon gate etching with low-pressure high-density Cl2/HBr/O2 plasma chemistries. *Journal of Vacuum Science & Technology A: Vacuum, Surfaces, and Films* **19,** 711–717 (2001).

58. Selvaraja, S. K., Bogaerts, W. & Van Thourhout, D. Loss reduction in silicon nanophotonic waveguide micro-bends through etch profile improvement. *Optics Communications* **284,** 2141–2144 (2011).

59. Muhonen, J. T., La Gala, G. R., Leijssen, R. & Verhagen, E. State Preparation and Tomography of a Nanomechanical Resonator with Fast Light Pulses. *Physical Review Letters* **123,** 113601 (2019).

60. Bachor, H.-A. & Ralph, T. C. *A Guide to Experiments in Quantum Optics* 434 (Wiley, 2004).

61. Chen, Y. *Macroscopic quantum mechanics: theory and experimental concepts of optomechanics* **10,** 104001 (IOP Publishing, 2013).

62. Sudhir, V. *Quantum Limits on Measurement and Control of a Mechanical Oscillator* (Springer International Publishing, 2018).

63. Xia, K., Vanner, M. R. & Twamley, J. An opto-magneto-mechanical quantum interface between distant superconducting qubits. *Scientific Reports* **4,** 5571 (2014).

64. Lvovsky, A. I. & Raymer, M. G. Continuous-variable optical quantum-state tomography. *Rev. Mod. Phys.* **81,** 299–332 (2009).

65. Haus, H. A. *Waves and fields in optoelectronics* (Prentice-Hall, 1984).

66. Fano, U. Effects of Configuration Interaction on Intensities and Phase Shifts. *Physical Review* **124,** 1866–1878 (1961).

67. Galli, M., Portalupi, S. L., Belotti, M., Andreani, L. C., O 'faolain, L. & Krauss, T. F. Light scattering and Fano resonances in high-Q photonic crystal nanocavities. *Appl. Phys. Lett.* **94** (2009).

68. Gorodetsky, M. L., Schliesser, A., Anetsberger, G., Deleglise, S. & Kippenberg, T. J. Determination of the vacuum optomechanical coupling rate using frequency noise calibration. *Optics Express* **18,** 23236 (2010).

69. Olivero, J. J. & Longbothum, R. L. Empirical fits to the Voigt line width: A brief review. *Journal of Quantitative Spectroscopy and Radiative Transfer* **17,** 233–236 (1977).

70. La Gala, G. R. *Nonlinear optomechanical measurement of nanomechanical motion* tech. rep. (University of Pavia, 2016).

71. Brawley, G. A., Vanner, M. R., Larsen, P. E., Schmid, S., Boisen, A. & Bowen, W. P. Nonlinear optomechanical measurement of mechanical motion. *Nature Communications* **7,** 10988 (2016).

72. Vanner, M. R., Hofer, J., Cole, G. D. & Aspelmeyer, M. Cooling-by-measurement and mechanical state tomography via pulsed optomechanics. *Nature Communications* **4,** 2295 (2013).

73. Abbott, B. P., Abbott, R., Abbott, T. D. & Others, A. Observation of Gravitational Waves from a Binary Black Hole Merger. *Physical Review Letters* **116,** 061102 (2016).

74. Zhang, J., Peng, K. & Braunstein, S. L. Quantum-state transfer from light to macroscopic oscillators. *Physical Review A* **68,** 013808 (2003).

75. Pino, H., Prat-Camps, J., Sinha, K., Venkatesh, B. P. & Romero-Isart, O. On-chip quantum interference of a superconducting microsphere. *Quantum Science and Technology* **3,** 025001 (2018).

76. Cohadon, P. F., Heidmann, A. & Pinard, M. Cooling of a mirror by radiation pressure. *Physical Review Letters* **83,** 3174–3177 (1999).

77. Wilson, D. J., Sudhir, V., Piro, N., Schilling, R., Ghadimi, A. & Kippenberg, T. J. Measurement-based control of a mechanical oscillator at its thermal decoherence rate. *Nature* **524,** 325–329 (2015).

78. Rossi, M., Mason, D., Chen, J., Tsaturyan, Y. & Schliesser, A. Measurement-based quantum control of mechanical motion. *Nature* **563,** 53–58 (2018).

79. Eichenfield, M., Camacho, R., Chan, J., Vahala, K. J. & Painter, O. A picogram- and nanometre-scale photonic-crystal optomechanical cavity. *Nature* **459,** 550–555 (2009).

80. Cotrufo, M., Verhagen, E. & Fiore, A. Control of the electromagnetic field in a cavity by an external perturbation. in (ed Razeghi, M.) **10111** (International Society for Optics and Photonics, 2017), 1011128.

81. Shkarin, A. B., Flowers-Jacobs, N. E., Hoch, S. W., Kashkanova, A. D., Deutsch, C., Reichel, J. & Harris, J. G. Optically mediated hybridization between two mechanical modes. *Physical Review Letters* **112,** 013602 (2014).

82. Leijssen, R., La Gala, G. R., Freisem, L., Muhonen, J. T. & Verhagen, E. Nonlinear cavity optomechanics with nanomechanical thermal fluctuations. *Nature Communications* **8,** ncomms16024 (2017).

83. Caves, C. M. & Milburn, G. J. Quantum-mechanical model for continuous position measurements. *Physical Review A* **36,** 5543–5555 (1987).

84. Wiseman, H. M. & Milburn, G. J. *Quantum measurement and control* 1–460 (Cambridge University Press, 2009).

85. Van Der Walt, S., Schönberger, J. L., Nunez-Iglesias, J., Boulogne, F., Warner, J. D., Yager, N., Gouillart, E. & Yu, T. Scikit-image: Image processing in python. *PeerJ* **2014** (2014).

86. Clarke, J., Sahium, P., Khosla, K. E., Pikovski, I., Kim, M. S. & Vanner, M. R. Generating mechanical and optomechanical entanglement via pulsed interaction and measurement. *arXiv:1910.09603* (2020).

87. Tian, L. & Wang, H. Optical wavelength conversion of quantum states with optomechanics. *Physical Review A* **82,** 53806 (2010).

88. Stannigel, K., Rabl, P., Sørensen, A. S., Zoller, P. & Lukin, M. D. Optomechanical Transducers for Long-Distance Quantum Communication. *Physical Review Letters* **105,** 220501 (2010).

89. Genes, C., Vitali, D., Tombesi, P., Gigan, S. & Aspelmeyer, M. Ground-state cooling of a micromechanical oscillator: Comparing cold damping and cavity-assisted cooling schemes. *Physical Review A* **77,** 33804 (2008).

90. Krause, A. G., Blasius, T. D. & Painter, O. Optical read out and feedback cooling of a nanostring optomechanical cavity. *arXiv:1506.01249* (2015).

91. Guo, J., Norte, R. & Gröblacher, S. Feedback Cooling of a Room Temperature Mechanical Oscillator close to its Motional Ground State. *Physical Review Letters* **123,** 223602 (2019).

92. Meenehan, S. M. *Cavity Optomechanics at Millikelvin Temperatures*. PhD thesis (California Institute of Technology, 2015).

93. Schmeing, K. *Integrated Gallium Phosphide Photonics*. PhD thesis (EPFL, 2019).

94. Waldhäusl, R., Schnabel, B., Dannberg, P., Kley, E.-B., Bräuer, A. & Karthe, W. Efficient Coupling into Polymer Waveguides by Gratings. *Appl. Opt.* **36,** 9383–9390 (1997).

95. Almeida, V. R., Panepucci, R. R. & Lipson, M. Nanotaper for compact mode conversion. *Opt. Lett.* **28,** 1302–1304 (2003).

96. Meenehan, S. M., Cohen, J. D., Gröblacher, S., Hill, J. T., Safavi-Naeini, A. H., Aspelmeyer, M. & Painter, O. Silicon optomechanical crystal resonator at millikelvin temperatures. *Physical Review A* **90,** 11803 (2014).

97. Spillane, S. M., Kippenberg, T. J., Painter, O. J. & Vahala, K. J. Ideality in a Fiber-Taper-Coupled Microresonator System for Application to Cavity Quantum Electrodynamics. *Physical Review Letters* **91** (2003).

98. Quan, Q. & Loncar, M. Deterministic design of wavelength scale, ultra-high Q photonic crystal nanobeam cavities. *Opt. Express* **19,** 18529–18542 (2011).

99. Johnson, S. G., Mekis, A., Fan, S. & Joannopoulos, J. D. Molding the flow of light. *Computing in Science and Engineering* **3,** 38–47 (2001).

100. Svelto, O. *Principles of Lasers* (Springer).

101. Siegman, A. E. *Lasers* (Mill Valley, CA University Science Books).